

## INFORMATION TO USERS

The most advanced technology has been used to photograph and reproduce this manuscript from the microfilm master. UMI films the original text directly from the copy submitted. Thus, some dissertation copies are in typewriter face, while others may be from a computer printer.

In the unlikely event that the author did not send UMI a complete manuscript and there are missing pages, these will be noted. Also, if unauthorized copyrighted material had to be removed, a note will indicate the deletion.

Oversize materials (e.g., maps, drawings, charts) are reproduced by sectioning the original, beginning at the upper left-hand corner and continuing from left to right in equal sections with small overlaps. Each oversize page is available as one exposure on a standard 35 mm slide or as a 17" x 23" black and white photographic print for an additional charge.

Photographs included in the original manuscript have been reproduced xerographically in this copy. 35 mm slides or 6" x 9" black and white photographic prints are available for any photographs or illustrations appearing in this copy for an additional charge. Contact UMI directly to order.



Accessing the World's Information since 1938

300 North Zeeb Road, Ann Arbor, MI 48106-1346 USA



Order Number 8902860

**The relationship between intraseasonal disturbance activity and  
interannual variation of the tropical atmosphere**

Wang, Xueliang, Ph.D.

University of Hawaii, 1988

**U·M·I**

300 N. Zeeb Rd.  
Ann Arbor, MI 48106



THE RELATIONSHIP BETWEEN INTRASEASONAL DISTURBANCE  
ACTIVITY AND INTERANNUAL VARIATION OF  
THE TROPICAL ATMOSPHERE

A DISSERTATION SUBMITTED TO THE GRADUATE DIVISION OF THE  
UNIVERSITY OF HAWAII IN PARTIAL FULFILLMENT  
OF THE REQUIREMENTS FOR THE DEGREE OF  
DOCTOR OF PHILOSOPHY  
IN METEOROLOGY  
AUGUST 1988

BY

Xueliang Wang

Dissertation Committee:

Takio Murakami, Chairman  
Pao-Shin Chu  
Roger B. Lukas  
Thomas A. Schroeder  
Bin Wang

### Acknowledgements

I would like to express my great appreciation and deep gratitude to my supervisor, Professor T. Murakami for his continual support, encouragement, and instruction, and for much detailed and invaluable advice and drive throughout the course of this dissertation and my graduate work at University of Hawaii. His professional and critical guidance improves my perspective on scientific research.

My sincere thanks are forward to Drs. R. Lukas and B. Wang for their stimulating discussion and constructive comments. For their helpful suggestions on improvement of the dissertation, I greatly appreciate Drs. T.A. Schroeder and P.S. Chu.

I am indebted to Mrs. Dixie Zee and Mrs. Forbing for their assistance in editing this manuscript. Finally, I wish to thank my wife, Hualan Rui, for her understanding and suffering during the course of my study.

## Abstract

The relationship between intraseasonal disturbance activity (cluster of disturbances) and interannual variation of tropical atmosphere is investigated using five years (1979-83) of outgoing longwave radiation (OLR) and wind data. The space and time scale of the disturbance cluster, as defined by spectral amplitude, are much larger than those of individual disturbances. The nonlinear energy cascade between intraseasonal activity and interannual modes, in terms of a frequency modulation process, increases before and after ENSO, and decreases during ENSO.

Two constructed period bands of disturbance activity, i.e., 2-15 day and 30-60 day, exhibit different spatial and temporal variations on interannual time scale. The 2-15 day activity is primarily associated with interannual variations, while the 30-60 day activity is strongest over the equatorial Indian Ocean and western Pacific prior to the 1982/83 ENSO onset and below normal during the episode. There is evidence that the 30-60 day oscillation is one of the triggering mechanisms for the 1982/83 ENSO event.

The results of empirical orthogonal function analysis show that ENSO, as the most dominant mode of interannual variations, is essentially one realization of a bimodal climate system. The occurrence of ENSO is the phase shift from non-ENSO steady state to ENSO steady state. The

transition period is relatively short with enhanced intraseasonal disturbance, and ENSO state lasts much shorter than non-ENSO state does.

The largest and most easily detectable climate signal (interannual variability) over the central and eastern Pacific is traceable to the western Pacific-Indian Ocean region (a warm pool), and is phase locked to seasonality. It is suggested that an interaction among intraseasonal activity, annual cycle, and interannual modes over the warm pool region may be instrumental in leading to ENSO onset.

The phase changes for the 1982/83 ENSO event are from the pre-ENSO in Jan. 1982, through the mid-ENSO in Jan. 1983, and back to post-ENSO of Dec. 1983. Associated with this cycle is an eastward migration of interannual component of OLR and zonal winds along the equator from the Indian Ocean, across the maritime continent, to the eastern Pacific. Both the pre-ENSO and post-ENSO are possible representatives of anti-ENSO, an extreme of non-ENSO steady state. The pre-ENSO (or post-ENSO) and mid-ENSO (mature ENSO) are phase locked with the annual cycle. The pre-ENSO (or post-ENSO) synoptics are the manifestation of an anomalous enhancement of the characteristics of the normal winter circulation, whereas the mid-ENSO patterns reflect an unusual weakening of the normal winter circulation. Thus, the mid-ENSO exhibits an approximate reversal of the synoptics from the pre-ENSO (or post-ENSO) phase.

Over the North and South Pacific between about the date line and  $120^{\circ}\text{W}$ , an important area for the 1982/83 ENSO, the main characteristics of the pre-ENSO (or post-ENSO) and mid-ENSO phases are summarized as follows: Pre-ENSO (or post-ENSO) is characterized by (1) an intensified indirect N-S vertical overturning with below normal equatorial convection in contrast to above normal rainfall over the extratropics, (2) an intensification of upper oceanic troughs over both the North and South Pacific with prominent equatorial westerlies between them, and (3) substantial intraseasonal disturbance activity at 200 mb. Mid-ENSO exhibits: (1) a direct N-S vertical overturning (anomaly) accompanied by equatorial convection and extratropical dry spells, (2) an unusual weakening of upper oceanic troughs (or anomalous upper anticyclones) with equatorial easterlies inhibiting intraseasonal disturbance activity, and (3) enhanced midlatitude westerlies poleward of twin anomalous anticyclones, facilitating above normal baroclinic disturbance activity.

The Australasian sector ( $100^{\circ}$ - $160^{\circ}\text{E}$ ) is another key area for a well-defined reversal of circulation characteristics. Here, circulation changes are out of phase with those over the eastern North and South Pacific. Less organized circulation reversals also take place over the Afghanistan-Indian Ocean region ( $40^{\circ}$ - $80^{\circ}\text{E}$ ) and the Central America-South America region ( $80^{\circ}$ - $40^{\circ}\text{W}$ ).

## TABLE OF CONTENTS

Acknowledgements . . . . .	iii
Abstract . . . . .	iv
List of Illustrations . . . . .	x
List of Abbreviations . . . . .	xviii
List of Symbols . . . . .	xix

Chapter	Page
1. Introduction . . . . .	1
1.1 Background . . . . .	1
1.2 Objectives . . . . .	5
2. Data and Computational Procedure . . . . .	8
3. Spatial and Temporal Variations of Intraseasonal Convective Activity . . . . .	16
3.1. Time Mean Distribution of ICA . . . . .	16
3.2. Frequency Modulation of LFO and HFO . . . . .	19
3.2.1. Low-Frequency Oscillation . . . . .	19
3.2.2. High-Frequency Oscillation . . . . .	27
3.2.3. Discussion . . . . .	28
3.2.4. Two Components of ICA . . . . .	28
3.3. Time-Space Characteristics of OLR <sub>S</sub> and OLR <sub>L</sub> . . . . .	29
3.3.1. Percentage Variance of OLR <sub>S</sub> and OLR <sub>L</sub> . . . . .	31
3.3.2. The Variation of OLR <sub>L</sub> . . . . .	33
3.3.3. The Variation of OLR <sub>S</sub> . . . . .	36

4.	Interannual and Seasonal Variation of Intraseasonal Convective Activity . . . . .	42
4.1.	An Overview . . . . .	42
4.2.	Convection . . . . .	48
4.2.1.	Interannual Variation . . . . .	48
4.2.2.	Seasonal Variation . . . . .	55
4.2.3.	A Discussion . . . . .	57
4.3.	Intraseasonal Convective Activity . . . . .	61
4.3.1.	Interannual Component . . . . .	61
4.3.2.	Seasonal Component . . . . .	65
4.4.	An Example of Climate Predictability . . . . .	66
5.	The 1982/83 ENSO . . . . .	75
5.1.	Introduction . . . . .	75
5.2.	Interannual Zonal Wind . . . . .	77
5.3.	Intraseasonal Disturbance Activity . . . . .	82
5.3.1.	The 30-60 Day Activity . . . . .	82
5.3.2.	The 2-15 Day Activity . . . . .	91
5.4.	Global-Scale Synoptics of Interannual Modes . . . . .	97
5.4.1.	JAN(0) Circulation Patterns . . . . .	97
5.4.2.	JAN(-1) Circulation Patterns . . . . .	116
5.4.3.	DEC(0) Circulation Patterns . . . . .	124
5.5.	Momentum Budget for Low-Level u" Westerlies . . . . .	127
6.	Discussion and Conclusion . . . . .	133
6.1	Discussion . . . . .	133

6.2 Conclusion . . . . . 137

Appendix . . . . . 142

    A. Significance Test of EOF Eigenmodes . . . . . 142

    B. Measurement of Climate Predictability . . . . . 143

Reference . . . . . 147

## LIST OF ILLUSTRATIONS

Figure	Page
3.1 Mean power spectra of OLR' along the equator during the five years of 1979-83. Unit is $10^2 \text{ W}^2\text{m}^{-4}\text{day}$ . Every grid point represents the areal average of $20^\circ \text{ lon.} \times 10^\circ \text{ lat.}$ , the points shown are centered at $0^\circ\text{E}$ (a), $30^\circ\text{E}$ (b), . . . . , $30^\circ\text{W}$ (l), respectively. . . . .	17
3.2 Time dependence of power spectral amplitude of equatorial OLR' averaged between $5^\circ\text{S}$ and $5^\circ\text{N}$ for period range of 25 to 100 days. Unit is $\text{W}^2\text{m}^{-4}\text{day}$ . Contour intervals are shown above the top-right corner of each diagram. Only positive anomalies (exceeding the season mean) are shown. The grid points shown are same as in Fig. 3.1.	
(a) - (d). . . . .	20
(e) - (h). . . . .	21
(i) - (l). . . . .	22
3.3 As in Fig. 3.2, except for 2-15 day period.	
(a) - (d). . . . .	24
(e) - (h). . . . .	25
(i) - (l). . . . .	26
3.4 Percentage of spectra amplitude explained by 30-60 day period band OLR <sub>L</sub> (a) and 2-15 day period band OLR <sub>S</sub> (b). Intervals are 0.05 and	

- shading are larger than 0.3 (0.45) for 30-60 (2-15) day. Zonal means are shown at the right. See text for definition of  $OLR_L$  and  $OLR_S$ . . . . 30
- 3.5 (a): Five-year mean of  $OLR_L$ . Unit is  $W^2m^{-4}day$ . Intervals and shading are shown above the top-right corner of the figure, i.e., 2500 and greater than 5000 units, respectively. (b): As in (a), except for standard deviation of  $\langle OLR_L \rangle$ . See text for definition of  $\langle OLR_L \rangle$ . (c): As in (b), except for  $OLR_L''$ , as defined by eq. (3). The zonal means are shown at the right side of each figure. . . . 32
- 3.6 Time series of  $OLR_L$  (solid) and its normal annual cycle (dash) along the equator. Unit is  $10^2 W^2m^{-4}day$ . The grid points shown are same as in Fig. 3.1. . . . . 35
- 3.7 As in Fig. 3.5, except for  $OLR_L$ . . . . . 37
- 3.8 As in Fig. 3.6, except for  $OLR_S$ . . . . . 40
- 4.1 As in Fig. 3.7a, except for  $OLR''(S)$  (a) and  $OLR''(I)$  (b), as defined by eq. (4). . . . . 43
- 4.2 As in Fig. 4.1, except for  $OLR_L''(S)$  and  $OLR_L''(I)$  . . 45
- 4.3 As in Fig. 4.1, except for  $OLR_S''(S)$  and  $OLR_S''(I)$  . . 47
- 4.4 The first two EOF eigenvectors  $E_1$  (a) and  $E_2$  (b) for  $OLR''(I)$ , over the five years of 1979-83. Intervals are 0.05 (non-dimensional) with light mesh (hatching) indicating regions of greater (less) than 0.025 (-0.025); no zero line. The

	fractional variance of each mode is shown in the top-right corner of the diagram. The time series of eigenvector coefficients $C_1(t)$ and $C_2(t)$ are shown in (c) and (d), respectively. Also shown in (a) is the Southern Oscillation Index SOI" (dot line). . . . .	49
4.5	As in Fig. 4.4, except for the OLR"(I) data set excluded the 1982/83 ENSO period (July 1982 - June 1983). Time coefficients over the ENSO period are the projection of OLR"(I) on the corresponding spatial EOF modes. . . . .	53
4.6	As in Fig. 4.4, except for OLR"(S). . . . .	56
4.7	Time-longitude section of OLR"(I) (a), OLR"(S) (b), and OLR"(c) along the equator. Intervals are $5.0 \text{ Wm}^{-2}$ for (a) and (c), 4.0 for (b). Mesh (hatching) indicates larger (less) than 2.5 (-2.5) for (a) and (c), 2.0 (-2.0) for (b); no zero line. . . . .	58
4.8	As in Fig. 4.4, except for OLR <sub>S</sub> "(I). . . . .	62
4.9	As in Fig. 4.4, except for OLR <sub>L</sub> "(I). . . . .	64
4.10	Distributions of phase differences between OLR <sub>S</sub> " (a) as well as OLR <sub>L</sub> " (b) at individual grid points and OLR" at the reference point ( $5^{\circ}\text{S}$ , $150^{\circ}\text{W}$ ) for the spectral band centered at a period of 20 months, as computed over entire five year period. Arrows pointing to south indicate zero	

- phase difference. Arrows are rotated in a clockwise (counterclockwise) fashion by  $1^\circ$  for each degree of phase lag (lead) of  $OLR_S''$  or  $OLR_L''$  relative to the reference time series of  $OLR''$ . The squared coherence values exceed the 90% and 95% significance levels are indicated by the light mesh and heavy dot. . . . . 67
- 4.11 Climate signal-to-noise ratio in summer (a) and winter (b). Intervals are 2.0, and heavy mesh denotes the region of larger than 5.0, and light mesh indicates the area of less than 5.0 and greater than 1.0. Zonal mean are also shown at the right. . . . . 70
- 5.1 Left: Longitude-time sections of three-month running mean  $u$  at 200 mb (a; interval  $5 \text{ ms}^{-1}$ ) and 850 mb (c; interval  $2 \text{ ms}^{-1}$ ) along the equator. Shading indicates regions of westerly  $u$ . Right: As in left, except for anomaly  $u''$  at 200 mb (b; interval  $2.5 \text{ ms}^{-1}$ ) and 850 mb (d; interval  $1 \text{ ms}^{-1}$ ). Shading denotes regions of westerly anomaly ( $u'' > 0$ ). . . . . 78
- 5.2 Time series of 30-60 day convective activity  $OLR_L''$  (unit:  $10^4 \text{ W}^2 \text{ m}^{-4} \text{ day}$ ) at the equator for every 30 degrees of longitude from  $60^\circ \text{E}$  to  $60^\circ \text{W}$ . Shading indicates regions of above normal activity. See text for further information. . . . . 83

- 5.3 Time series of daily  $OLR'$  (a),  $\bar{OLR}$  (b), and  $OLR^*$  (c) at (Equator,  $90^{\circ}E$ ) from 1 Jan. 1982 to 28 Feb. 1983, unit of  $Wm^{-2}$ . Refer to Section 2 for detail. . . . . 85
- 5.4 The first EOF pattern (a) of the 30-60 day filtered  $\bar{OLR}$ . Intervals are 0.05 (non-dimensional), and shading denotes less than -0.025, and zero line is omitted. The frictional variance is shown in the bracket. Shown in (b) is the time coefficient  $C_1(t)$ . The standard deviation of  $C_1(t)$  is also shown in (b). The largest amplitude of  $C_1(t)$  is marked by a letter x (Adopted from Shrestha, 1986). . . . . 86
- 5.5 Seven-day running mean of  $OLR'$  (unit:  $Wm^{-2}$ ) at the selected days from May 1st to Nov. 1st 1982. Intervals are 10.0 units and mesh (hatching) denotes the greater (less) than +5.0 (-5.0) units; no zero lines. The major convection centers are marked by minus sign '-'.  
 (a) - (j). . . . . 88  
 (k) - (t). . . . . 89
- 5.6 As in Fig. 5.2, except for 2-15 day convective activity  $OLR_g''$ . . . . . 92
- 5.7 As in Fig. 5.3, except for at (EQ.,  $150^{\circ}W$ ) from 1 May 1982 to 30 June 1983. The largest amplitude of  $OLR^*$  in (c) is marked by a letter x. . . . . 94

- 5.8 As in Fig. 5.5, except for daily map of OLR\* over the eastern Pacific from Dec. 22 to Dec. 27 1982. . . . . 96
- 5.9 Mid-ENSO (January 1983) patterns for OLR'' (a;  $5 \text{ Wm}^{-2}$  unit), OLR<sub>S</sub>'' (b;  $10^4 \text{ W}^2\text{m}^{-4}\text{day}$  unit), and OLR<sub>L</sub>'' (c;  $10^4 \text{ W}^2\text{m}^{-4}\text{day}$  unit). Interval is 1 unit. Light mesh (hatching) indicates regions of greater (less) than +0.5 (-0.5) unit; no zero lines. The letter U (D) in (a) denotes updraft or convection (downdraft or non-convection) region, and M (m) in (b) and (c) indicates maximum (minimum) convective activity. The heavy (light) arrows in (a) denotes anomalous Walker (local Hadley) circulation. . . . 98
- 5.10 Time-latitude section of zonally averaged correlation between OLR'' and OLR<sub>S</sub>'' (a), and between OLR'' and OLR<sub>L</sub>'' (b). Intervals are 0.15. Shading indicates negative correlation less than -0.3. The 5-year mean correlations are also shown at the right end of the diagram, the triangle (asterisk) denotes mean correlation exceeding 0.5 (0.3). . . . . 101
- 5.11 Mid-ENSO (January 1983) patterns for ( $u''$ ,  $v''$ ) vectors (a),  $K_S''$  (b), and  $K_L''$  (c) at 200 mb. Unit vector is  $10 \text{ ms}^{-1}$  and major distributions are indicated by H and L. Heavy dashed lines denotes regions of OLR'' less than  $-7.5 \text{ Wm}^{-2}$ . Intervals

for normalized $K_S''$ and $K_L''$ are 0.5; light mesh indicates regions greater than 0.25 (no zero and negative contours). . . . .	103
5.12 As in Fig. 5.11, except for the 850 mb level . . .	108
5.13 Schematic diagram for a direct N-S vertical overturning (anomaly) occurring over the eastern North and South Pacific ( $180^\circ$ - $120^\circ$ W) during the mid-ENSO phase of January 1983. . . . .	113
5.14 As in Fig. 5.13, except for an indirect N-S vertical overturning (anomaly) over the Japan-maritime continent-Australia area ( $100^\circ$ - $160^\circ$ E) . .	115
5.15 As in Fig. 5.9, except for the pre-ENSO phase of January 1982. . . . .	117
5.16 As in Fig. 5.11, except for the pre-ENSO phase of January 1982. . . . .	119
5.17 As in Fig. 5.12, except for the pre-ENSO phase of January 1982. . . . .	121
5.18 As in Fig. 5.9, except for the post-ENSO phase of December 1983. . . . .	123
5.19 As in Fig. 5.11, except for the post-ENSO phase of December 1983. . . . .	125
5.20 As in Fig. 5.12, except for the post-ENSO phase of December 1983. . . . .	126
5.21 Westerly momentum budget due to short-period (2-15 day) disturbances at 850 mb. Arrows are proportional to the direction and magnitude of	

the momentum fluxes integrated along the boundaries (unit: $10^6 \text{ m}^3\text{s}^{-2}$ ), while the number at the center of the represents the net westerly momentum balance. The areal averaged zonal wind $u''$ is also shown at the center of diagram. . . . .	128
5.22 As in Fig. 5.21, except for low-frequency (30-60 day) perturbations. . . . .	131

## LIST OF ABBREVIATIONS

AR	Auto-regression
D	Downdraft
DNS	Direct North and South
ECMWF	European Center for Medium Range Weather Forecast
ENSO	El-Niño and Southern Oscillation
EOF	Empirical Orthogonal Function
HFO	High Frequency Oscillation
ICA	Intraseasonal Convective Activity
ITCZ	Intertropical Convergence Zone
LFO	Low Frequency Oscillation
NECZ	Near Equatorial Convergence Zone
NH	Northern Hemisphere
NOAA	National Oceanic and Atmospheric Administration
N-S	North and South
OLR	Outgoing Longwave Radiation
RNS	Reversal North and South
SH	Southern Hemisphere
SNR	Signal-to-Noise Ratio
SO	Southern Oscillation
SOI	Southern Oscillation Index
SPCZ	South Pacific Convergence Zone
SST	Sea Surface Temperature
U	Updraft
WC	Walker Circulation

## LIST OF SYMBOLS

OLR	Original daily data
$\langle \text{OLR} \rangle$	Normal annual cycle, daily
$\text{OLR}'$	Departure from normal annual cycle, daily data
$\text{OLR}^*$	2-15 day filtered daily data
$\bar{\text{OLR}}$	30-60 day filtered daily data
$\text{OLR}''$	Three-month running mean monthly data
$\text{OLR}''(\text{I})$	Interannual component, with period longer than one year, of $\text{OLR}''$
$\text{OLR}''(\text{S})$	Seasonal component, with period less than one year and longer than one season, of $\text{OLR}''$
$\text{OLR}_p(t, f)$	Spectra of $\text{OLR}'$ computed within five-month period centered at month $t$ , monthly data
$\text{OLR}_L$	Averaged spectra of $\text{OLR}_p(t, f)$ over the 30 day to 60 day period band, monthly data
$\text{OLR}_S$	Averaged spectra of $\text{OLR}_p(t, f)$ over the 2 day to 15 day period band, monthly data
$\langle \text{OLR}_L \rangle$	Normal annual cycle of $\text{OLR}_L$ , monthly
$\langle \text{OLR}_S \rangle$	Normal annual cycle of $\text{OLR}_S$ , monthly
$\text{OLR}_L''$	Three-month running mean of $\text{OLR}_L$ departure from $\langle \text{OLR}_L \rangle$ , monthly
$\text{OLR}_S''$	Three-month running mean of $\text{OLR}_S$ departure from $\langle \text{OLR}_S \rangle$ , monthly
$\text{OLR}_L''(\text{I})$	Interannual component of $\text{OLR}_L''$
$\text{OLR}_S''(\text{S})$	Seasonal component of $\text{OLR}_S''$

$u'', v''$	Three-month running mean monthly winds
$u^*, v^*$	2-15 day filtered daily winds
$\tilde{u}, \tilde{v}$	30-60 day filtered daily winds
$(u_L u_L)$	Zonal transport of westerly momentum for 30-60 day oscillation
$(u_L v_L)$	Meridional transport of westerly momentum for 30-60 day oscillation
$(u_S u_S)$	Zonal transport of westerly momentum for 2-15 day disturbance
$(u_S v_S)$	Meridional transport of westerly momentum for 2-15 day disturbance
$K_L''$	Three-month running mean of monthly kinetic energy computed from 30-60 day filtered wind field
$K_S''$	Three-month running mean of monthly kinetic energy computed from 2-15 day filtered wind field

## 1. Introduction

### 1.1 Background

Interannual variability in the atmosphere and ocean has been of significant interest in the last two decades, particularly its manifestation as El Nino-Southern Oscillation (ENSO) events. Investigations into various aspects of the coupled atmosphere-ocean system on an interannual time scale with relevance to the ENSO phenomenon have greatly accelerated in recent years. There are at least two good reasons for this increased activity. First, recent extreme climatic anomalies, e.g., the 1982/83 ENSO, have encouraged research into the understanding of the global climate system, with the tropics thought to be a key component of this system. Second, only in the past several years have such studies become possible. Because the data required to elucidate variability on climatic space and time scales over the globe simply did not exist until several years ago. The availability of comprehensive data coverage for recent events, such as the 1982/83 ENSO, presents an opportunity for more detailed study of the interannual atmospheric variation associated with an ENSO event.

The importance of interannual atmospheric variability was first recognized by Bjerknes (1966, 1969, and 1972), and presented in terms of variation of the Walker Circulation (WC) which is characterized during a normal year by

ascending motion in the western Pacific, descending motion in the eastern Pacific, westward motion near the surface, and eastward motion at 200 mb (Walker, 1923 and 1924). He suggested that phase shift of the anomalous WC is closely tied to the Southern Oscillation (SO), and is primarily associated with tropical circulation anomalies. In the practical sense, Bjerknes perceived that the anomalous variability associated with the WC phase which alternates on the interannual time scale, is likely to play an important part in future seasonal forecasting of climatic anomalies over North America and even over the Europe. Moreover, many recent studies show that interannual modes in association with ENSO events have a global perspective (e.g., Rasmusson and Carpenter, 1982; Rasmusson and Wallace, 1983; Phillander, 1983).

One of the key questions regarding the interannual ENSO is the triggering mechanism of the event. This topic is currently being addressed by both atmospheric and oceanic studies, because ENSO is an air-sea coupled phenomenon. The focus of this study is on the atmospheric aspects, however.

By using ten years of OLR data, Lau and Chan (1985) have noted the spatial similarity of the anomalous convection and circulation patterns between ENSO and the 30-60 day modes of variation. Based on a limited amount of evidence, Lau and Chan (1986) suggested the occurrence of

ENSO may be the result of the episodic amplification of the 30-60 day mode through a coupled ocean-atmosphere interaction. Lau (1985a,b) has also proposed a stochastic-dynamical theory of ENSO, emphasizing the importance of the interaction among the seasonal cycle, air-sea coupling and stochastic forcing in leading to the onset and evolution of ENSO anomalies.

The occurrence of surface westerly wind anomalies over the equatorial Pacific in conjunction with the onset of ENSO events has become another significant area of current research. Wyrтки (1975) concluded that wind anomalies associated with a massive collapse of the easterlies over the central Pacific generate a redistribution of water mass and oceanic heat from the western to eastern Pacific, consistent with equatorial oceanic Kelvin wave dynamics (McCreary, 1976). By examining long time series of island meteorological observations, Luther et al. (1983) also found some relationship between westerly wind events, so-called westerly bursts, and ENSO. Westerly bursts seemed to be more frequent prior to many, but not all, occurrences of ENSO. Typically, a westerly burst lasts a few days, and has westerly winds of  $4-5 \text{ ms}^{-1}$ , which results in an anomalous westerly of about  $8 \text{ ms}^{-1}$  (Keen, 1987). Based on wind and sea level statistics, Lukas et al. (1984) showed that westerly bursts were responsible for generating first and second vertical mode Kelvin waves, which eventually

facilitated the onset of the 1982/83 ENSO. Harrison and Schopf (1984) further suggested from model results that even though the dynamics of the Kelvin wave pulse are essentially linear, the interaction of the pulse with the background thermal structure is nonlinear, and a sequence of such pulses can produce an evolutionary warming trend. Thus, short-time scale atmospheric variability is possibly related to the development of low-frequency sea surface temperature (SST) anomalies associated with ENSO events.

In a series of studies of intraseasonal variations of the tropical atmosphere, Murakami et al. (1984, 1986a, and 1986b) demonstrated that the activity of the short-term, synoptic-scale disturbances change with a period of about 30-60 days as a group velocity dispersion process. They further showed that the low-frequency (30-60 day) modes also appear to have some evidence of interannual amplitude modulation with an approximate period of 2.5 years. Moreover, they pointed out that the amplitude of 30-60 day oscillation exhibits strong seasonality over the monsoon regions away from the equator. Nakazawa (1986) also found the 30-60 day amplitude modulation of short-term variations in outgoing longwave radiation (OLR). In a recent paper, Yamazaki and M. Murakami (1987) showed that the enhanced amplitude modulation of transient wind disturbances over the equatorial western Pacific is often accompanied by the clustered genesis and/or development of tropical cyclones.

These phenomena are indicative of the strong nonlinear interaction among 30-60 day oscillations, transients, and interannual variations in the atmosphere.

## 1.2 Objectives

In conjunction with the results cited above, it is reasonable to suggest a cascading energy exchange between transient and interannual modes associated with the meteorological aspects of the ENSO events. While such a hypothesis remains to be tested, it should be pointed out that new insight into the understanding of ENSO phenomenon may be gained by investigating transient disturbances, 30-60 day oscillations, and interannual variations as interconnected components of the tropical ocean-atmosphere system. The main objective of the present study is the investigation of interannual modes and intraseasonal (including transient and 30-60 day) activities in a common framework. This follows the lead of cited studies which have shown evidences of interaction among transient, 30-60 day oscillation and interannual variation in the atmosphere. The relationship between short-term disturbances and 30-60 day modes will not be addressed.

Since ENSO event explains the major portion of interannual variance, the present study attempts to detail the spatial structure of interannual modes and its association with intraseasonal disturbances in terms of the

1982/83 ENSO event. Rasmusson and Carpenter (1982) discussed the sequence of events by means of composite SST and surface wind for six ENSO episodes that occurred between 1949 and 1981, and Meehl (1987) applied a similar compositing technique to depict the statistical aspects of ENSO. These composites were made in terms of time, and not with respect to phase for each cycle of ENSO. Thus, the compositing of many ENSO events might combine different flow regimes together, thereby masking the distinct characteristic of individual ENSO episodes. Therefore, the interest of this study is not in the statistical nature of many ENSOs combined, but in the evolution of an individual event, i.e., the 1982/83 ENSO episode, which is of particular interest because of its unusual intensity and evolution, as well as its superior data coverage. Also examined are global synoptic feature characteristics of the 1982/83 ENSO mature phase (mid-ENSO) with comparison to that of the preceding (pre-ENSO) and succeeding (post-ENSO) winters, which are two extremes phases of non-ENSO circulation before and after the 1982/83 ENSO event. An understanding of these relationships between intraseasonal and interannual components of atmospheric variability is paramount to a more complete knowledge of onset and evolution of ENSO.

In Section 2, a discussion of data and computational algorithms is presented. The spatial and temporal varia-

tions of intraseasonal activities in terms of frequency and amplitude modulations are detailed in Section 3. The relationship between these intraseasonal activities and interannual modes is investigated in Section 4. In addition, a brief discussion concerning the seasonality of these activities also appears in Section 4. Section 5 describes in detail the relationship between interannual flow patterns and intraseasonal activities with application to the 1982/83 ENSO, and the global synoptics of the 1982/83 pre-ENSO (or post-ENSO) and mid-ENSO phases. Finally in Section 6, the results of this study are synthesized and discussed in terms of the dynamical and physical properties of the short-term climate variations.

## 2. Data and Computational Procedure

The spatial domain for the present study is the global tropics between 40°N and 40°S. Daily outgoing longwave radiation (OLR) data, a mean of the morning and evening observations, obtained from scanning radiometers aboard polar-orbiting satellites operated by the National Oceanic and Atmospheric Administration (NOAA) were used. The OLR data cover the period, January 1979 through December 1983, at a 2.5° latitude-longitude resolution. The methods used to derive the radiation values have been extensively described (Gruber and Winston, 1978).

The OLR data are used as a surrogate of convection or latent heating, as has been done by many researchers (e.g., Murakami, 1980; Lau and Chan, 1985). The usefulness of OLR for this purpose results from the fact that thermal radiation emitted by the sea surface is absorbed and remitted by atmospheric water (vapor, droplets, or ice crystals). The amount of radiation remitted depends on the temperature of the atmospheric water, which in turn is a function of altitude. The longwave radiation received at a satellite is therefore an integrated measure of the distribution of water vapor with height. The sequence of multiple absorption and re-emission results in a brightness temperature appropriate for a concentration of water vapor at a high level. Thus, when large quantities of water vapor are transported upward in deep tropical convective clouds, the

altitude of the apparent emission source is raised, thereby lowering the brightness temperature and reflecting the great amount of latent heat release. These regions appear as areas of lower (cooler) satellite-sensed OLR that can be distinguished from relatively higher (warmer) OLR areas free from convection or latent heating.

For the same five years, daily winds ( $u$ ,  $v$ ) at 200 mb and 850 mb are also utilized. These data are extracted from the objectively analyzed data set prepared by the European Centre for Medium Range Weather Forecasts (ECMWF), which has the same resolution as that of OLR fields. The suitability of the ECMWF wind data can be established by its very good correspondence with NOAA OLR data, both for planetary perturbations and global statistics of synoptic disturbances on interannual and intraseasonal time scales (e.g., Arpe et al., 1986, Weickmann, 1987, Murakami, 1988).

The normal annual cycle is determined from the mean daily value for each day of the year over all years. Applying harmonic analysis, the first three harmonics are computed from these smoothed daily data by:

$$S(t) = \sum_{m=1}^3 A_m \exp(i2\pi mt/T_0) \quad (1)$$

where  $A_m$  is the complex amplitude of  $m$ -th harmonic,  $T_0$  is the total number of days in a year, and  $m$  denotes the harmonic, for example,  $m=1$  corresponds to annual harmonic.

Thus, the summed quantity  $S(t)$  for the first three harmonics together with the annual mean is associated primarily with the normal annual cycle, which is identical from one year to another. Here, angle braces are introduced to represent the normal annual cycle, and a prime to define the departure from it. OLR, for example, can be expressed as:

$$OLR = \langle OLR \rangle + OLR' \quad (2)$$

Thus,  $OLR'$  represents the anomalous OLR, which includes the intraseasonal as well as interannual time scale.

For the investigation of intraseasonal variations, a prefiltering is applied to the anomalies by utilizing the procedure formulated by M. Murakami (1979). This is a recursive filter. In order to avoid the frequency shift, the filter has been designed to run forward and backward through the time series. A detailed description of the method has been given by author (Wang, 1986). The filter has been carried out for two frequency bands. The first band covers a wide period range from about 30 to 60 days with the center at 45 days. These 30-60 day filtered data are hereafter signified by the notation ( $\sim$ ). The second filter is designed to retain high frequency components with periods shorter than 15 days, which are denoted as (\*).

In order to isolate the interannual component, the monthly means for the entire five years are computed first from the transient values, for example,  $OLR'$ . The interannual modes are then expressed by three-month running mean anomalies as follows:

$$(OLR'')_i = 0.25(OLR')_{i-1} + 0.5(OLR')_i + 0.25(OLR')_{i+1} \quad (3)$$

where  $(OLR')_i$  represents the monthly mean  $OLR'$  value at month  $i$ . Note that the  $(OLR')_i$  includes not just the interannual mode but also some intraseasonal variability. However, these intraseasonal variations are satisfactorily filtered out in the time series of  $(OLR'')_i$  data.

Since the main purpose of the present study is to investigate the relationship between intraseasonal disturbances and interannual modes, the intensity of transient  $OLR'$  activity on the interannual time scale was estimated by spectral analysis using the Maximum Entropy Method (MEM) as:

$$OLR_p(t, f) = \frac{2 \sigma^2(t)}{\left| 1 - \sum_{j=1}^M \alpha_j \exp(-i2\pi f j) \right|^2} \quad (4)$$

where  $\sigma^2(t)$  is the variance of time series within the computing period centered at month  $t$ . In this study,  $\sigma^2(t)$  is computed from every five-month period.  $\alpha_j$  is the coeffi-

cient of prediction error filter evaluated by fitting an auto-regressive (AR) model, and  $M$  is the order of the filter determined from the lag correlation of the series.  $OLR_p(t, f)$  represents the OLR' power at each frequency ( $f$ ) and each month ( $t$ ) where a five-month computing period is shifted from the beginning to the end of the entire five years of 1979-83 with an one-month interval each time. Following the same procedure as described in Eq. 1, the normal annual cycle was also computed from  $OLR_p(t, f)$  data at each frequency. These monthly time series of anomalous spectra,  $OLR_p^i(t, f)$ , over the global tropics between  $40^{\circ}N$  and  $40^{\circ}S$  are then smoothed by the three-month running mean in Eq. 3. By motivation of Murakami et al. (1986a), those smoothed spectra, signified as  $OLR_p^{ii}(t, f)$ , will be used to investigate the nature of interannual amplitude and frequency modulation of the intraseasonal disturbance.

Eddy kinetic energy, as denoted by  $K$ , is also computed in order to investigate intensity of wind disturbances. On the 2-15 day and 30-60 day time scale, for example,  $K$  is defined by:

$$K^* = (u^{*2} + v^{*2}) / 2 \quad (5a)$$

$$\bar{K} = (\bar{u}^2 + \bar{v}^2) / 2 \quad (6a)$$

respectively. Then the monthly mean of these daily eddy kinetic energy is computed as:

$$K_S = 1/N \sum_{n=1}^N K_n^* \quad (5)$$

$$K_L = 1/N \sum_{n=1}^N \bar{K}_n \quad (6)$$

where  $N$  is the total number of days in the corresponding month. Three-month running mean anomalies, i.e.,  $K_S''$  and  $K_L''$ , are then evaluated from monthly  $K_S$  and  $K_L$  data after the normal annual cycle is removed.

Empirical orthogonal function (EOF) analysis is used to characterize the global-scale variability of interannual modes. The main advantage of this analysis technique is that it often enables a description of the variations of a complex geophysical field with a relatively small number of functions and associated time coefficients. More importantly, the derived empirical functions often are amenable to physical interpretation which may give insight into complex processes. The procedure employed here is essentially the method outlined by Grimmer (1963) and Kutzbach (1967). A brief discussion is given below.

Let  $f_n$  be an  $L$  spatial component vector representing the  $n$ -th observation. The  $f_n$  may be expressed as:

$$f_n = \sum_{i=1}^L C_{in} E_i, \quad n=1,2, \dots, N \quad (7)$$

where  $E_i$  denotes an eigenvector associated with the  $i$ -th eigenvalue,  $C_{in}$  is the coefficient of the  $i$ -th eigenvector

for the n-th observation, and N is the total number of observations. Before the performance of the EOF analysis, each variable was normalized or nondimensionalized by dividing it by the mean standard deviation computed at all L grid points. This normalization assures that each variable at each point in the field is of equal importance in determining the principle modes of variation. Thus, the eigenvectors computed using the normalized variables reflect the real spatial distribution of variance over the domain considered. Each component of the eigenvector  $E_i$  is subject to the condition that the total variance of its elements  $e_{ij}$  is unity, i.e.,

$$\sum_{j=1}^L (e_{ij})^2 = 1, \quad i=1, 2, 3, \dots, L \quad (8)$$

The eigenvectors and their associated eigenvalues represent the solution of a maximization of the "explained variance" problem. The fraction of the total variance  $V_k$ , explained by the k largest eigenvalues, can be estimated as:

$$V_k = \frac{\sum_{i=1}^k \lambda_i}{\sum_{i=1}^L \lambda_i} \quad (9)$$

where  $\lambda_i$  represents the i-th eigenvalue.

The statistical significance of the eigenvectors is tested using the rule-of-thumb (semi-empirical) method

suggested by North et al. (1982). The precise significance testing method of the EOF eigenvectors (Overland and Preisendorfer, 1982), which has not been performed in present study, is outlined in the Appendix. In the following discussion, only those eigenmodes which are statistically independent each other will be highlighted.

### 3. Spatial and Temporal Variations of Intraseasonal Convective Activity

Based on the procedures discussed in the previous section, OLR spectra are calculated for each month over the tropical globe from 40°S to 40°N. Those monthly time series of the OLR spectra represent convective intensity change in different frequency bands. The intraseasonal convective activity (ICA) are defined as OLR spectra with periods less than one season. They will be used to investigate seasonal<sup>1</sup> and interannual variations of atmospheric convection as well as circulation.

#### 3.1. Time Mean Distribution of ICA

Shown in Fig. 3.1 are the five year (1979-1983) mean spectra of OLR along the equator. Based on mean value of lag one auto-correlation, mean red-noise spectra at the 95% confidence level, as shown by dash line, are also computed to determine the statistical significance of the spectra.

It is obvious from Fig. 3.1 that peaks in the spectra in the 30-60 day range are mostly confined to the tropical Indian Ocean and the western Pacific areas. The most pronounced signal is found in the eastern Indian Ocean (see

---

<sup>1</sup>In order to distinguish from annual variation, a term 'seasonal' is used to refer the component with period less than one year and longer than one season in this paper.

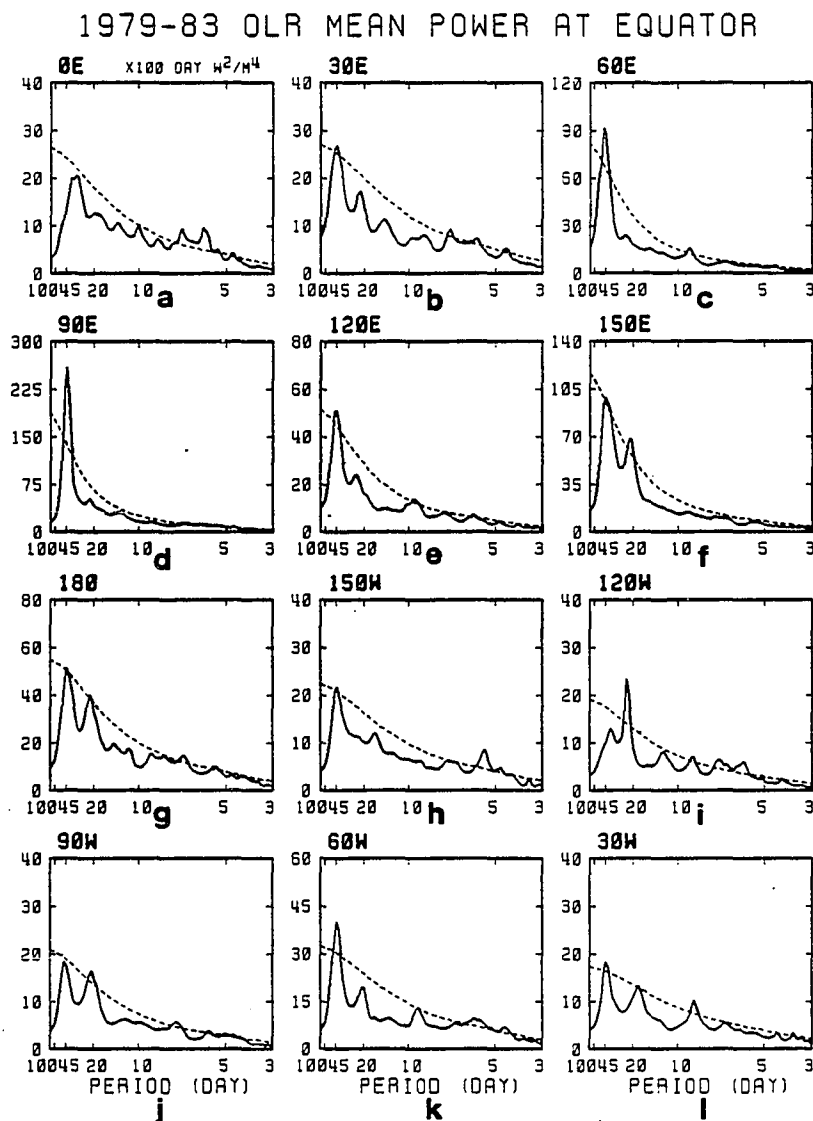


Fig. 3.1 Mean power spectra of OLR' along the equator during the five years of 1979-83. Unit is  $10^2 \text{ W}^2 \text{ m}^{-4} \text{ day}$ . Every grid point represents the areal average over  $20^\circ$  longitude  $\times 10^\circ$  latitude. The points shown are centered at  $0^\circ \text{E}$  (a),  $30^\circ \text{E}$  (b), ..., and  $30^\circ \text{W}$  (l), respectively.

spectrum for  $90^{\circ}\text{E}$ ). Over the eastern Africa-western Indian Ocean region and the western Pacific, the 30-60 day signal is still significant, but is much reduced. Another significant 30-60 day peak, although of smaller magnitude, is over Brazil and the western Atlantic. Near and east of the date line, the high frequency signal (periods  $< 15$  days) is much enhanced while the 30-60 day signal is depressed.

From examination of mean OLR spectra at all latitudes (not shown), there appears to be a decrease (increase) away from the equator for 30-60 day (high frequency;  $< 15$  day) signals. An exception is that the 30-60 day signal over the maritime continent ( $120^{\circ}\text{E}$ ) is relatively weaker at the equator than in the subtropics of both hemispheres.

One may also note an approximate 20 day spectral peak over the Pacific in Fig. 3.1. However, it will not be discussed since the separation between this peak and 30-60 day peak is not so obvious. Furthermore, from the detailed analyses which will be presented later, the 30-60 day and 2-15 day oscillations have distinguishing characteristics and effects in relation to atmospheric interannual variations. Therefore, the focus in this paper will be placed on the OLR spectral signal within those two frequency bands, i.e., 30-60 days oscillation or low-frequency oscillation (LFO), and 2-15 days oscillation or high-frequency oscillation (HFO).

### 3.2 Frequency Modulation of LFO and HFO

As noted by Murakami et al. (1984, 1986), the activity of the low-frequency oscillation differs significantly both in dominant frequency and amplitude from one year to another. For example, during the 1982/83 El Nino-Southern Oscillation event, the activity of the low-frequency (30-60 day) oscillation was depressed well below normal and its eastward phase propagation became irregular over the Indian Ocean and western Pacific. Thus, it is important to investigate the interannual variability of the 30-60 day oscillations.

In addition, Murakami et al. (1986) discussed the variation of high-frequency difference assembly during a longer time period in conjunction with the energy dispersion phenomenon. Subsequently, Nakazawa (1986) and Yamazaki and M. Murakami (1987) found that the HFO shows an amplitude modulation with a period of 30-60 days. The results cited above are indicative of the strong interaction between intraseasonal perturbations and interannual variations in the atmosphere, which is likely associated with global-scale circulation changes. Next, the seasonal and interannual variation of LFO and HFO, using OLR spectra, are presented.

#### 3.2.1 Low-Frequency Oscillation

Figure 3.2 depicts the time dependence of OLR spectra,

OLR POWER EXCEEDING SEASON MEAN

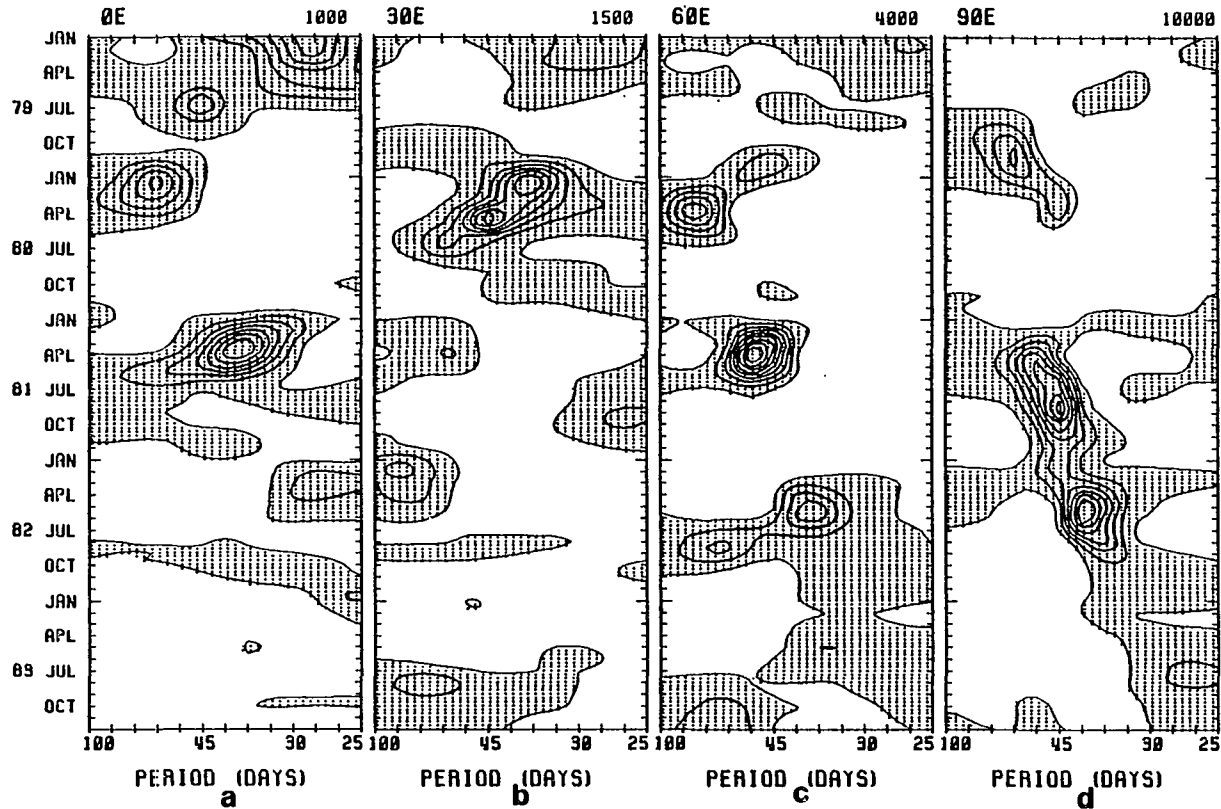


Fig. 3.2 Time dependence of power spectral amplitude of equatorial OLR<sup>1</sup> averaged between 5°S and 5°N for period range of 25 to 100 days. Unit is  $W^2m^{-4}day$ . Contour intervals are shown above the top-right corner of each diagram. Only positive anomalies (exceeding the season mean) are shown. The grid points shown are same as in Fig. 3.1.

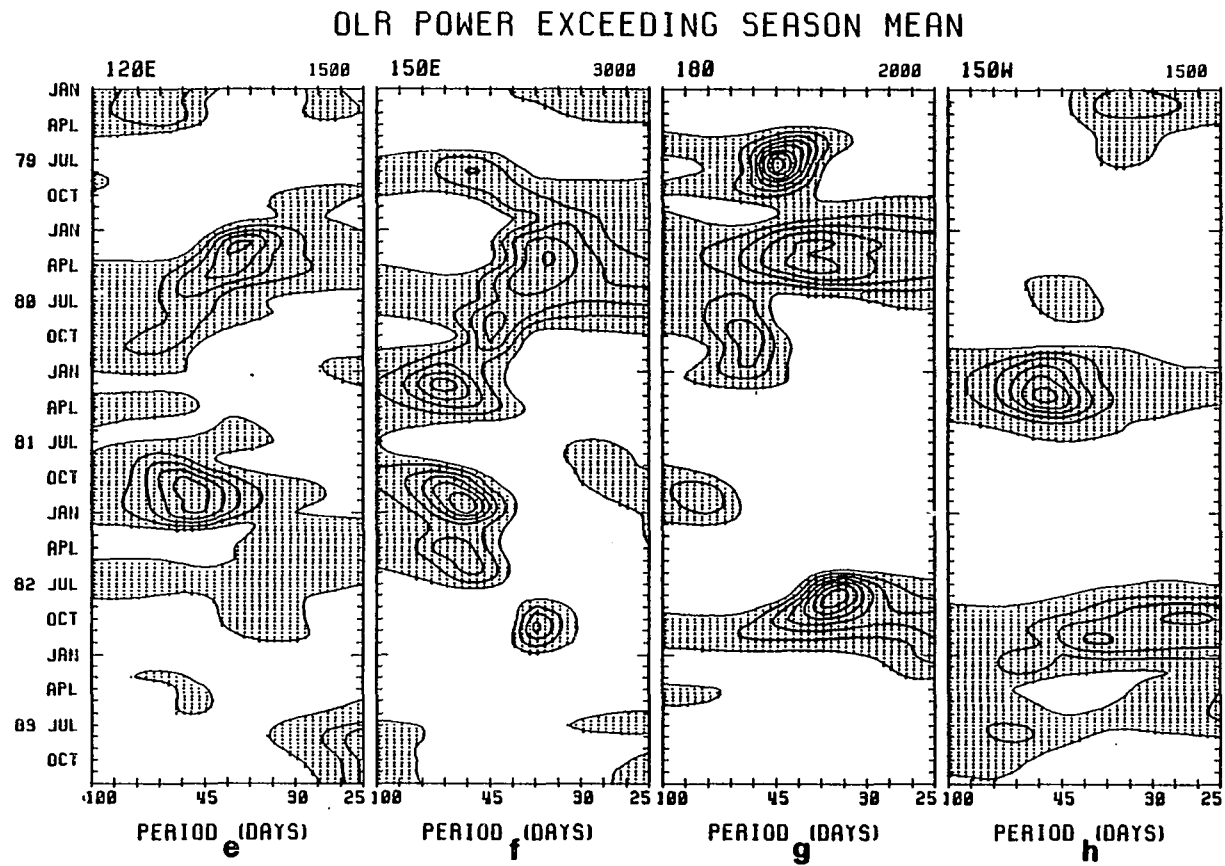


Fig. 3.2 (continue)

OLR POWER EXCEEDING SEASON MEAN

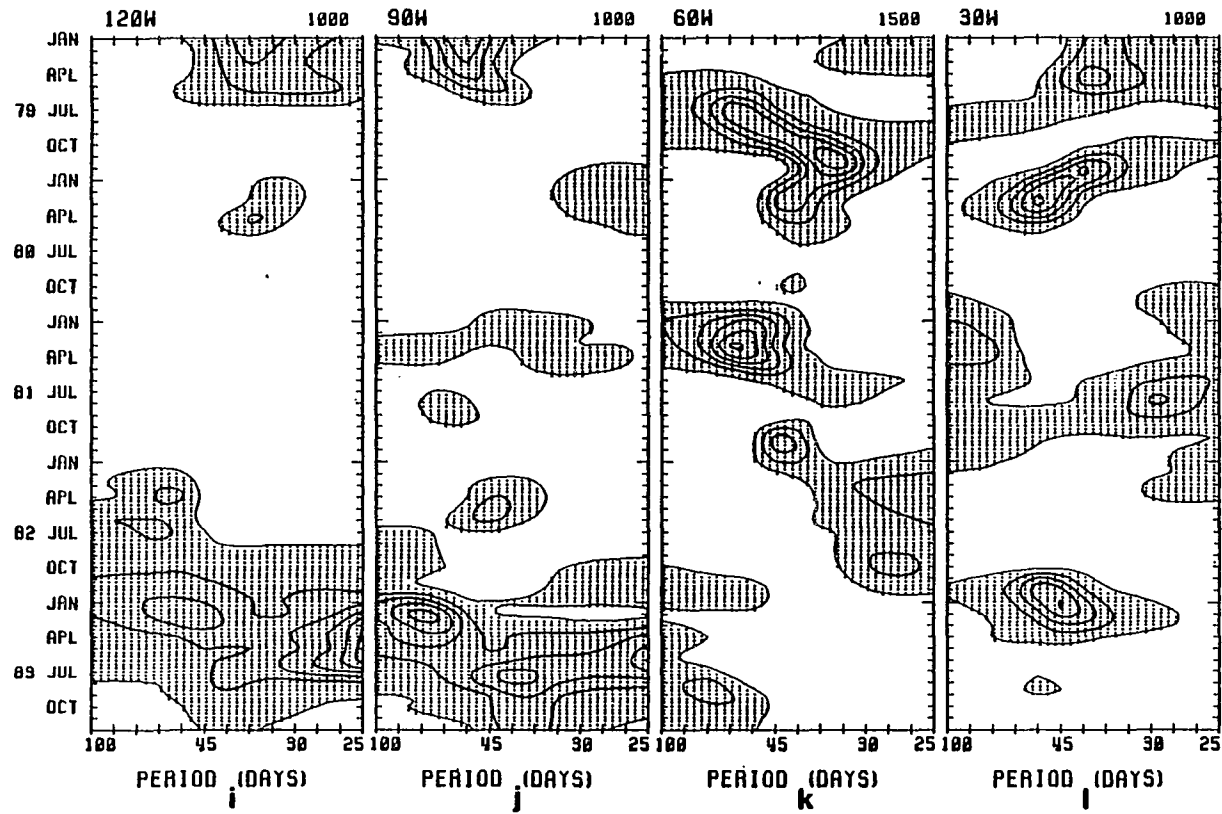


Fig. 3.2 (continue)

exceeding<sup>2</sup> the five-year normal annual mean, from a period of 25 to 100 days along the equator. Over the Indian Ocean (Figs. 3.2c and 3.2d) and the western Pacific (Figs. 3.2e, 3.2f, and 3.2g), where the LFO is most pronounced and where its eastward and northward phase propagation is well defined, the dominant period decreases or increases with time between approximately 30 and 60 days. For example, over the eastern Indian Ocean (90°E, Fig. 3.2d) the dominant period decreased from about 60 days in January 1981 to about 30 days in December 1982. A reverse case is shown in Fig. 3.2f, where the period of the strongest signal increases from about 30 days in October 1979 to about 60 days in May 1981. A similar situation, although more irregular, can be seen over the maritime continent (120°E, Fig. 3.2e) and the date line (180°E, Fig. 3.2g). This phenomenon indicates the existence of frequency modulation in the atmosphere. The modulating period of the LFO is roughly 2-5 years over the equatorial Indian Ocean, the maritime continent and the western Pacific. Outside of

---

<sup>2</sup>Here, a caution must be drawn that presenting only spectra greater than annual cycle can be dynamically biased. However, examination of spectra less than annual cycle shows no particular interested feature. For convenient access to discussion, negative anomalies have been eliminated.

OLR POWER EXCEEDING SEASON MEAN

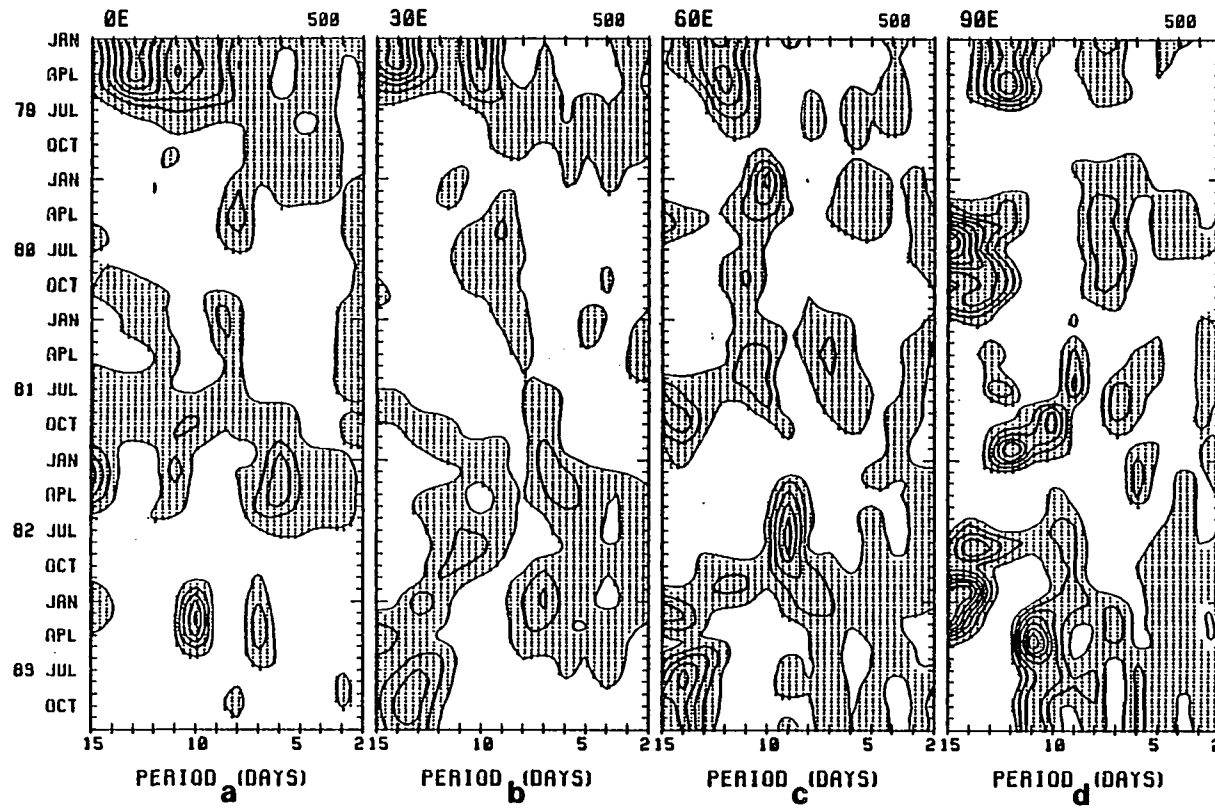


Fig. 3.3 As in Fig. 3.2, except for 2-15 day period.

OLR POWER EXCEEDING SEASON MEAN

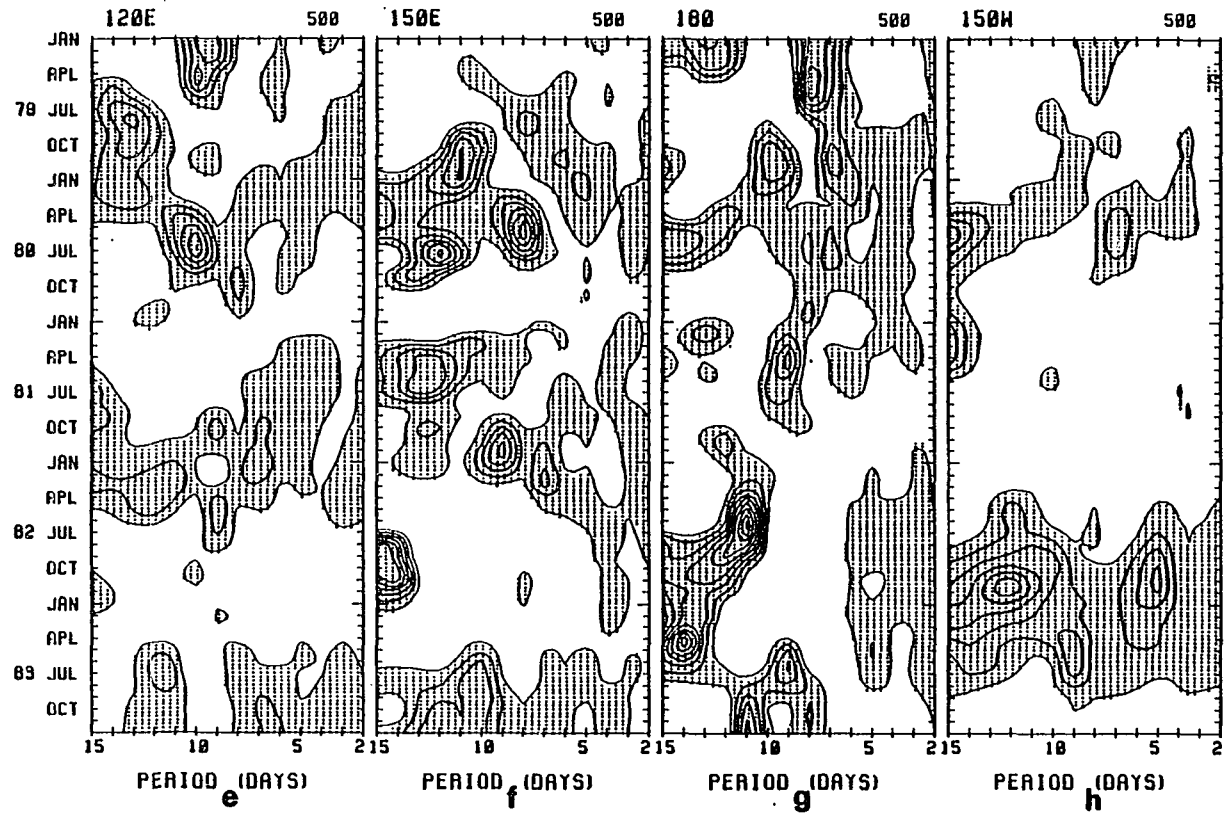


Fig. 3.3 (continue)

OLR POWER EXCEEDING SEASON MEAN

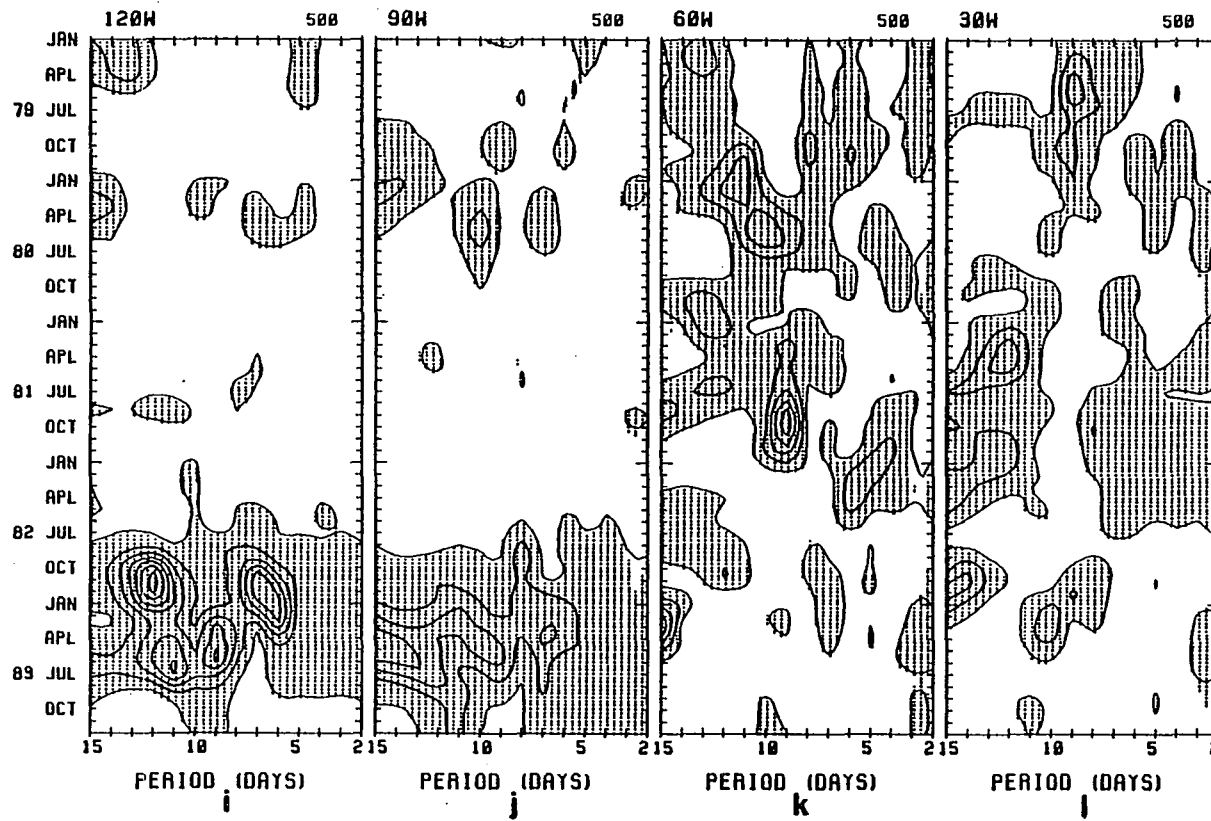


Fig. 3.3 (continue)

these regions, the frequency modulation phenomenon is relatively ill organized. In other words, the time scales of modulated signals (approximately 45 days=1.5 months) and of the modulating signals (about 3-7 months, e.g., Figs. 3.2a and 3.2b) are of same order, and are not distinguishable from each other due to the high nonlinearity.

Another interesting feature in Fig. 3.2 is that the LFO signal is greatly enhanced over the central and eastern Pacific during the 1982/83 ENSO event for all frequencies.

### 3.2.2 High-Frequency Oscillation

On the interannual time scale, the frequency modulations of short-period activities, as revealed in Fig. 3.3, are not as clear as those of the 30-60 day oscillations. A relatively well-defined case can be found at the date line during the 1982/83 ENSO (Fig. 3.3g). However, one may note that there are many occasions of the strongest perturbations decreasing or increasing their period within several months in Fig. 3.3. This reflects much shorter frequency modulation periods for 2-15 day activities, which are not properly described in the monthly data set used here. A complete discussion of frequency modulation of 2-15 day disturbances needs a more sophisticated analysis method and a denser data set.

A very striking feature in Fig. 3.3 is the greatly enhanced activity for all frequencies over the equatorial

central and eastern Pacific within the ENSO period (Figs. 3.3h, 3.3i and 3.3j). A thorough examination of this point will be presented in a later section.

### 3.2.3. Discussion

The frequency modulation phenomenon explored above can be viewed as an energy conversion process in the frequency domain. In Figs. 3.2 and 3.3, maximum centers or ridges represent large convective energy in the corresponding frequencies. The gradual frequency change of these centers means that the large convective energy is continuously converted from one frequency to the next. This is the so-called energy cascade phenomenon. However, this phenomenon is not important over the equatorial central and eastern Pacific during the 1982/83 ENSO, since all frequencies have large OLR spectral amplitude as mentioned previously.

### 3.2.4. Two Components of ICA

Thus far, it has been revealed that frequency modulations for 30-60 day and 2-15 day oscillations have different character, and a cascade of time-scale interaction possibly exists in the atmosphere. Turning one's attention to Figs. 3.2 and 3.3 again, a common feature is an interannual change of maximum spectral amplitude when considering the frequency band (about 30-60 day in Fig. 3.2 and 2-15 day in Fig. 3.3) as a whole. This is the amplitude

modulation phenomenon. Two components for intraseasonal convective activity are therefore constructed as follows:

$$OLR_S = \int_{\frac{1}{2}}^{\frac{1}{15}} OLR_p(t, f) * f \, df \quad (10)$$

$$OLR_L = \int_{\frac{1}{30}}^{\frac{1}{60}} OLR_p(t, f) * f \, df \quad (11)$$

where  $OLR_S$  represents convective activities with periods of 2-15 days, while  $OLR_L$  for periods of 30-60 days<sup>3</sup>.  $OLR_S$  and  $OLR_L$  will be used to investigate interannual and seasonal variability of intraseasonal activity (in view of amplitude modulation), and their association with the 1982/83 ENSO.

### 3.3. Time-Space Character of $OLR_S$ and $OLR_L$

After summation of OLR spectra over two specific frequency bands, spatial and temporal variations of these two components, i.e.,  $OLR_S$  and  $OLR_L$ , reflect the intensity of variations of the high-frequency (2-15 days) and low-frequency (30-60 days) disturbances, respectively. From now on, the emphasis will be on those two components when discussing intraseasonal disturbance activity.

---

<sup>3</sup>These averaged spectra are approximately proportional to the standard deviation of  $\bar{OLR}$  and  $OLR^*$  during the same five-month period.

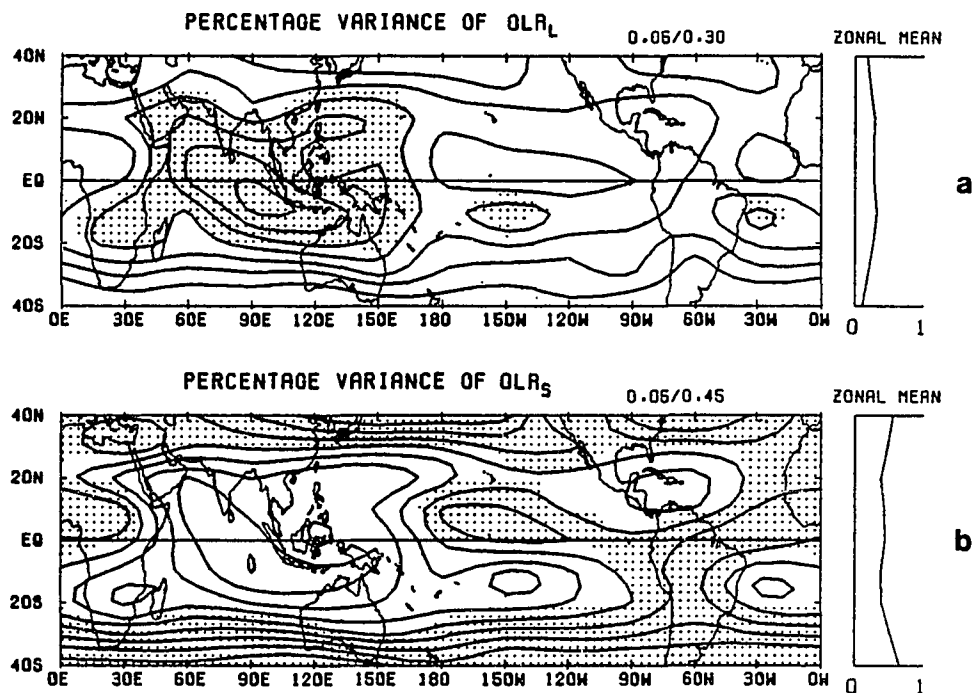


Fig. 3.4 Percentage of spectra amplitude explained by 30-60 day period band  $OLR_L$  (a) and 2-15 day period band  $OLR_S$  (b). Intervals are 0.05 and shading are larger than 0.3 (0.45) for 30-60 (2-15) day. Zonal means are shown at the right. See text for definition of  $OLR_L$  and  $OLR_S$ .

### 3.3.1. Percentage Variance of OLR<sub>S</sub> and OLR<sub>L</sub>

The OLR<sub>S</sub> and OLR<sub>L</sub> components exhibit different spatial patterns, as mentioned above. Shown in Fig. 3.4 are the percentage of spectra explained by OLR<sub>L</sub> and OLR<sub>S</sub> modes, respectively. Over 30% of the total OLR power is occupied by OLR<sub>L</sub> in the Indian Ocean and the western Pacific between 20°S and 20°N. A maximum center of 45% is found over the eastern Indian Ocean (Fig. 3.4a). This agrees well with the previous conclusions by Lau et al. (1985) and Murakami et al. (1986).

On the other hand, a large percentage of variance occupied by OLR<sub>S</sub> components is over the midlatitudes poleward of 25° (Fig. 3.4b). This may be attributed to the cloudiness associated with frequent passage of synoptic-scale cyclones in prevailing westerlies. Another maximum in Fig. 3.4b is over the central Pacific north of the equator, which extends eastward along the equator to Brazil, the Atlantic, and northwestern Africa. This is probably due to frequent short-period activity over the Near Equatorial Convergence Zone (NECZ) during the 1982/83 ENSO event. Over the western Pacific, the variance of OLR<sub>L</sub> and OLR<sub>S</sub> component are almost equally important. This is in agreement with Lau's (1986) analysis. However, the maximum center of OLR<sub>S</sub> variance over the central Pacific is much stronger with comparison to Lau's results, and is probably due to the dominant influence of the 1982/83 ENSO

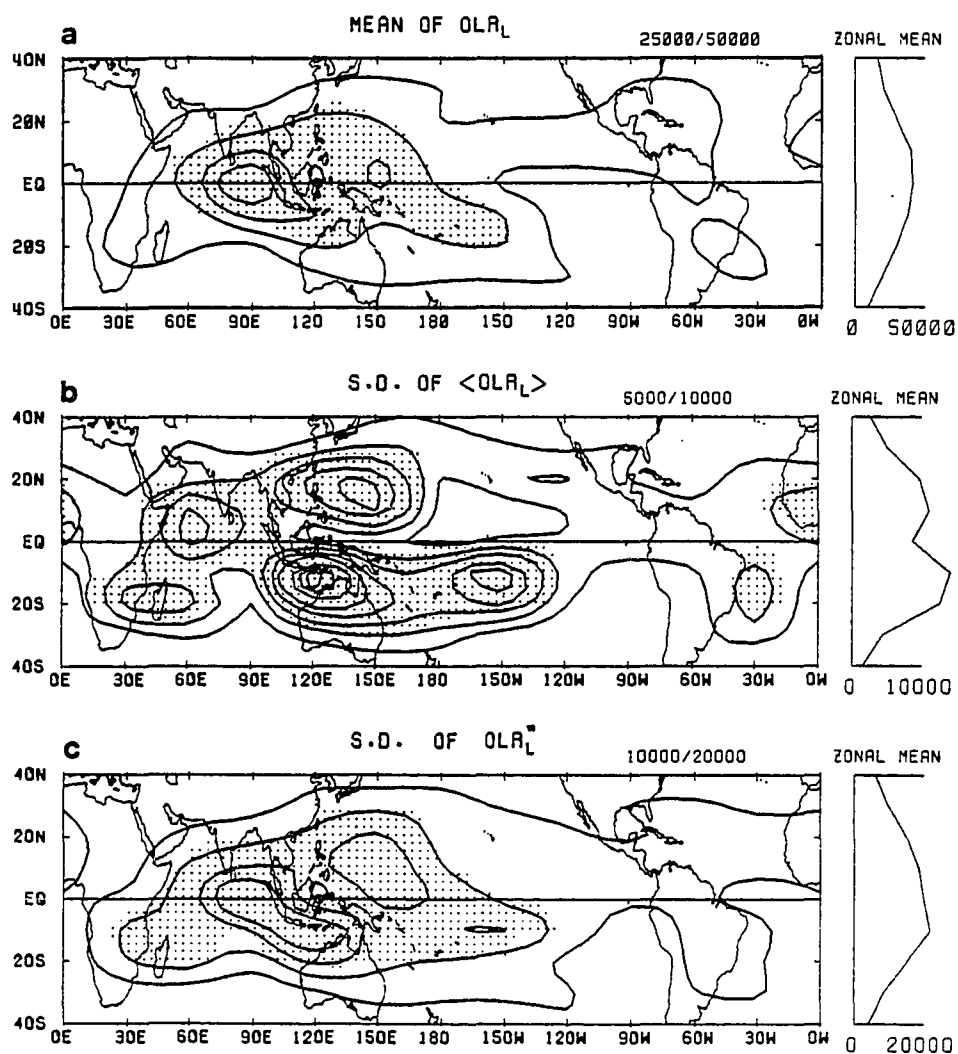


Fig. 3.5 (a): Five-year mean of  $OLR_L$ . Unit is  $W^2m^{-4}day$ . Intervals and shading are shown above the top-right corner of the figure, i.e., 2500 and greater than 5000 units, respectively. (b): As in (a), except for standard deviation of  $\langle OLR_L \rangle$ . See text for definition of  $\langle OLR_L \rangle$ . (c): As in (b), except for  $OLR_L''$ , as defined by eq. (3). The zonal means are shown at the right side of each figure.

variation over the Pacific within the data period of this study.

The zonal mean shown in Fig. 3.4 illustrates a general tendency of  $OLR_L$  to be large over the equatorial region, while  $OLR_S$  is large over the midlatitudes. Overall, these two components comprise about 80-90% of the total OLR spectra.

### 3.3.2. Variation of $OLR_L$

The 5-year mean field of  $OLR_L$  is depicted in Fig.

3.5a. The very large  $OLR_L$  areas, which reflect the most pronounced 30-60 day oscillations, are confined to the Indian Ocean and the western Pacific. A maximum center is found over the equatorial eastern Indian Ocean ( $90^\circ E$ ). A second maximum is located at  $150^\circ E$  along the equator. This result reconfirms the dipole pattern (Lau, 1985) of the 30-60 day oscillation.

The standard deviation of the normal annual cycle of  $OLR_L$  describes very different spatial distributions (Fig. 3.5b). Maxima exist over the subtropics of both hemispheres, i.e., the northeastern Pacific and northern Australia to south-central Pacific. Therefore, the annual variations of intensity of the 30-60 day oscillation are extremely large over these areas compared with elsewhere. In other words, the amplitude modulation of  $OLR_L$  by the annual cycle is very strong in the Australia monsoon region

and the northwestern Pacific where tropical cyclones occur most frequently. Another relatively large value area in Fig. 3.5b is over the western Indian Ocean along the east coast of Africa. All centers are away from the equator (Fig. 3.5b). Comparing Figs. 3.5b and 3.5c, one notes that in general the annual component of  $OLR_L$  is much smaller than the interannual component.

By definition,  $OLR_L''$  mainly contains interannual components of  $OLR_L$ . The standard deviation of  $OLR_L''$  shown in Fig. 3.5c exhibits a large value in two zones stretching from dipole centers: the central Indian Ocean to northern Australia, and the western Pacific to the northwestern Pacific. Thus, the variability of the 30-60 day oscillation is essentially of an interannual character along the equator. From a further inspection of Figs. 3.5b and 3.5c, an interesting feature is that  $\langle OLR_L \rangle$  and  $OLR_L''$  have the same intensity over the Australia monsoon region, while,  $OLR_L''$  dominates over the Indian monsoon area.

Temporal variations of  $OLR_L$  along the equator are presented in Fig. 3.6. The normal annual component  $\langle OLR_L \rangle$  is also plotted as a dashed line. Two maximum interannual peaks are found over the Indian Ocean ( $60^\circ\text{E}$ , Fig. 3.6c;  $90^\circ\text{E}$ , Fig. 3.6d) during the summer of 1981 and 1982, respectively. The latter occurs just prior to the onset of the 1982/83 ENSO event. This point will be discussed in detail later. Disregarding the intensity, the interannual

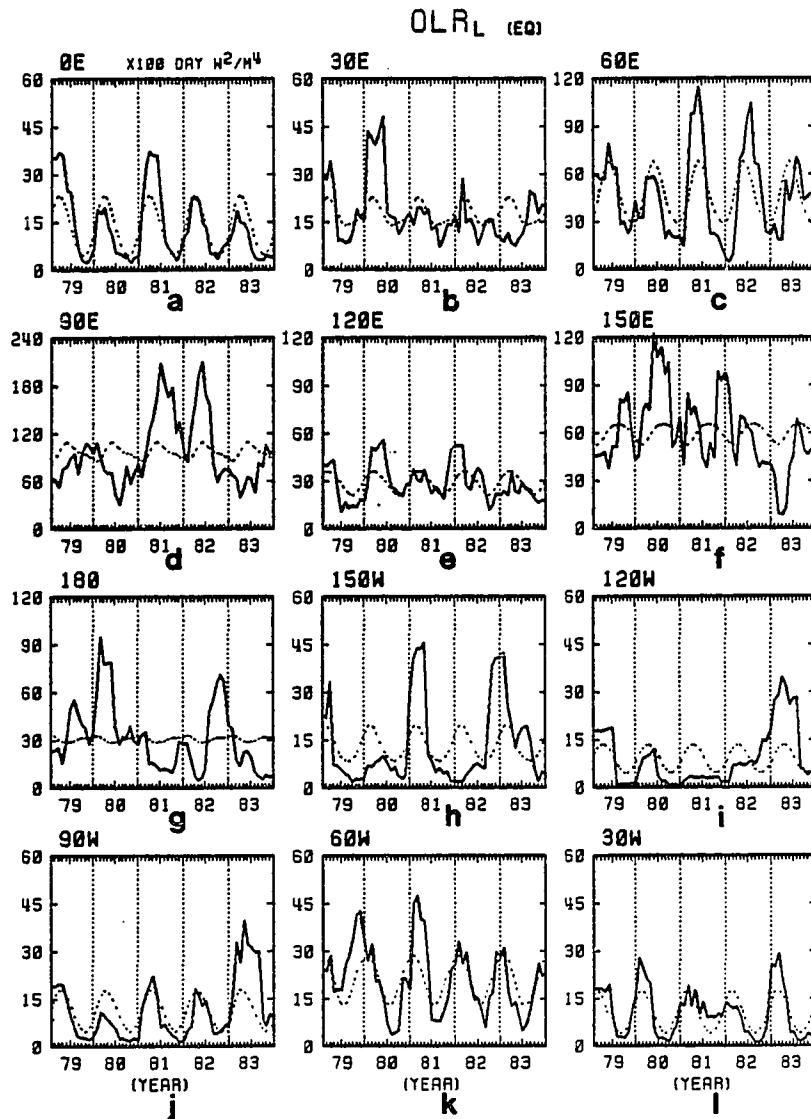


Fig. 3.6 Time series of OLR<sub>L</sub> (solid) and its normal annual cycle (dash) along the equator. Unit is  $10^2 \text{ W}^2 \text{ m}^{-4} \text{ day}$ . The grid points shown are same as in Fig. 3.1.

variability of  $OLR_L$  is predominant over the equatorial central and eastern Pacific (Figs. 3.6g-j).

During the 1982/83 ENSO period, an  $OLR_L$  peak over the eastern Pacific ( $90^\circ W$ , Fig. 3.6j) in the early summer of 1983 can be traced to the central Pacific ( $180^\circ$ , Fig. 3.6g) in the early winter of 1982, to some degree. However, an  $OLR_L$  peak at the eastern Indian Ocean ( $90^\circ E$ , Fig. 3.6d) during the summer of 1982 somewhat lost its trace when it migrated eastward. There is no obvious continuity along the equator over the western Pacific during the fall of 1982 (Figs. 3.6e and 3.6f). This may reduce the detectability of an interannual mode over the central and eastern Pacific during ENSO. In Fig. 3.6, a component with a time scale between a season and one year can also be seen (e.g., Fig. 3.6f) in addition to the normal annual cycle and interannual components.

### 3.3.3. Variation of $OLR_S$

The mean distribution of  $OLR_S$  is shown in Fig. 3.7a. Values are large over the tropical Pacific north of the equator and the south central Pacific, reflecting a substantial number of transient disturbances over the Inter-Tropical Convergence Zone (ITCZ) or the NECZ, and the South Pacific Convergence Zone (SPCZ). The mean  $OLR_S$  values are also large over Japan, the east coast of the United States, and from South America to the southeastern

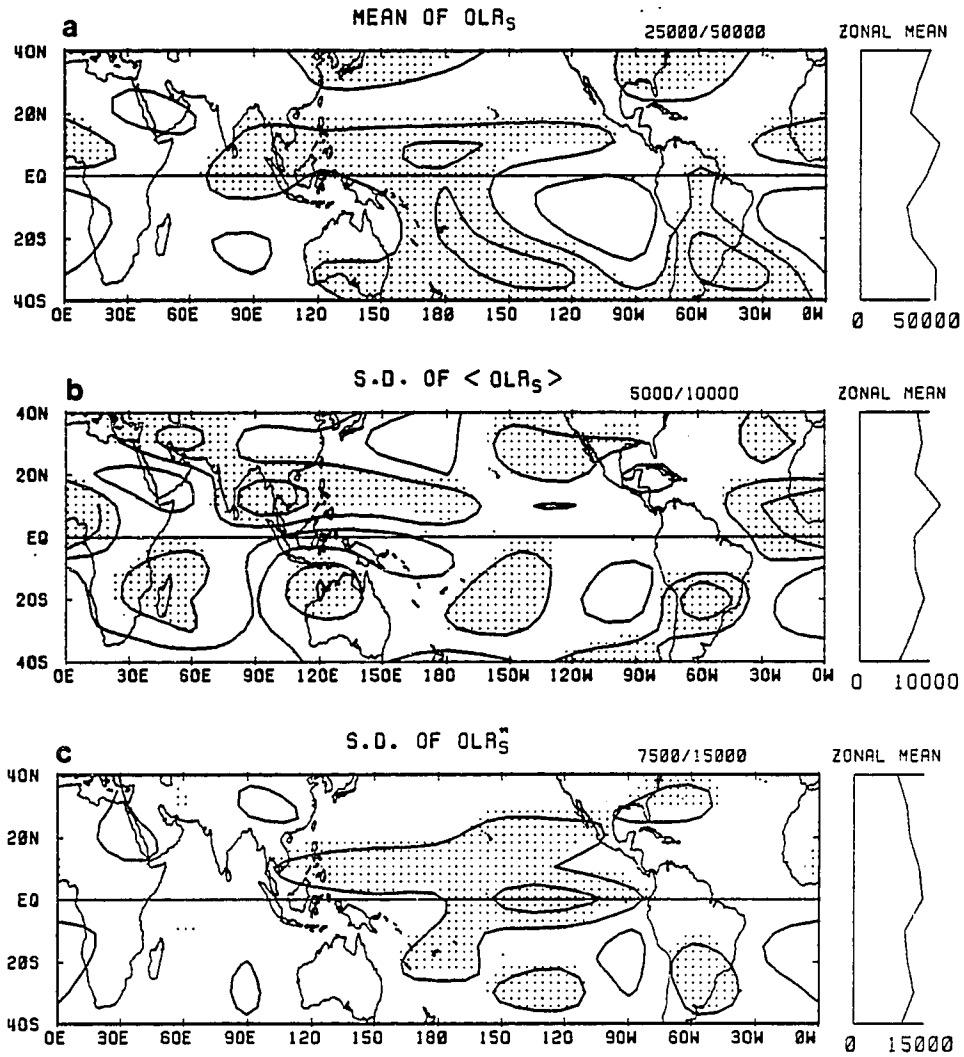


Fig. 3.7 As in Fig. 3.5, except for  $OLR_L$ .

Atlantic, where there is a correspondence to the core areas of the upper-level westerly jet. These results suggest the different natures of transient convective disturbance activities over the tropical region and over midlatitudes. Nevertheless, the mean pattern of short-period activities ( $OLR_S$ ) fairly well describes the global planetary-scale circulation components.

The intensity of the annual components of  $OLR_S$ , as shown in Fig. 3.7b, probably reflects the seasonal changes of the thermal continent-ocean contrast. For example, a maximum center over southern Asia may result from the Indian and Asia monsoon variability. Another large value centered over the tropical Atlantic and western Africa north of the equator is possibly due to the thermal effect of the Africa desert. Also relatively large values in Fig. 3.7b over the south and north central Pacific are mainly due to the 1982/83 ENSO. The annual change of  $OLR_S$  activities is not important over the equator.

Unlike the annual cycle, interannual components of  $OLR_S$  are confined to the Pacific Ocean near the equator, as shown in Fig. 3.7c. The maximum is over the equator from  $160^{\circ}W$  to  $100^{\circ}W$ . This is almost entirely due to the 1982/83 ENSO event. Let us look at the differences between  $OLR_S$  and  $OLR_L$ . For  $OLR_L$  mode (Fig. 3.5), the region with high mean value coincides with the area of large standard deviation of interannual components of  $OLR_L$  (comparing

Figs. 3.5a with 3.5c). This is an indication of that the interannual modulation of the 30-60 day oscillation is mainly due to the frequency interference of the LFO itself, implying more degree of freedom for the 30-60 day mode to interact with interannual components of atmospheric variation. However, that is not true for  $OLR_S$  mode (Figs. 3.7a and 3.7c). The maximum standard deviation of interannual components of  $OLR_S$  overlays the minimum value area of mean  $OLR_S$ . This may imply that interannual variations of  $OLR_S$  are greatly affected by a planetary-scale circulation anomaly on interannual time scale. Therefore, the  $OLR_L$  and  $OLR_S$  modes must have different natures in regard to ENSO-type interannual variability of atmosphere-ocean coupled system.

The time series of  $OLR_S$  and its normal annual cycle along the equator (Fig. 3.8) give support to the previous argument. It can be immediately seen that the largest interannual variations are over the equatorial central and eastern Pacific (Figs. 3.8h, 3.8i, and 3.8j). During the 1982/83 ENSO event, a very large peak of  $OLR_S$  first occurred at  $150^{\circ}W$  in the winter of 1982, and then propagates eastward to  $90^{\circ}W$  in the early summer of 1983. No obvious trace can be found near the date line (west of  $150^{\circ}W$ ) along the equator. Within the non-ENSO period,  $OLR_S$  activity are much more depressed over the central and

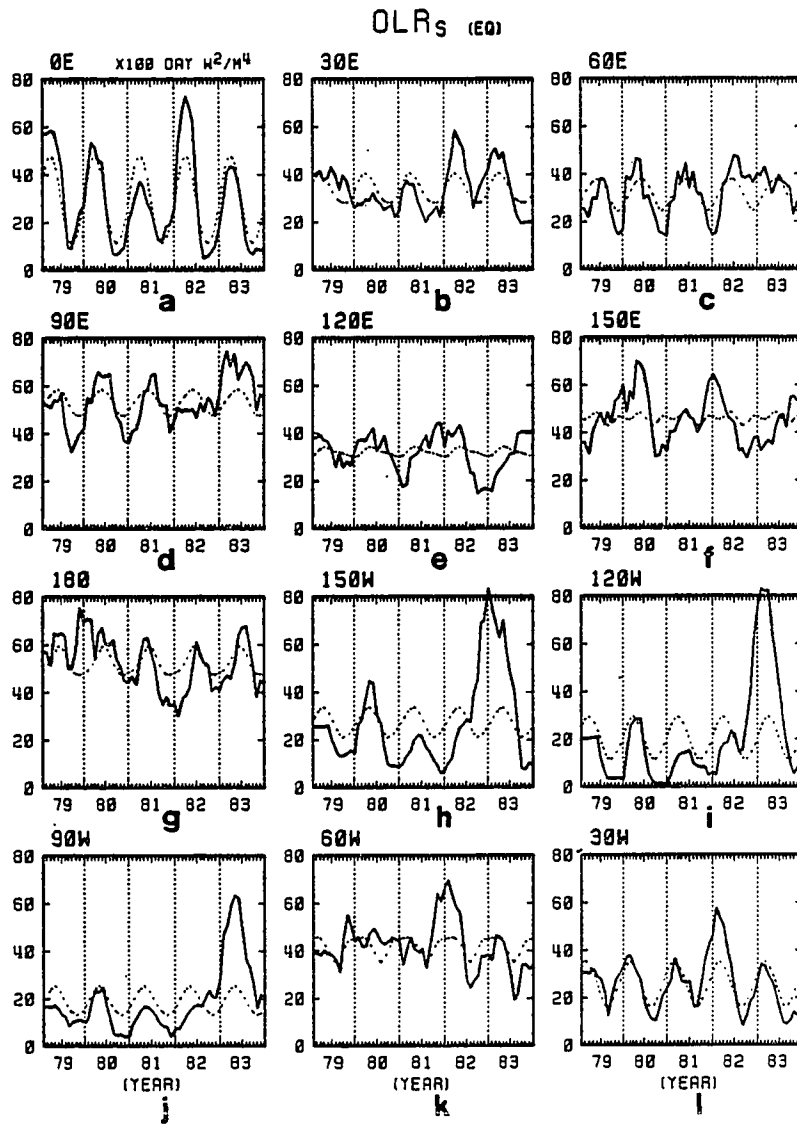


Fig. 3.8 As in Fig. 3.6, except for OLR<sub>S</sub>.

eastern Pacific, where the cold water area (low SST) is, than in any other areas.

Besides the normal annual cycle and interannual components, signals of periods of less than one year are also quite substantial in Fig. 3.8, especially over the western Pacific (Figs. 3.8e, 3.8f, and 3.8g). In the next section, a separation between interannual components and seasonal components will be made in order to address their different roles in the ENSO phenomenon.

#### 4. Interannual and Seasonal Variation of Intraseasonal Convective Activity

##### 4.1. An Overview

In order to investigate the relationship between intraseasonal convective activity ( $OLR_S$  and  $OLR_L$ ) and variation in convection itself, the OLR parameter will be included in subsequent discussions. By definition,  $OLR''$  primarily contains interannual components of convection. However, certain parts of the anomalous annual components with interannual time scales, which are not included in a normal annual cycle because of the limitation of the numerical method, are still in  $OLR''$ . Examples have been given in Figs. 3.6 and 3.8 when discussing the time series of  $OLR_S$  and  $OLR_L$ . This anomalous annual component, called seasonal components in this paper, will be separated from interannual components by using Fourier decomposition techniques. For example,  $OLR''(S)$  and  $OLR''(I)$ , signified as the seasonal cycle and interannual components of  $OLR''$ , will be defined as:

$$OLR''(S) = \sum_{m=6}^{20} A \sin \frac{2\pi mt}{T} + B \cos \frac{2\pi mt}{T} \quad (12)$$

$$OLR''(I) = \sum_{m=1}^5 A \sin \frac{2\pi mt}{T} + B \cos \frac{2\pi mt}{T} \quad (13)$$

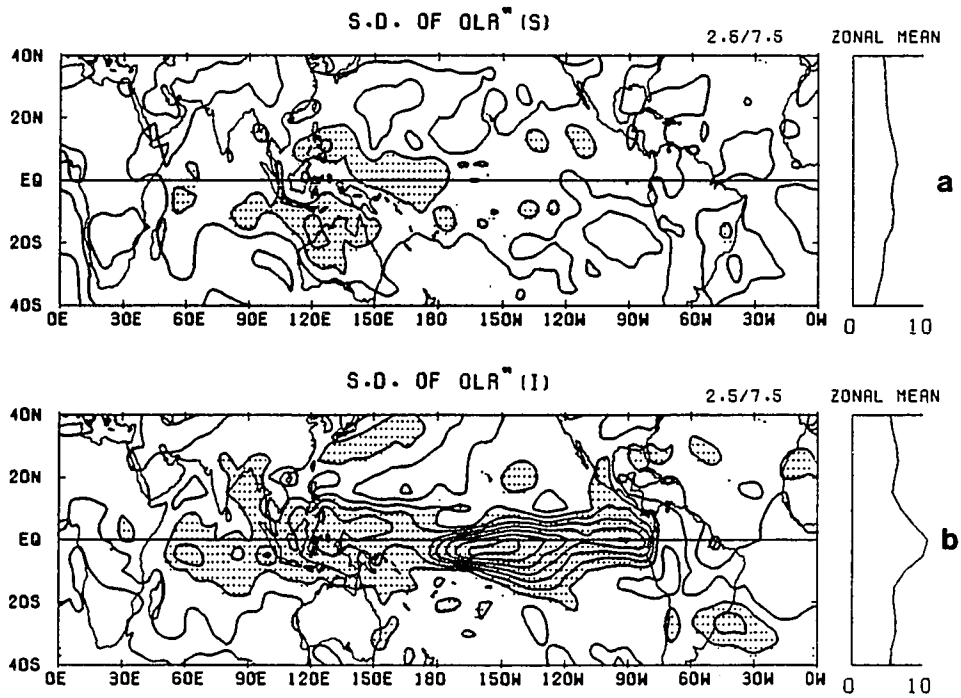


Fig. 4.1 As in Fig. 3.7a, except for  $OLR^{(S)}$  in (a) and  $OLR^{(I)}$  in (b), as defined by the eqs. (12) and (13), respectively.

where A and B are the Fourier coefficient, and are computed from five years of the  $OLR''$  time series. T is the length of sample, i.e., 60 months. The same procedure is applied to the quantities  $OLR_S''$  and  $OLR_L''$  yielding  $OLR_S''(S)$ ,  $OLR_S''(I)$ ,  $OLR_L''(S)$ , and  $OLR_L''(I)$ , respectively.

A discussion of the standard deviation pattern of the OLR normal annual cycle (Figure is not shown, refer to Fig. 2 of Lau, 1987) is also presented here for comparison. All the areas where large standard deviations are found are of large seasonal thermal contrast, i.e., continental land masses and the monsoon regions. The largest seasonal variations of OLR over the continental region of western Asia are not likely to be associated with convection alone, but also with changes of surface temperature and snow cover. In the tropics, where changes in OLR are well correlated with convection, large normal seasonal variations of OLR are situated over the Northern Hemisphere summer monsoon region of India and Indochina, the Northern Hemisphere winter monsoon region of Indonesia and Australia, the Amazon, and central Africa.

Figure 4.1a shows the standard deviation of OLR seasonal components. Interestingly, large variations are confined to the western Pacific north of the equator with a leg extending to the date line at the equator, and to northern Australia with the center near Darwin, where are the place being considered important for the onset of ENSO

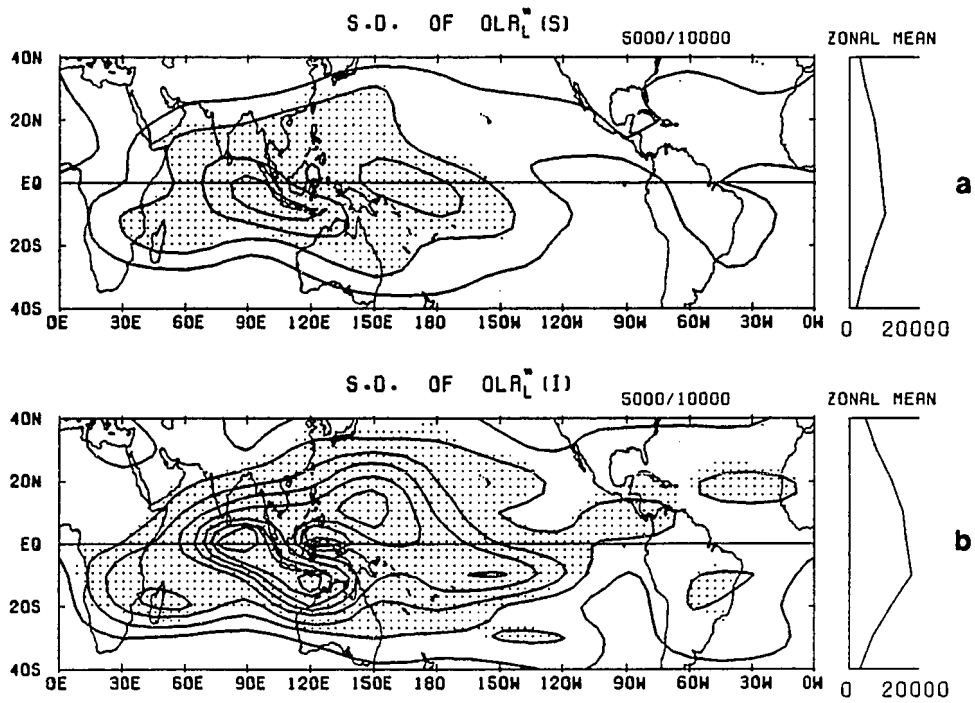


Fig. 4.2 As in Fig. 4.1, except for  $OLR_L^*(S)$  and  $OLR_L^*(I)$ .

events. This means that the mean annual cycle frequently shifts its phase over the equatorial western Pacific where SST remains high. In other words, the normal annual cycle is readily disturbed there. Hence, it is possible that the onset of an ENSO event can be resulted from the abnormal intensification of an atmospheric annual components over the equatorial western Pacific.

The standard deviation of  $OLR''(I)$  is shown in Fig. 4.1b. The strongest variation is located in the central Pacific just south of the equator. This is essentially due to the 1982/83 ENSO event. A second maximum is over the maritime continent north of the equator. A relatively large value area extends all the way from the western Indian Ocean to the west coast of South America along the equator. The spatially coherent feature of interannual  $OLR''(I)$  variations over the equatorial Indian Ocean, western Pacific and central-eastern Pacific is obvious in Fig. 4.1b.

Shown in Fig. 4.2 are standard deviations of  $OLR_L''(S)$  and  $OLR_L''(I)$ . The areas of prominent standard deviations for  $OLR_L''(S)$ ,  $OLR_L''(I)$ , and  $OLR_L''$  are quite similar. However, there are fundamental differences between the variability of the  $OLR_L$  normal annual cycle and the  $OLR_L$  seasonal components (compare Fig. 3.5b with Fig. 4.2a). Therefore, the amplitude modulation of the 30-60 day oscillation with a time scale slightly different from normal annual cycle,

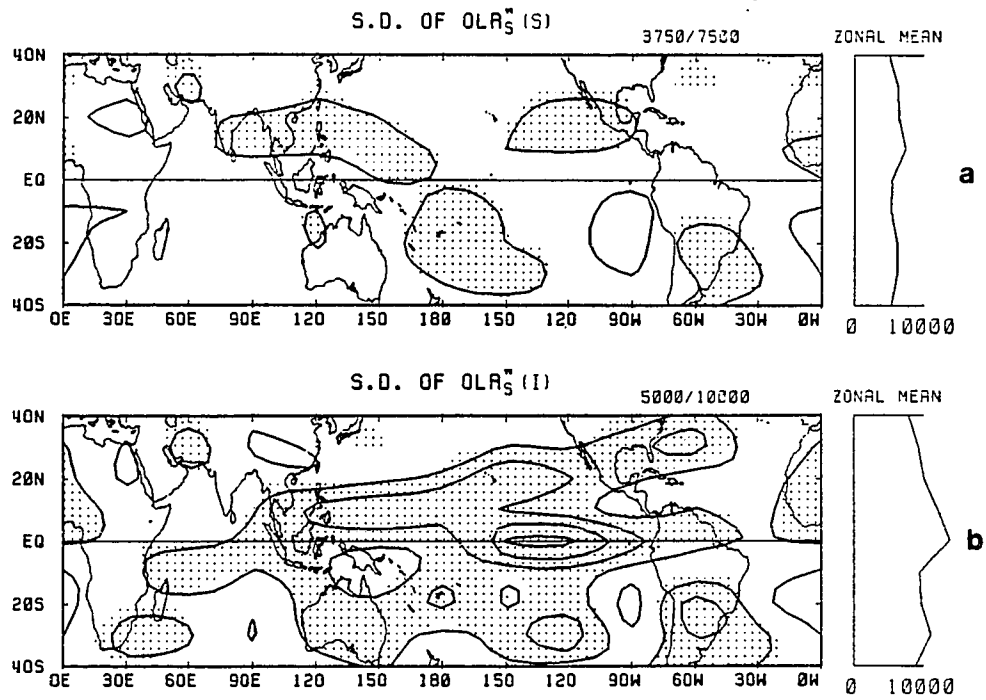


Fig. 4.3 As in Fig. 4.1, except for  $OLR_S^2(S)$  and  $OLR_S^2(I)$ .

although small, can be important enough to enhance inter-annual variations at a certain phase.

Likewise, the standard deviations of  $OLR_S''(S)$  and  $OLR_S''(I)$  are also shown in Figs. 4.3a and 4.3b, respectively.  $OLR_S''(S)$  is much smaller than  $OLR_S''(I)$ . Variations of  $OLR_S''(S)$  in Fig. 4.3a show some similarities to those of  $\langle OLR_S \rangle$  in Fig. 3.7b. The large standard deviations of  $OLR_S''(S)$  are mainly confined to active tropical cyclone areas except for a region over the southeast coast of South America (Fig. 4.3a). This result may reflect irregular seasonality of tropical cyclones. Variability of  $OLR_S''(I)$  shown in Fig. 4.3b are basically the same as those shown in Fig. 3.7c for  $OLR_S$ .

## 4.2. Convection

### 4.2.1. Interannual Variation

The spatial and temporal variability of interannual convection can be illustrated by an empirical orthogonal function (EOF) analysis of the  $OLR''(I)$  components. Depicted in Fig. 4.4 are the first two EOF modes and their time coefficients. The Southern Oscillation Index (SOI), as defined by the difference in surface pressure between Easter Island and Darwin, Australia, is also shown in Fig. 4.4c for the same period. The first EOF mode (Fig. 4.4a) typically resembles the El-Nino and Southern Oscillation

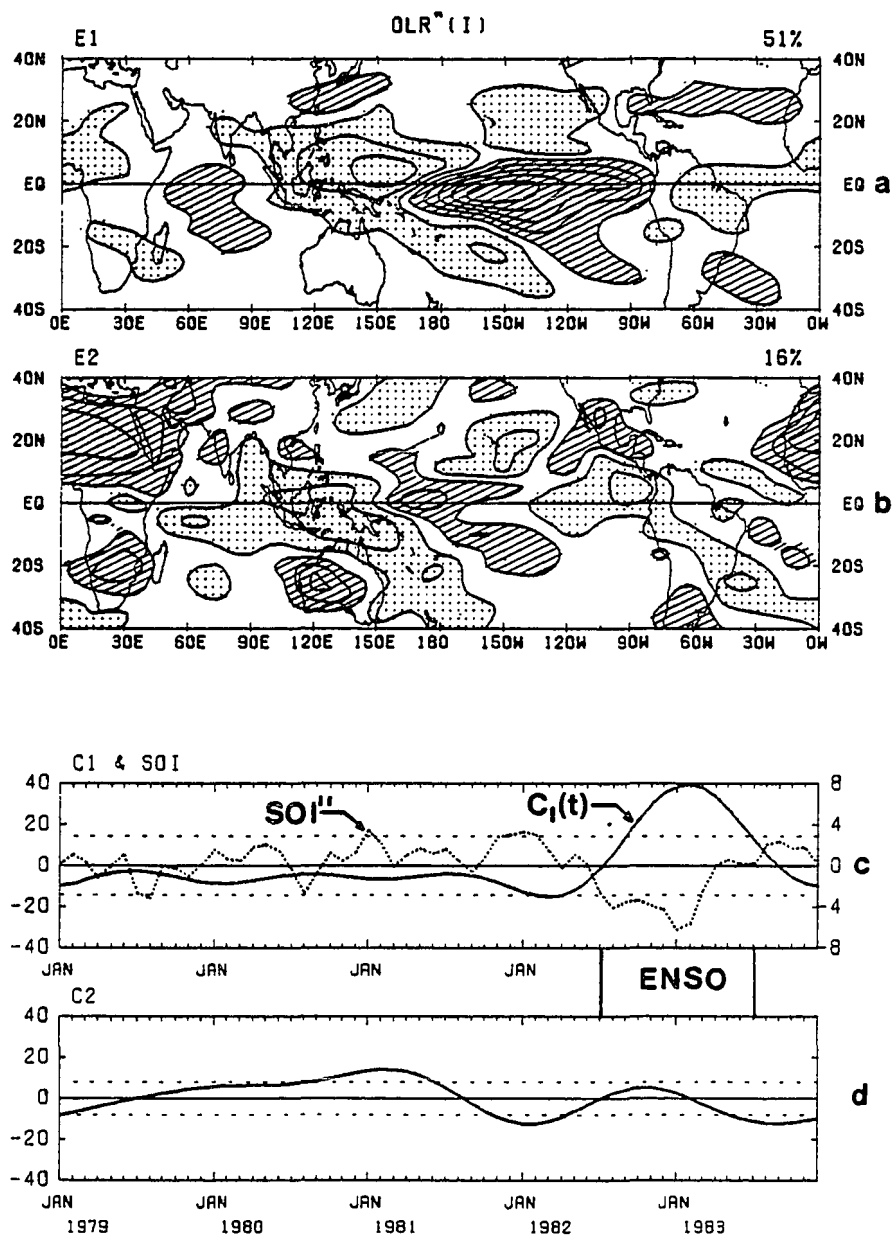


Fig. 4.4 The first two EOF eigenvectors  $E_1$  (a) and  $E_2$  (b) for  $OLR''(I)$ , over the five years of 1979-83. Intervals are 0.05 (non-dimensional) with light mesh (hatching) indicating regions of greater (less) than 0.025 (-0.025); no zero line. The fractional variance of each mode is shown in the top-right corner of the diagram. The time series of eigenmode coefficients  $C_1(t)$  and  $C_2(t)$  are shown in (c) and (d).

(ENSO) pattern described by Rasmusson and Carpenter (1982), as well as the non-ENSO pattern, since the time coefficient  $C_1(t)$  can be either positive or negative (Fig. 4.4c). When the  $C_1(t)$  reaches the maximum (January 1983), the  $E_1$  Pattern represents mid-ENSO, the extreme of ENSO state, of the 1982/83 event. When the  $C_1(t)$  has the minimum (for example, January 1982) the  $E_1$  pattern describes the extreme of non-ENSO state, or so-called anti-ENSO<sup>4</sup> phase. The  $C_1(t)$  shows very good correlation (-0.74) with SOI". This is highly significant at the 95% confidence level with 20 degrees of freedom, i.e., one third of the total months in five years which reflects the three-month running mean applied. During the period from the summer 1982 to the summer 1983, the  $C_1(t)$  is largely positive, the  $E_1$  pattern therefore describes the 1982/83 ENSO event.

From Fig. 4.4a, one can see a "wave number two"-like feature over the equatorial zone with the major action

---

<sup>4</sup>This statement of anti-ENSO has been drawn solely from analysis of equatorial convection and winds, therefore, does not indicate the 'cold event' in the Pacific from oceanographic point of view. In fact, from analysis of SST (Murakami, 1988) the possible 'cold event' before the 1982/83 ENSO can be defined from the early Summer to Fall of 1981.

centered over the central-eastern Pacific, and its counterpart situated over the maritime continent-western Pacific. Two centers, although much weaker, are located over the Indian Ocean and the Amazon-Atlantic-northeastern Africa region. In other words, the  $E_1$  mode basically has a dipole pattern over the equatorial Pacific. Interestingly, Fig. 4.4a exhibits anomalous interannual convection over the equatorial regions out of phase with those over subtropics. A further inspection of Fig. 4.4a, reveals that when convection dominates over the central-eastern Pacific during the ENSO period ( $C_1(t) > 0$ ), there is also above normal convection over the Indian Ocean and eastern Asia-southern Japan region, and below normal values over all monsoon regions.

The interannual variance explained by the first EOF mode is 51%. Therefore, the  $E_1$  pattern in Fig. 4.4a resembles the dominant component of interannual variations. In other words, ENSO events account for more than half of the short-term climatological variation. Because of the extremely large fractional variance of the first EOF mode, it turns out that the major mode of interannual convection

---

<sup>5</sup>Here, the steady state only refers to two possible spatial patterns described by the first eigenmode together with its time coefficients, and by no means satisfies any criterion.

(ENSO pattern) is of a stationary character, which can be viewed as two steady states<sup>5</sup> of short-term climates, i.e., ENSO state and non-ENSO state. However, occurrences of ENSO events are about every 2-7 years according to previous studies. This means that the non-ENSO steady state with considerable perturbations must last for more than two years. These superimposed perturbations might significantly disturb the non-ENSO state sometime, and probably determines whether extreme phase (anti-ENSO) of non-ENSO steady state appears or not. Those perturbations can be attributed to seasonality which also can be regarded as two steady states (the summer pattern and winter pattern) on a much shorter time scale as compared with ENSO recurrence. From this point of view, there exist multiple time-scale steady states in the atmosphere.

A comparison of Figs. 4.4a and 4.4b shows the first two EOF patterns ( $E_1$  and  $E_2$ ) are nearly quarter phase different over the equatorial Indian Ocean and Pacific, although the fractional variance of  $E_2$  (16%) is much smaller than that of  $E_1$  (51%). A similar type of phase difference between  $C_1(t)$  in Fig. 4.4c and  $C_2(t)$  in Fig. 4.4d is also apparent after the winter of 1981. This indicates a slow eastward migration of interannual convection from the eastern Indian Ocean to the eastern Pacific, i.e., a transition from a non-ENSO steady state to an ENSO steady state. Another important feature in Fig. 4.4b is

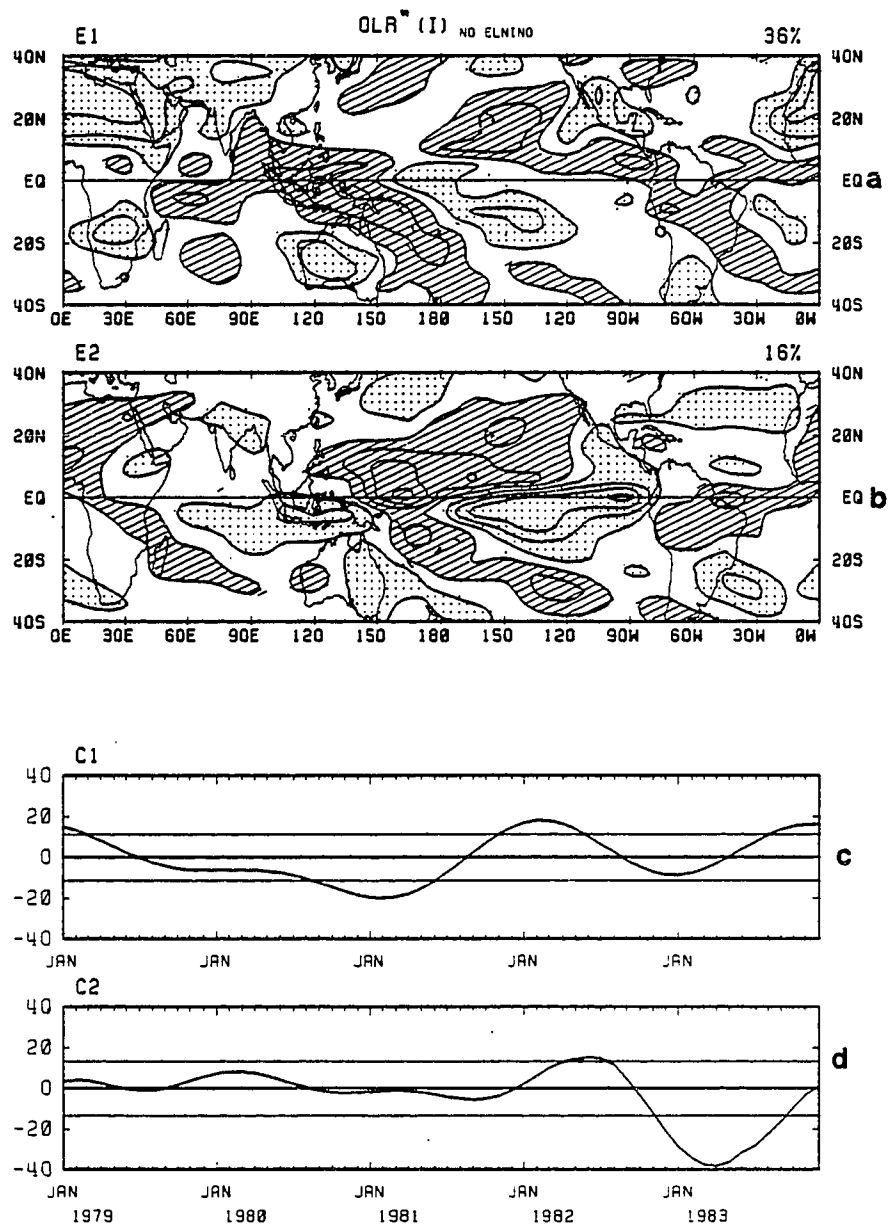


Fig. 4.5 As in Fig. 4.4, except for the OLR(I) data set excluded the 1982/83 ENSO period (July 1982 - June 1983). Time coefficients over the ENSO period are the projection of OLR(I) on the corresponding spatial EOF modes.

the largest action center situated over the African desert region, reflecting a considerable interannual component of convection.

In order to investigate the regularity of ENSO pattern in climate variations, the EOF analysis is also applied to the data set in which the 1982/83 ENSO period (July 1982 - June 1983) has been removed. The results are presented in Fig. 4.5 for the first two EOF modes. The temporal variations ( $C_1(t)$  and  $C_2(t)$ ) during the ENSO period represent the projection of the actual OLR<sup>"(I)</sup> anomaly onto the spatial patterns shown in Figs. 4.4a and 4.5b.

From a comparison of Figs. 4.4 and 4.5, one can immediately see similarities between Figs. 4.4a (4.4b) and 4.5b (4.5a) as well as their corresponding time coefficients. The pattern correlation is -0.80 for  $E_1$  pattern included ENSO (Fig. 4.4a) and  $E_2$  pattern excluded ENSO (Fig. 4.5b), and -0.85 for  $E_2$  included ENSO (Fig. 4.4b) and  $E_1$  excluded ENSO (Fig. 4.5a). The minimum lag correlation of -0.91 between the  $C_1(t)$  included ENSO (Fig. 4.4c) and the  $C_2(t)$  excluded ENSO (Fig. 4.5d) occurs at  $C_1(t)$  included ENSO leading 2 months. A minimum correlation of -0.94 occurs simultaneously between the  $C_2(t)$  included ENSO (Fig. 4.4d) and  $C_1(t)$  excluded ENSO (Fig. 4.5c). Therefore, the ENSO pattern can be considered as a regular mode of climate variations.

Another regular mode is  $E_2$  included ENSO (Fig. 4.4b) or  $E_1$  excluded ENSO (Fig. 4.5a). This mode is dominant during non-ENSO period, and exhibits phase difference with either anti-ENSO or mid-ENSO. Occurrence of ENSO events also can be regarded as a result of the alternation of the bimodal climate system (Lau, 1986). This also supports the previous statement of two steady states, i.e., non-ENSO and ENSO. However, the question of how the transition between those two steady states occurs still remains unknown.

An interesting difference between Figs. 4.4a and 4.5b is that changes over the Indian, Asia, and Australia monsoon regions are out of phase with those over the central-eastern Pacific in Fig. 4.4a, but they are in phase in Fig. 4.5b. This may be indicative of an association between monsoon variations and ENSO events (Barnett, 1983).

#### 4.2.2. Seasonal Variation

As mentioned earlier, the component  $OLR''(S)$  has a time scale between a season and slightly less than one year. Since the five years (1979-1983) normal annual cycle (same for each year) has been removed from the data set,  $OLR''(S)$  represents year-to-year anomalous seasonality, namely, interannual variations with a seasonal time scale.

The first two EOF modes of  $OLR''(S)$  are shown in Fig. 4.6. Over the equatorial Indian Ocean and Pacific, there exists approximately a quarter phase difference between  $E_1$

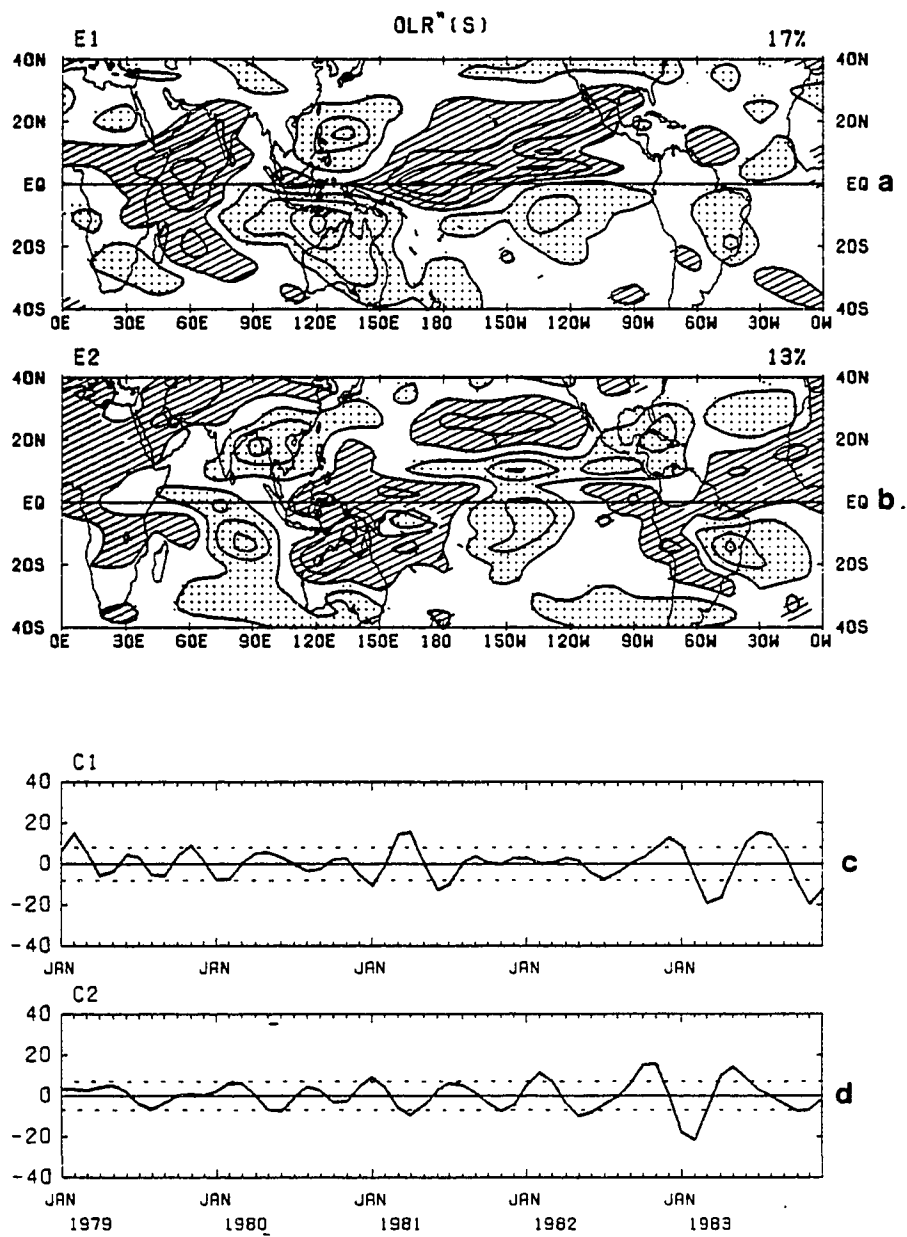


Fig. 4.6 As in Fig. 4.4, except for OLR" (S).

and  $E_2$  patterns (Figs. 4.6a and 4.6b). On the other hand, the time coefficients  $C_1(t)$  and  $C_2(t)$  are nearly out of phase for the first three years (1979-1981). Furthermore,  $C_1(t)$  and  $C_2(t)$  show a minimum correlation of -0.53 at lag zero for the period of 1979-1981, and a maximum correlation of 0.93 occurring at  $C_2(t)$  leading  $C_1(t)$  by two months during the period of 1982-1983. Hence just prior to the onset of the 1982/83 ENSO,  $OLR''(S)$  along the equator appears to propagate systematically eastward. However, this component does not contribute significantly to the ENSO mature phase or mid-ENSO state. Presumably, this eastward propagation of the seasonal component  $OLR''(S)$  can be relevant to the onset and withdrawal of ENSO or to the transition from non-ENSO steady state to ENSO steady state and vice versa.

#### 4.2.3. A Discussion

Fig. 4.7 is the time-longitude section of  $OLR''(I)$ ,  $OLR''(S)$ , and  $OLR''$  along the equator. Clearly,  $OLR''(I)$  resembles the long time-scale features of  $OLR''$ , and  $OLR''(S)$  depicts the short time-scale characters of  $OLR''$ . A very well-organized eastward propagation of convection, which corresponds to the 1982/83 ENSO event, starts over the eastern Indian Ocean-maritime continent in the fall of 1981 and ends over the eastern Pacific in the summer of 1983 (Fig. 4.7a). The phase speed is about 8-9 degrees of

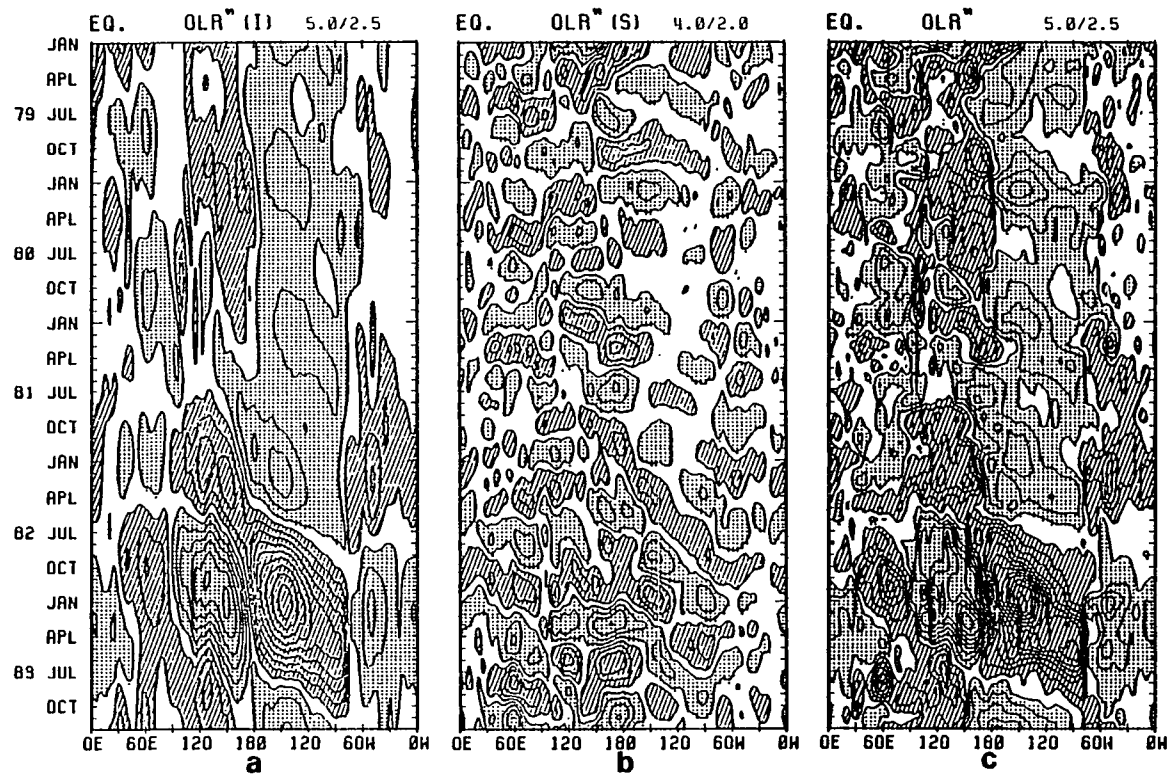


Fig. 4.7 Time-longitude section of  $OLR^{(I)}$  in (a),  $OLR^{(S)}$  in (b), and  $OLR''$  in (c) along the equator. Intervals are  $5.0 \text{ Wm}^{-2}$  for (a) and (c),  $4.0 \text{ Wm}^{-2}$  for (b). Mesh (hatching) indicates larger (less) than 2.5 ( $-2.5$ ) for (a) and (c), 2.0 ( $-2.0$ ) for (b); no zero line.

longitudes per month (0.3-0.4 m/s). In addition, a weaker than normal convection center located near 150°W in Feb. 1982 can be traced back to the Indian Ocean in the winter of 1980. This feature is more distinct in Fig. 4.7c than in Fig. 4.7a, which means that there are considerable contributions from modified seasonal component OLR"(S). As long as the main convection center moves to the central-eastern Pacific, a dry area is intensified over the maritime continent during the 1982/83 ENSO episode (Fig. 4.7a), reflecting an eastward shift of normally persistent warm water across the Pacific. This below normal convection then propagates eastward to replace the anomalous enhanced convection during the ENSO decay period.

In conjunction with the eastward movements, one can easily see that a reverse anomalous Walker circulation with updraft over the central Pacific and downdraft over the maritime continent is drastically amplified during the 1982/83 ENSO. Prior to this, a much more intensified normal Walker circulation occurred during the 1981-82 winter. Moreover, another enhanced normal Walker cell is established during 1983 winter. This is consistent with the two dipoles depicted in Fig. 4.4a. By a further examination of Fig. 4.7a or Fig. 4.7c, one notes that before and during the pre-ENSO state of January 1982 the seasonality is apparently involved in interannual variations, although the normal annual cycle is removed. In

other words, a seasonal oscillation with two steady states in summer and winter is superimposed on the non-ENSO state. This reconfirms the existence of multiple time-scale steady states.

In order to check the possibility that the seasonality discussed here is forced by the 1982/83 ENSO event in terms of the normal seasonal component removal procedure, the normal annual cycle is recomputed with only three years (1979-1981) of OLR data, and then it is removed from the entire five-year data set. This new data set is subjected to all the analysis steps previously done for  $OLR''(I)$ . The results are identical to those presented in Figs. 4.5 and 4.7a. Therefore, the interannual variability and its association with seasonality are real climate signals rather than artificial products of a numerical analysis scheme.

Shown in Fig. 4.7b is the time-longitude section of  $OLR''(S)$  along the equator. The features presented in Fig. 4.6 are clearly illustrated in this diagram, namely, many occasions of the systematic eastward propagation  $OLR''(S)$  which are well organized from the Indian Ocean to the eastern Pacific prior to and during the ENSO episode. The same analysis that was utilized for  $OLR''(I)$  above is also applied to the  $OLR''(S)$  component. The results are consistent with those discussed in Figs. 4.6 and 4.7b.

### 4.3. Intraseasonal Convective Activity

#### 4.3.1. Interannual Component

Shown in Fig. 4.8 are the first two EOF modes of  $OLR_S''(I)$ .  $E_1$  pattern (Fig. 4.8a) explains 42% of the total variance of  $OLR_S''(I)$ . Comparing Figs. 4.8a (4.8c) for  $OLR_S''(I)$  and 4.4a (4.4c) for  $OLR''(I)$ , a similarity (inversion) is immediately apparent. The pattern correlation between  $E_1$  of  $OLR''(I)$  and  $E_1$  of  $OLR_S''(I)$  is 0.91, and the correlation between  $C_1(t)$  of  $OLR''(I)$  and  $C_1(t)$  of  $OLR_S''(I)$  reaches a minimum of -0.95 at lag zero, meaning that there is greatly enhanced (much depressed) 2-15 day convective activity over deep (free) convection areas on the interannual time scale. However, a close inspection of convective activity reveals that a negative (positive) center at  $130^\circ W$ , equator ( $170^\circ E$  and north of the equator) in Fig. 4.8a for  $OLR_S''(I)$  is about 20 degrees east of the corresponding center in Fig. 4.4a for  $OLR''(I)$ . This implies a phase difference in the evolution of  $OLR''(I)$  and  $OLR_S''(I)$ . An examination of the  $E_2$  patterns and  $C_2(t)$  series of both  $OLR''(I)$  and  $OLR_S''(I)$  may clarify this point to some extent. From the beginning of 1979 to the summer of 1981, there is no obvious relationship between  $C_2(t)$  of  $OLR''(I)$  in Fig. 4.4d and  $C_2(t)$  of  $OLR_S''(I)$  in Fig. 4.8d. However, a two-month phase leading of  $C_2(t)$  of  $OLR_S''(I)$  to that of  $OLR''(I)$  is very clear between the period of fall 1981 and the end

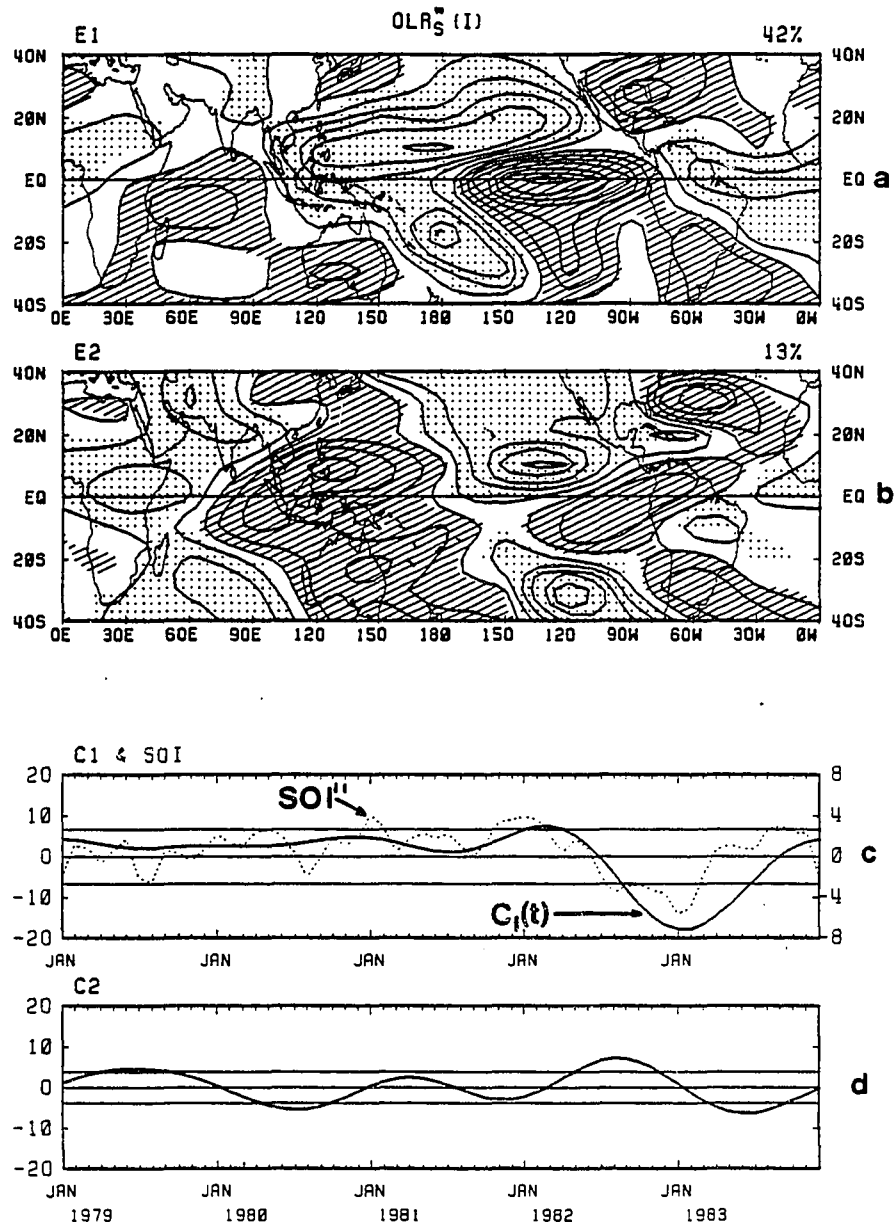


Fig. 4.8 As in Fig. 4.4, except for  $OLR_S''(I)$ .

of 1983. Moreover, a nearly quarter phase difference between  $E_1$  ( $C_1(t)$ ) and  $E_2$  ( $C_2(t)$ ) after the summer of 1981 in Fig. 4.8 describes a migration of  $OLR_S''(I)$  pattern from the maritime continent to the eastern Pacific. Hence, the eastward propagation of consolidated pattern for the first two EOFs ( $C_1(t)E_1 + C_2(t)E_2$ ) of  $OLR_S''(I)$  starts about two months earlier than that of  $OLR''(I)$  during the evolution of the 1982/83 ENSO. An interesting observation in Fig. 4.8d is the quasi-periodicity of 16-22 months, suggesting that a portion of interannual amplitude modulation of 2-15 day perturbations is an oscillating signal, and can be phase locked to ENSO events.

Unlike the  $OLR_S''(I)$  components, the EOFs of 30-60 day activity on an interannual time scale ( $OLR_L''(I)$ ) present different features. The  $E_1$  pattern (Fig. 4.9a) shows the strongest positive center over the Indian Ocean and the strongest negative center to west of Darwin, Australia. The signals over the Pacific, although slightly weaker, correspond to the 1982/83 ENSO phenomenon. The pattern correlation between  $E_1$  of  $OLR''(I)$  in Fig. 4.4a and  $E_1$  of  $OLR_L''(I)$  in Fig. 4.9a is 0.74, and the lag correlation between corresponding  $C_1(t)$ s reaches a minimum of -0.89 at lag zero, reflecting the association of large 30-60 day signals with the 1982/83 ENSO over the central Pacific. Besides the ENSO feature, a dipole pattern of the 30-60 day oscillation is also evident over the eastern Indian Ocean

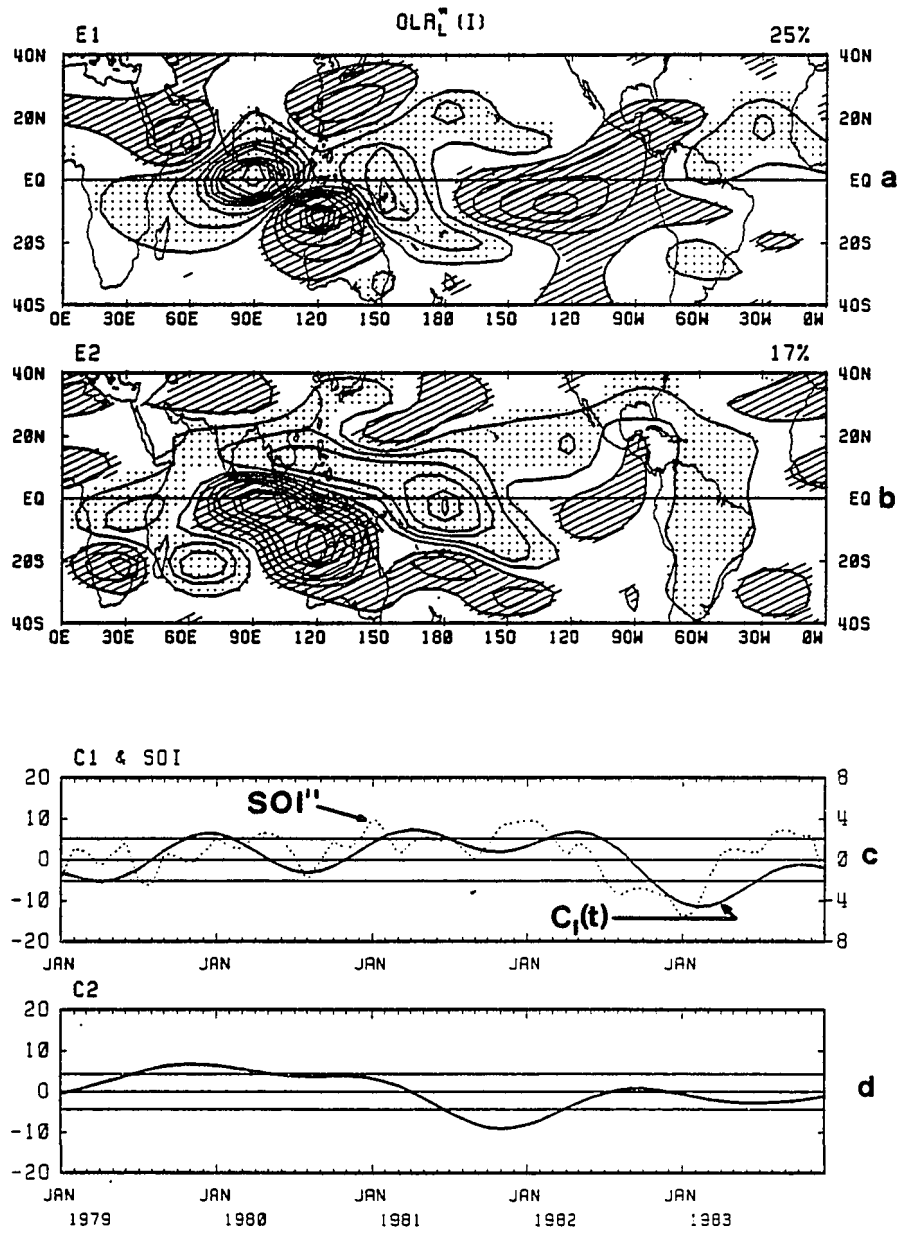


Fig. 4.9 As in Fig. 4.4, except for  $OLR_L''(I)$ .

and western Pacific (Fig. 4.9a) with the quasi-periodicity of  $C_1(t)$  in Fig. 4.9c. The interannual change of oscillation intensity is stronger over the Indian Ocean pole. A continuous stretch between two poles indicates the eastward propagation of 30-60 day oscillation. However, two negative centers over the south of Japan and west of Darwin intend to block the way of the eastward movement (Fig. 4.9a), resulting in a 30-60 day signal weakening over the maritime continent. This is in agreement with previous studies of the 30-60 day oscillation.

The  $E_2$  pattern of  $OLR_L''(I)$  does not contribute to the ENSO since the  $C_2(t)$  is nearly zero from the summer of 1982 to the end of 1983 (Figs. 4.9b and 4.9d). Prior to this, very strong negative values of  $C_2(t)$  occur during the period from fall 1981 to spring 1982, indicating much enhanced 30-60 day oscillations over the equatorial Indian Ocean and maritime continent-western Australia (negative regions of  $E_2$ ; Fig. 4.9b). Thus, part of the 30-60 day activities is possibly related to the ENSO onset. This point will be discussed in further detail in the next section.

#### 4.3.2. Seasonal Component

The EOF analysis is also applied to the components  $OLR_S''(S)$  and  $OLR_L''(S)$ , respectively. Here, the EOF patterns

are not as distinctive, even so, some aspects of the results (figures are not shown) are still of interest.

EOF analysis of  $OLR_S''(S)$  not only confirms those regions of large fluctuations as shown in Fig. 4.3a, but also indicates a period of 9-10 months for this activity. Furthermore, there appears to be a phase lock among the disturbance activities over monsoonal regions of the Indian peninsula-western Pacific, SPCZ region, and ITCZ region of northeastern Pacific.

Results for  $OLR_L''(S)$  show that activities over the two dipole centers as shown in Fig. 4.2a, i.e., the equatorial eastern Indian Ocean and western Pacific, are of opposite phase and have a time scale of 8-10 months. Recall that  $OLR_L''(S)$  component is much smaller than  $OLR_L''(I)$ , thus, the dipole structure is characterized by an out-of-phase seasonality of the amplitude modulation for the 30-60 day oscillation, and by its interannual variations as described in Fig. 4.9.

#### 4.4. An Example of Climate Predictability

The discussion of the previous subsections, provides the impetus for further investigation of disturbance activity, namely, the intraseasonal activity represented by  $OLR_L''$  and  $OLR_S''$  which tend to intensify prior to the convective enhancement associated with ENSO. This is studied by use of conventional cross spectrum analysis with the

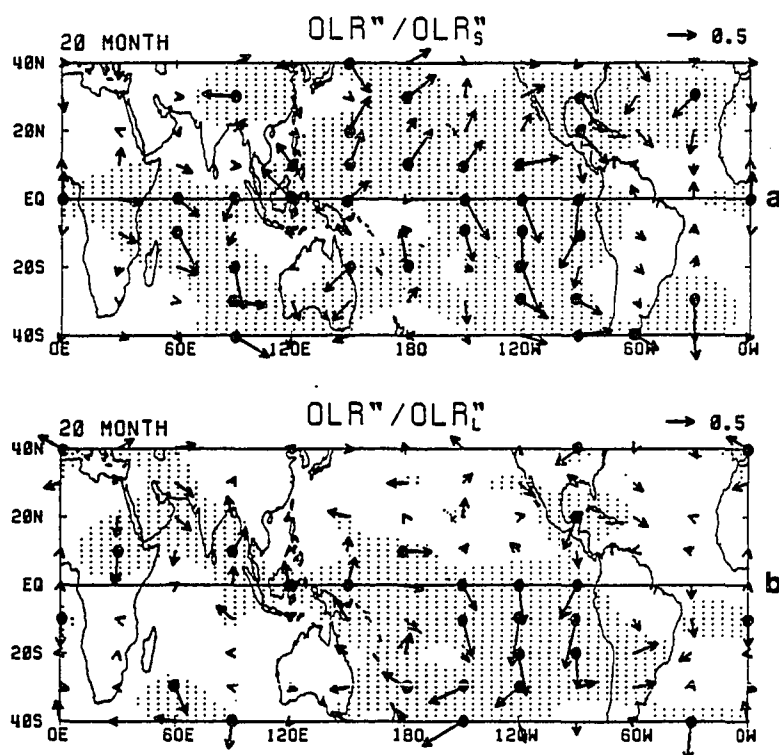


Fig. 4.10 Distributions of phase differences between  $OLR_S''$  (a) as well as  $OLR_L''$  (b) at individual grid points and  $OLR''$  at the reference point ( $5^{\circ}S, 150^{\circ}W$ ) for the spectral band centered at a period of 20 months, as computed over entire five year period. Arrows pointing to south indicate zero phase difference. Arrows are rotated in a clockwise (counterclockwise) fashion by  $1^{\circ}$  for each degree of phase lag (lead) of  $OLR_S''$  or  $OLR_L''$  relative to the reference time series of  $OLR''$ . The squared coherence values exceed the 90% and 95% significance levels are indicated by the light mesh and heavy dot.

reference time series being  $OLR''$  at  $(5^{\circ}S, 150^{\circ}W)$ , which is the convection center of the 1982/83 ENSO as revealed by Fig. 4.4a. The spectra are computed between global  $OLR_G''$  or  $OLR_L''$  and the reference  $OLR''$  for each frequency band. The coherence and phase are plotted in terms of a vector in the clockwise rotating fashion. The spectra for a 20-month period are presented in Fig. 4.10. The spectral results indicate the most significant coherence is within the range of about 15-30 months with 20 months being representative.

A definite eastward propagation can be seen in Fig. 4.10a. About one year prior to maximum convection ( $OLR''$  minimum) at reference point, enhanced  $OLR_G''$  activity occurs over the maritime continent. Subsequently, it migrates northeastward across the Pacific through the northern subtropics, and then southward to the southeastern Pacific. Surprisingly, the  $OLR_G''$  signal somehow lost its trace at the equator,  $180^{\circ}$  during the eastward movement. Over the reference point,  $OLR_G''$  is slightly leading  $OLR''$ . Presumably, the 2-15 day activity ( $OLR_G''$ ) in Fig. 4.10a, although containing many irregularities, can be regarded as a forerunner of convection associated with ENSO in a broad sense.

With respect to the reference  $OLR''$  series,  $OLR_L''$  activity also can be traced back about one year to the equatorial eastern Indian Ocean, maritime continent, and western Pacific. However, the relatively large coherence

is confined only to the equatorial region. During the eastward migration,  $OLR_L''$  likewise experiences considerable weakening at the equator near the date line, and leads  $OLR''$  over the reference point. The strongest coherence and systematic phase propagation are found over the southeastern Pacific (Fig. 4.10b).

The results presented in Fig. 4.10 are consistent with those determined by EOF analysis. That is, intraseasonal convective activity, which hypothetically act as an index of synoptic disturbances and 30-60 day perturbations, can serve as a precursor of interannual convection related to ENSO events. In other words, interannual variability of convection are detectable to a certain degree over the tropical region.

By using the method of Trenberth (1984), the analysis of the signal-to-noise ratio<sup>6</sup> (SNR) is applied to OLR data in order to identify the geographical distribution of a detectable climate signal. As previously seen, interannual variations in which the largest contribution comes from the 1982/83 ENSO are phase locked to seasonality. Hence, the SNR is calculated separately for the Northern Hemisphere summer and winter, as shown in Fig. 4.11. Madden and Shea

---

<sup>6</sup>There are certain disadvantages of this method. A more sophisticated approach is briefly discussed in Appendix (Chu and Katz, 1987).

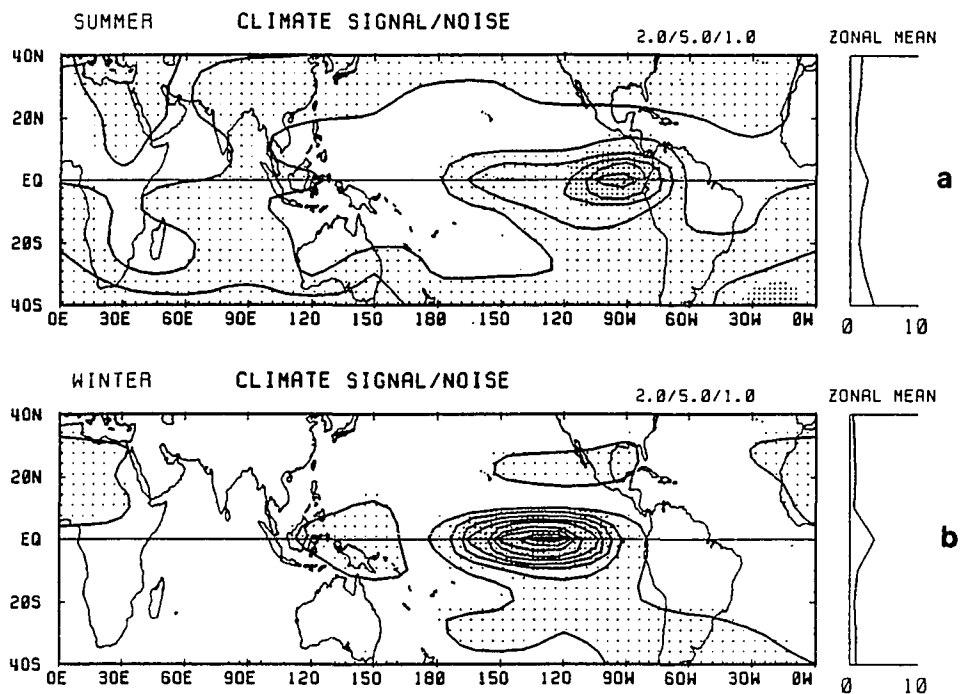


Fig. 4.11 Climate signal-to-noise ratio in summer (a) and winter (b). Intervals are 2.0, and heavy mesh denotes the region of larger than 5.0, and light mesh indicates the area of less than 5.0 and greater than 1.0. Zonal mean are also shown at the right.

(1972) used a value of  $SNR > 2$ , based on root-mean-square amplitude estimate, to represent a distinct separation between climate signal and noise (or natural variability). Since the Fourier decomposition technique is used to compute interannual (climate signal) and intraseasonal (noise) variability, and the time series used are relatively short (5 years), a ratio of larger than 5 will be the criterion indicative of a distinct separation between signal and noise. Hence, there is no potential scale interaction between them, due to the relative absence or weak amplitude of the noise in such a region. A ratio between unity and 5 indicates a region where potential scale interaction exists. Nevertheless, the detection of climate signals over a certain period, for example the 1982/83 ENSO episode, can be possible.

In summer (Fig. 4.11a), the maximum ratio is found over the equatorial eastern Pacific near the South America coast ( $>9$ ). The potential detectable region of climate signal ( $1 < SNR < 5$ ) covers the central Pacific and Indian Ocean in the tropical region. However, the SNR is closer to or less than unity over the maritime continent and western Pacific, indicating that the detection of the climate signal over these regions will be very difficult. In other words, interannual variations are totally overwhelmed by intraseasonal variability over this region.

In winter (Fig. 4.11b), the maximum ratio is located over the equatorial central-eastern Pacific ( $>18$ , double the summer maximum). Interestingly, a potential detectable region of interannual variability ( $1 < \text{SNR} < 5$ ) shifts eastward from the Indian Ocean in summer to the maritime continent and western Pacific in winter. The gap region of  $\text{SNR} < 1$ , although still existing, is much reduced over the equator,  $170^{\circ}\text{E}$  in comparison to summer. This gap ( $\text{SNR} < 1$ ) is results from a weakening of the interannual component during its eastward migration, as mentioned previously.

It is likely that the major contribution to large SNR over the equatorial central and eastern Pacific is due to the 1982/83 ENSO, because of its exceptional strength. Therefore, one implication of the above result is that the interannual variation associated with ENSO possibly has its origin over the Indian Ocean and western Pacific with a phase-lock to seasonality. Barnett (1983) has suggested that the Indian Ocean and eastern Pacific are the spawning region for ENSO, and that large-scale wind and surface pressure anomalies undergo a systematic slow eastward propagation from this region to the central-eastern Pacific on an interannual time scale. The present results and many previous works have confirmed that the 30-60 day oscillation is substantially amplified over the Indian Ocean-western Pacific, inferring potential interaction between interannual and intraseasonal variations. This is consis-

tent with the relatively low value of the SNR (Fig. 4.11) found over these regions. In general, this makes the prediction or even detection of climate signals difficult when using parameters from the Indian Ocean and western Pacific.

However, the SNR value represents the average criterion for the entire time domain (5 years). With this in mind and recalling the results of eastward propagation within ENSO cycle discussed in the EOF analysis of CLR<sup>"(I)</sup> and OLR<sup>"(S)</sup>, it is reasonable to expect that the ENSO anomaly over the equatorial central-eastern Pacific may be traced to the Indian Ocean and western Pacific regions. The traceable time duration prior to the ENSO onset is relatively short because natural climate variability (noise or transient fluctuation) overshoots the climate signal during the non-ENSO steady state, especially over the Indian Ocean and western Pacific. In other words, the enhancement of interannual variation over the Indian Ocean and western Pacific is strongly regulated by processes somehow related to persistent intraseasonal activity in this area, such as, amplitude modulation of the 30-60 day oscillation, and the modification of seasonality. Therefore, the initiation of ENSO or the transition from non-ENSO to ENSO steady state must extract energy from intraseasonal disturbance activity. This certainly suggests the importance of intraseasonal fluctuations to ENSO events,

particularly to its onset. Some of these aspects will be discussed in further detail with respect to the 1982/83 ENSO phenomenon in next section.

## 5. The 1982/83 ENSO

### 5.1. Introduction

The 1982/83 ENSO, which started in June 1982 and ended July 1983, provided the most notable and pronounced example of interannual variability. Various meteorological and oceanic aspects of the event have been documented by several researchers (e.g., Arkin et al., 1983; Gill and Rasmusson, 1983; Rasmusson and Wallace, 1983). In late June 1982, the normal easterly surface winds along the equator west of the date line were replaced by westerlies. This was accompanied by a warm water shift from the western Pacific to central Pacific, together with the onset of an extended period of extremely heavy rainfall over this anomalous warmed (high SST) region. This warm water shift reversed the normal Walker circulation, resulting in the commencement of severe drought over the maritime continent and South Asia. Concurrently, changes also occur in the upper troposphere, namely, the establishment of the teleconnection pattern described by Horel and Wallace (1981) which is characterized by a pair of anticyclonic gyres (anomaly) over the subtropics of the central Pacific with enhanced easterly between them and westerly jets poleward.

The association between tropical heating and extra-tropical westerly anomalies on the interannual time scale,

especially in connection with ENSO, was first suggested by Bjerknes (1966). During the 1982/83 ENSO, a strong easterly jet stream over the equatorial central-eastern Pacific was established through an intensification of the local Hadley circulation (anomaly) which developed in response to an increase in latent heat release over there (Ardanuy and Krishnamurti, 1987), indicating an enhanced teleconnection between equatorial heating and mid-latitude circulation. This strong tropical-extratropical interaction occurring in a deep equatorial upper-level easterly flow invalidates some of the previous theoretical explanation of the teleconnection (e.g., Hoskins and Karoly, 1981; Lau and Lim, 1984). However, Sardeshmukh and Hoskins (1987) recently showed that the vorticity advection due to the irrotational component of the winds, which represents a direct N-S vertical overturning, is primarily responsible for the westerly acceleration of the midlatitude jet stream. Therefore during ENSO events, the local Hadley circulation should be an essential factor for global weather changes.

In this section, an attempt will be made to detail the vertical structure of interannual time scale-wind perturbations and associated short-period transient (intraseasonal) disturbances over the eastern North and South Pacific before, during, and after the 1982/83 ENSO, i.e., pre-ENSO, mid-ENSO, and post-ENSO states. Since the evolution of

climate anomalies over the maritime continent and Brazil is the complete reversal of that over the eastern equatorial Pacific (cf. Fig. 4.4), it is reasonable to expect that the relationship between interannual modes (including locally enhanced anomalous N-S overturning) and transient disturbance activity differs significantly from one region to another. This possibility will also be examined in the following discussion.

## 5.2. Interannual Zonal Wind

Shown in Fig. 5.1 are the time evolution of original and anomalous zonal wind along the equator at 200 mb and 850 mb. Recall the major feature in Fig. 4.7c, that is, a distinct zone of large negative OLR" (above normal convection) originated over the eastern Indian Ocean around July 1981, propagated eastward through the western and central Pacific, eventually reaching the eastern Pacific near 90°W around July 1983. A comparison of Fig. 4.7c with Figs. 5.1b and 20d reveals a close association of above normal convection ( $OLR'' > 0$ ) with anomalous low-level westerlies ( $u'' > 0$ ) which are capped by anomalous easterlies ( $u'' < 0$ ) aloft. Conversely, regions of below normal convection ( $OLR'' < 0$ ) are characterized by low-level easterlies ( $u'' < 0$ ) and upper-level westerlies ( $u'' > 0$ ). This is best exemplified during the mid-ENSO phase around January 1983 [abbreviated as JAN(0)] where the western Pacific exhibits

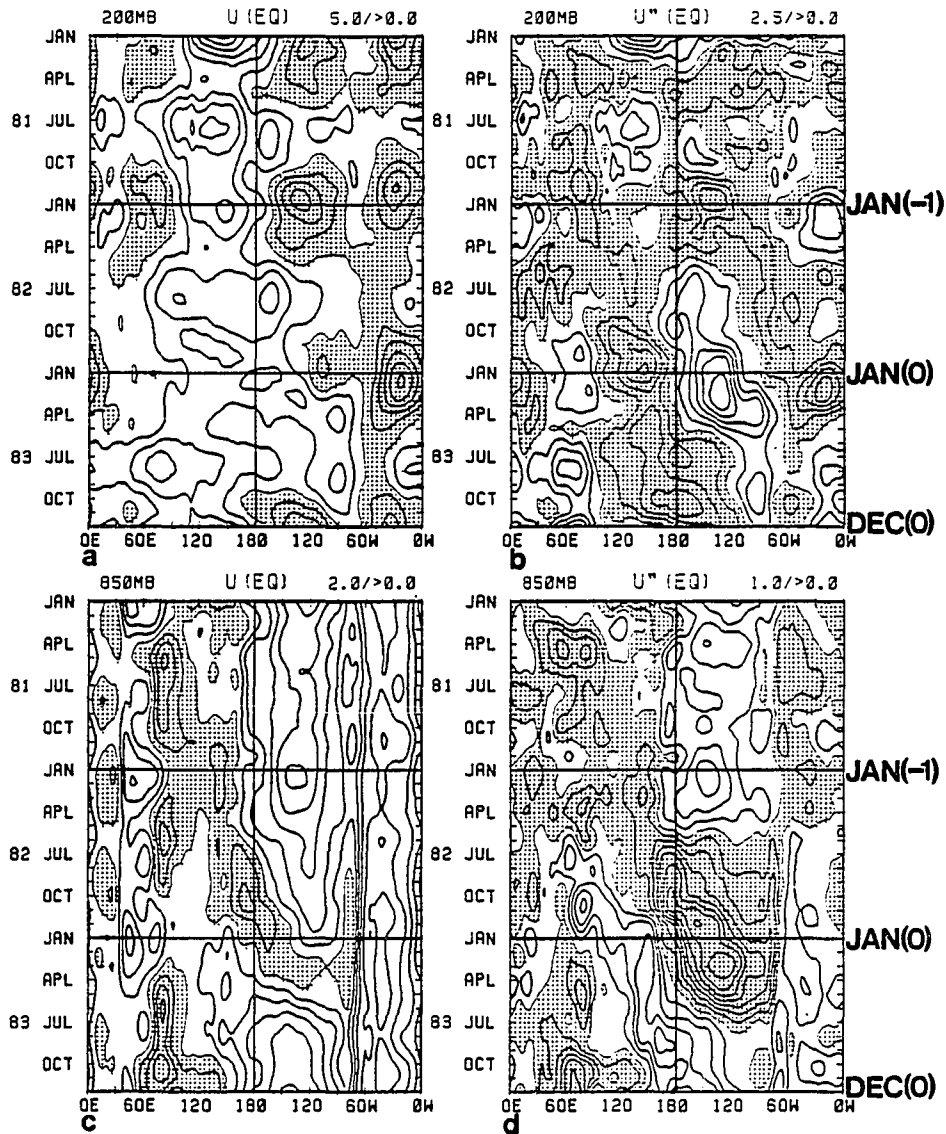


Fig. 5.1 Left: Longitude-time sections of 3-month running mean  $u$  at 200 mb (a; interval  $5 \text{ ms}^{-1}$ ) and 850 mb (c; interval  $2 \text{ ms}^{-1}$ ) along the equator. Shading indicates regions of westerly  $u$ . Right: As in left, except for anomaly  $u''$  at 200 mb (b; interval  $2.5 \text{ ms}^{-1}$ ) and 850 mb (d; interval  $1 \text{ ms}^{-1}$ ). Shading denotes regions of westerly anomaly ( $u'' > 0$ ).

an association of  $OLR'' > 0$  with  $850 \text{ mb } u'' < 0$  and  $200 \text{ mb } u'' > 0$ , while the eastern Pacific indicates the coincidence of  $OLR'' < 0$  with  $850 \text{ mb } u'' > 0$  and  $200 \text{ mb } u'' < 0$ . An alternation of the relationships between these two regions can be clearly seen during the pre-ENSO phase of January 1982 [denoted as JAN(-1)], and post-ENSO phase of December 1983 [signified as DEC(0)]. Namely, the interannual  $u''$  perturbations are out of phase (baroclinic nature) in the vertical at the equator. In this regard, equatorial interannual  $u''$  modes resemble the intraseasonal 30-60 day  $\bar{u}$  modes which are also baroclinic in the vertical (Madden and Julian, 1972; Murakami, 1987 and 1988; and others).

There is a tendency for equatorial  $u''$  modes to propagate eastward. As mentioned earlier, in JAN(0) pronounced westerly  $u''$  anomalies dominated the lower troposphere of the eastern Pacific between about the date line and  $80^{\circ}\text{W}$ . The trajectory of this anomalous westerly zone is traceable during the precursor stages of the 1982/83 ENSO event. In Fig. 5.1d, a well-organized westerly (anomaly) zone is established near the east coast of Africa ( $40^{\circ}\text{E}$ ) in April 1981, about fifteen months prior to the onset of the 1982/83 ENSO. Regions of anomalous westerlies then shift eastward across the Indian Ocean and western Pacific, followed by a dramatic intensification after reaching the date line around July 1982 (the onset phase). Thus, the birthplace of  $850 \text{ mb } u''$  perturbations appears to be the

western Indian Ocean or possibly further upstream on the Africa coast. The above statement is based on the 3-months running mean  $u''$  anomalies along the equator. This can also be tested against the time series of the original 3-months running mean data (Fig. 5.1c) in which the normal seasonal cycle is included. It appears that the initial development of  $u''$  westerlies near the western African coast is accomplished by a phase locking with the annual cycle of low-level winds; namely, anomalous acceleration of westerlies in April 1981.

Several studies of westerly burst, cited previously, emphasized that atmospheric transients over the western Pacific can directly trigger interannual ocean-atmosphere coupled modes (ENSO). In other words, these transients can be fully coupled with the ocean, and produce interannual SST variations. However in Fig. 5.1d, evidence has been presented that the origin of anomalous  $u''$  westerlies dates back more than one year prior to the onset of the 1982/83 ENSO. Plus, their breeding place is further upstream in the eastern Africa-Indian Ocean rather than the western Pacific. The western Pacific is only the region for significant intensification of the interannual westerlies, instead of its origin. This enhancement of the  $u''$  westerlies can be attributed to several mechanisms, e.g., mid-latitude influence (Harrison, 1984), and nonlinear interaction (Murakami and sumathipala, 1988).

Based on an ocean model, Gill and Rasmusson (1983) successfully simulated the principle features of the ocean response due to interannual zonal wind forcing for the 1982/83 event. They suggested that a scenario of anomalous zonal advection, which was responsible for the 1972/73 ENSO, was also applicable to the 1982/83 event. A closer inspection Figs. 4.7c and 5.1d, reveals that during the summer and winter of 1981 weak  $u''$  westerlies (about  $1 \text{ ms}^{-1}$ ) correspond to below normal convection ( $OLR'' > 0$ ) over the eastern Indian Ocean and maritime continent. This discrepancy is likely due to the overwhelmingly persistent strong intraseasonal (especially 30-60 day) convective activity over this region as discussed earlier, and may also result in more freedom of intraseasonal wind anomalies as westerly bursts. Above phenomenon can arise the delusion for one to consider transient westerly as an initiator of interannual mode (ENSO). However, this is also suggestive of the importance of intraseasonal activity to interannual modes of zonal wind anomalies.

Based on an ocean-atmosphere coupled model, Lau and Shen (1987) also emphasized the importance of zonal advection of sea surface temperature (SST) as a determining factor in the development of unstable interannual modes. Murakami (1988) found that observed highest SST'' anomalies occur slightly ahead of the eastward propagating OLR'' perturbations, which is essentially identical to the model

results. Atmospheric intraseasonal disturbances have their own dynamics in this coupled model. The unstable modes may be considered as intrinsic modes enhanced through mutual interactions between the atmosphere and ocean with the interannual time scale. It is possible that intraseasonal activity (e.g.,  $OLR_G''$  and  $OLR_L''$  in this paper) benefit the growth of atmospheric interannual modes internally, and then favor coupling with the ocean efficiently on the interannual time scale.

### 5.3. Intraseasonal Activity

As seen in the previous section, the space and time scale of transient activity  $OLR_L''$  and  $OLR_G''$  become much larger than those of individual  $\tilde{OLR}$  and  $OLR^*$  perturbations. These transient disturbances, as a group, correlate (interact) well with the global-scale interannual  $OLR''$  modes.

#### 5.3.1. The 30-60 Day Disturbance

Figure 5.2 depicts the time series of  $OLR_L''$  along the equator from  $60^\circ\text{E}$  to  $60^\circ\text{W}$ . Over the eastern Pacific ( $120^\circ\text{W}$ - $90^\circ\text{W}$ ), 30-60 day activity is much more intensified during the 1982/83 ENSO episode. The enhanced signal can be traced upstream at least to the date line, which confirms the previous finding. Over the Indian Ocean ( $60^\circ\text{E}$ - $90^\circ\text{E}$ ) and the western Pacific ( $120^\circ\text{E}$ - $150^\circ\text{E}$ ), an out

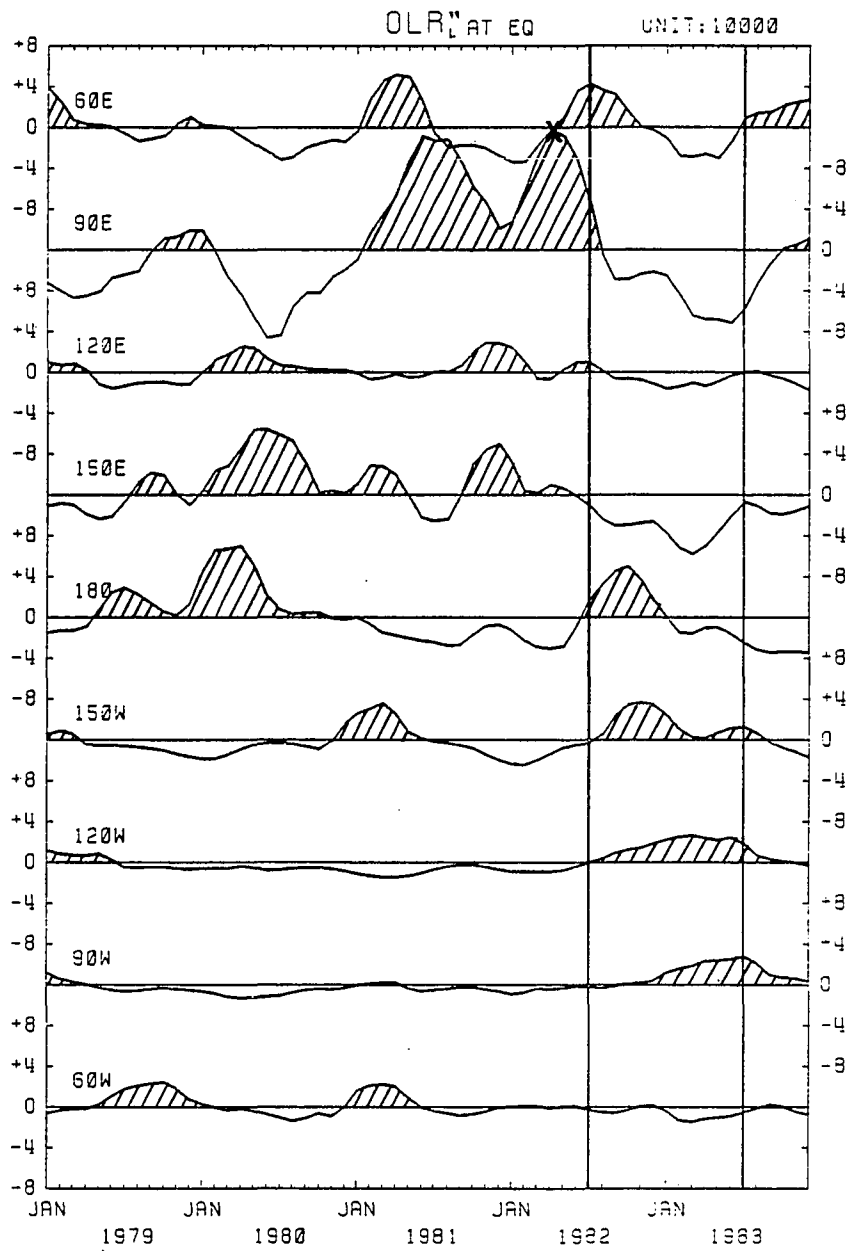


Fig. 5.2 Time series of 30-60 day convective activity  $OLR_L''$  (unit:  $10^4 \text{ W}^2\text{m}^{-4}\text{day}$ ) at the equator for every 30 degrees of longitude from  $60^\circ\text{E}$  to  $60^\circ\text{W}$ . Shading indicates regions of above normal activity. See text for further information.

of phase relationship generally holds, except during the ENSO period when both are depressed. This means that the east-west orientated dipole structure of the 30-60 day oscillation exists not only in phase but also in intensity, with the weak pole in the western Pacific. Interestingly, the anomalously strong 30-60 day  $OLR_L''$  convection activity in the eastern Indian Ocean ( $90^\circ E$ ) occurs prior to the ENSO onset. The two strongest positive  $OLR_L''$  peaks are, June-August 1981 and April-May 1982, respectively. The latter is just ahead of the onset phase, its detailed structure will be further investigated next.

The daily time series of  $OLR'$  (refer to eq. 2) which has been used to compute  $OLR_L''$  are shown in Fig. 5.3a from Jan. 1982 to Feb. 1983, and the 30-60 day filtered  $OLR$  and high-pass filtered  $OLR^*$  (period < 15 days) are presented in Fig. 5.3b and 5.3c, respectively. Clearly, the 30-60 day oscillation (Fig. 5.3b) is greatly enhanced over the period of March-June 1982, in terms of an amplitude modulation process. This signal is also evident in  $OLR'$  data (Fig. 5.3a). The strongest 30-60 day cycle starts in early May and ends in late June 1982 (Fig. 5.3b). From an EOF analysis of the 30-60 day filtered  $OLR$  data for the same five-year period, the first eigenmode ( $E_1$ ) and its time evolution ( $C_1(t)$ ) are shown in Fig. 5.4 (Shrestha, 1986). The spatial pattern (Fig. 5.4a) depicts the dipole feature, as expected. The strongest cycle in  $C_1(t)$  is the only one

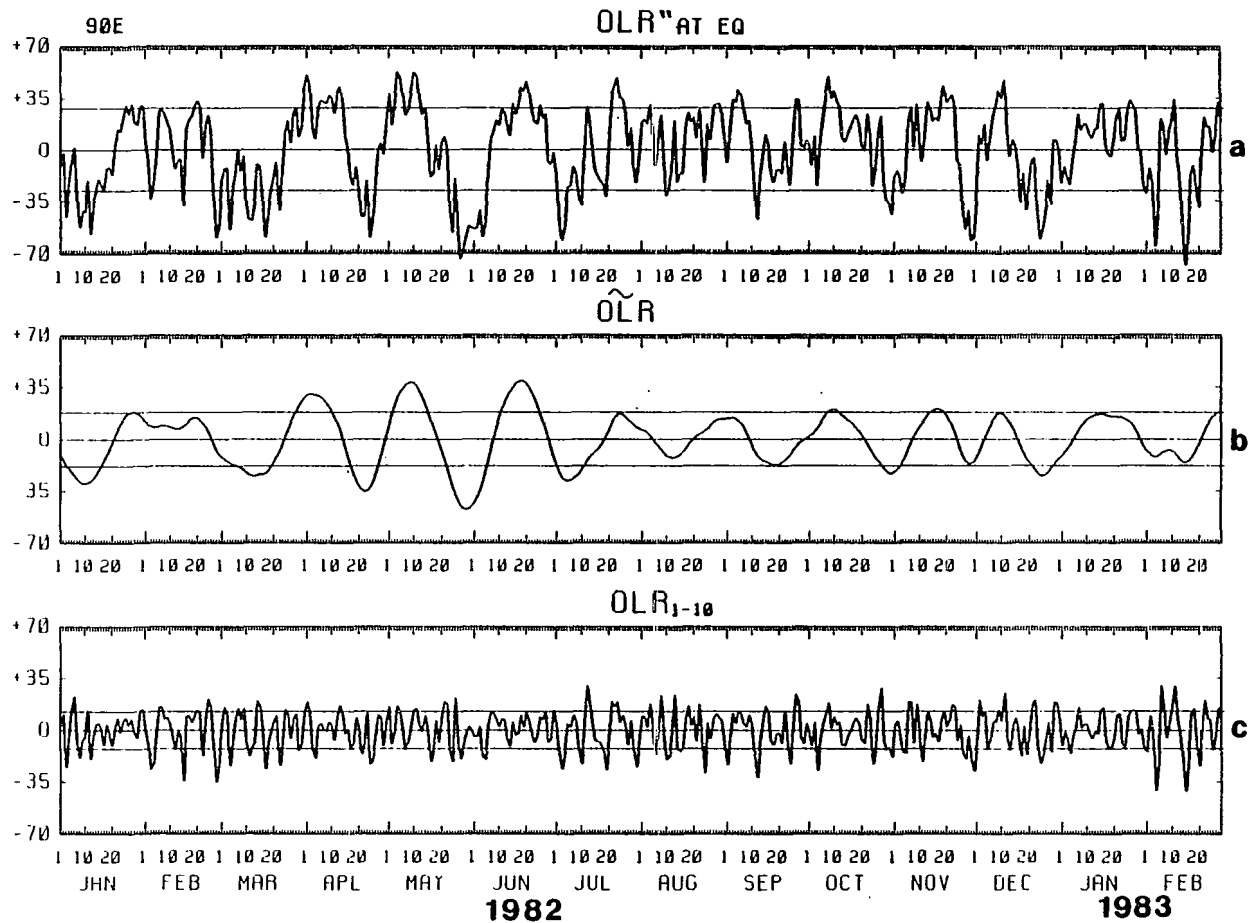


Fig. 5.3 Time series of daily OLR' (a),  $\bar{\text{OLR}}$  (b), and OLR\* (c) at (Equator,  $90^{\circ}\text{E}$ ) from 1 Jan. 1982 to 28 Feb. 1983, unit of  $\text{Wm}^{-2}$ . Refer to Section 2 for detail.

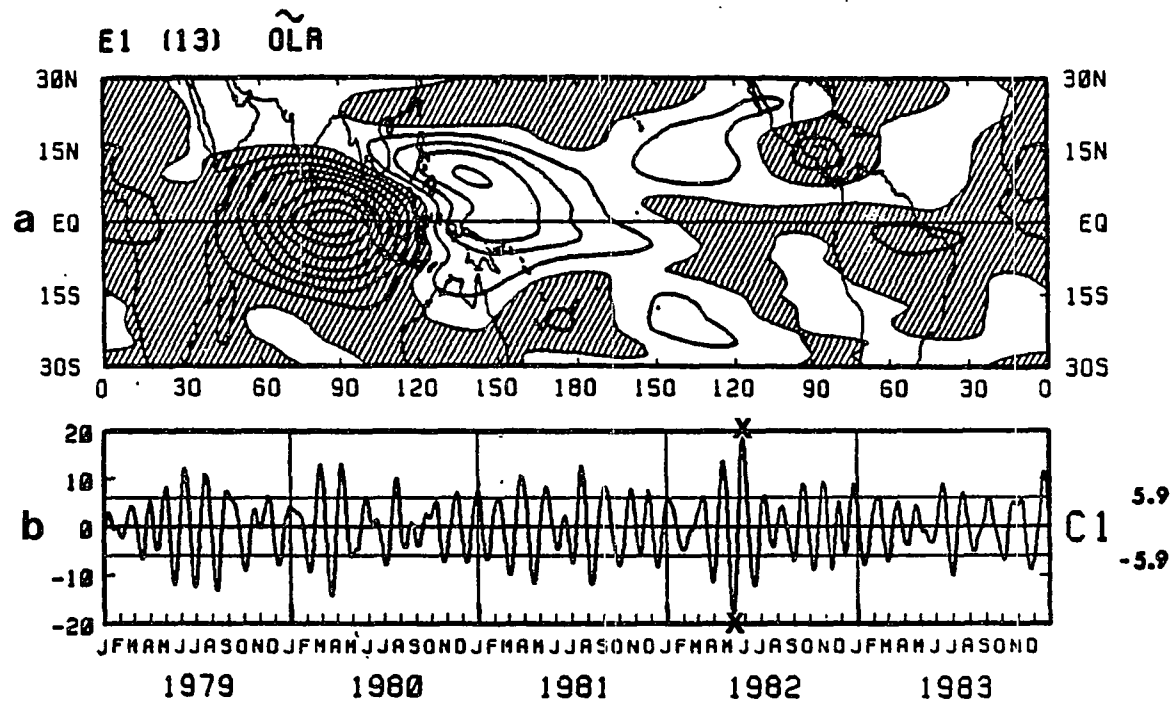


Fig. 5.4 The first EOF pattern (a) of the 30-60 day filtered  $\tilde{O}LR$ . Intervals are 0.05 (non-dimensional), and the shading denotes less than -0.025, and zero line is omitted. The frictional variance is shown in the bracket. Shown in (b) is the time coefficient  $C_1(t)$ . The standard deviation of  $C_1(t)$  is also shown in (b). The largest amplitude of  $C_1(t)$  is marked by a letter x (Adopted from Shrestha, 1986).

whose amplitude exceeds three times the standard deviation, and it occurs during May-June 1982 (Fig. 5.4b), which is entirely consistent with the findings in Fig. 5.3b. In fact, an examination of another  $C_1(t)$  from an EOF analysis for 10 years (1975-77, 1979-85) of 30-60 day filtered OLR (figures are not shown) reveals that the cycle during May-June 1982 is also the strongest one. Thus, the above results not only are a regional phenomenon in a short-time period, but also exhibits global perspectives over a longer time period. The fact that the strongest 30-60 day oscillation within ten years occurs prior to the onset of the 1982/83 ENSO (the strongest one in the record) suggests the existence of an intrinsic link between them, reflecting the importance of the 30-60 day oscillation to the ENSO onset.

In order to further clarify the above discussion, a series of daily OLR' maps are shown in Fig. 5.5 from the first of May to the first of November 1982 with an average interval of about 10 days. Since the 30-60 day oscillation effecting the ENSO onset involves the interaction of their time scales, a seven-day running mean, instead of the 30-60 day filtering, is applied to OLR' data in order to retain the interannual variations and reduce synoptic noise. The daily OLR' maps depicted in Figure 5.5 are selected with reference to the phase of the 30-60 day oscillation shown in Fig. 5.3b. Three isolated spots of negative OLR' (above

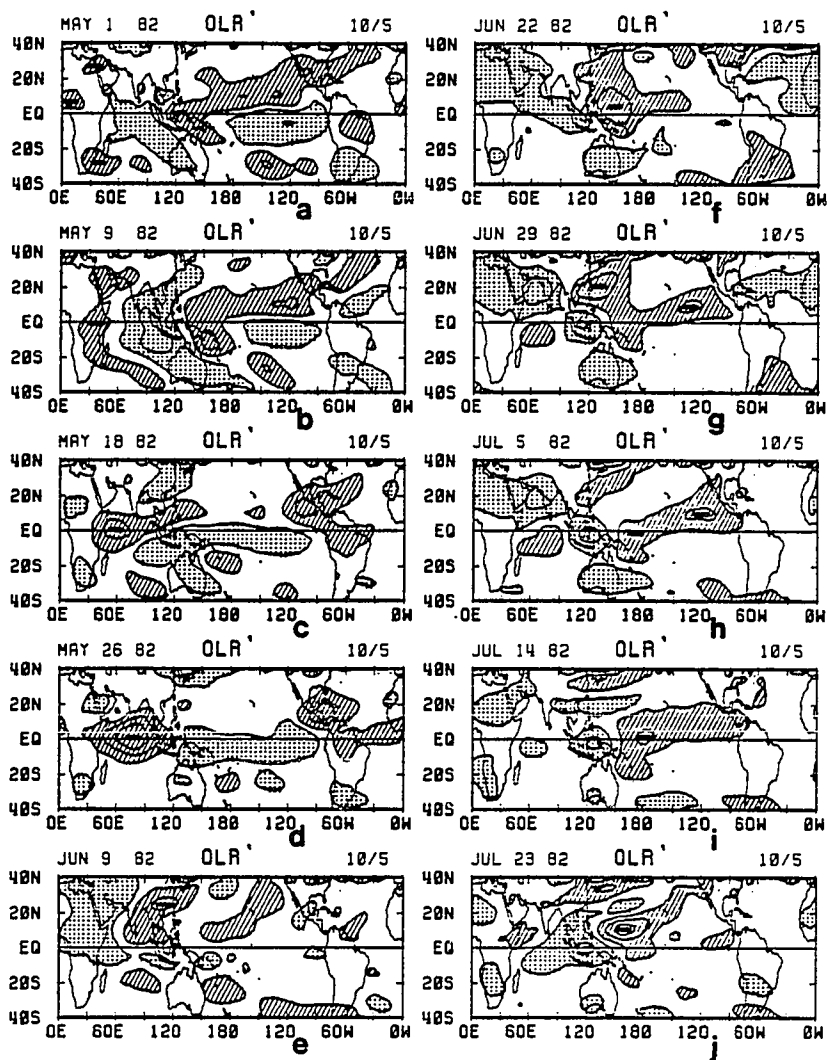


Fig. 5.5 Seven-day running mean of  $OLR'$  (unit:  $Wm^{-2}$ ) at the selected days from May 1st to Nov. 1st 1982. Intervals are 10.0 units and mesh (hatching) denotes the greater (less) than +5.0 (-5.0) units; no zero lines. The major convection centers are marked by minus sign '-'.

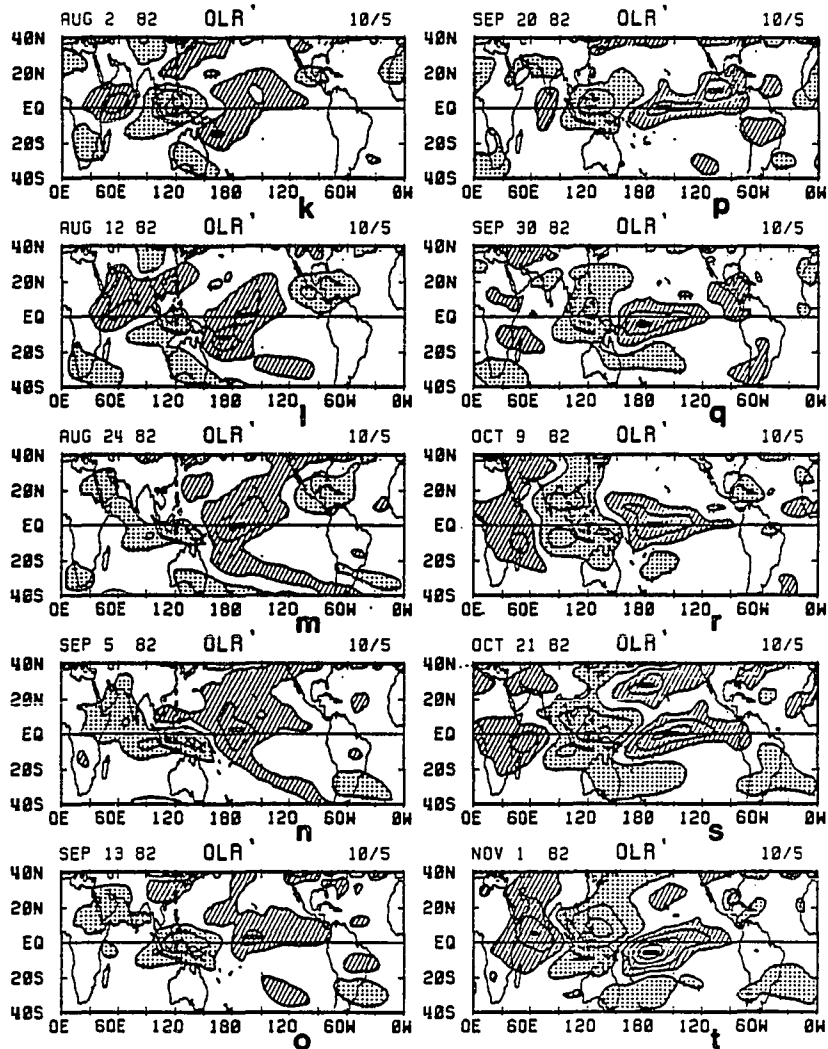


Fig. 5.5 (continue)

normal convection) over the Red Sea, west coast of central Africa, and south of Madagascar in Fig. 5.5a are united along the east coast of Africa about one week later (Fig. 5.5b). Then, this negative OLR' region propagates eastward into the Indian Ocean (Fig. 5.5c), and significantly intensifies as it approaches the Indian Ocean region (Fig. 5.5d). Over the Asiatic monsoon region, a northward propagation of negative OLR' anomaly is very well defined (Figs. 5.5e-5.5g). When this anomalously intensified 30-60 day convection center reaches the western Pacific (Figs. 5.5f and 5.5g), a positive OLR' area is established near the maritime continent and stalls thereafter. This indicates a directional shift of the anomalous Walker circulation as well as the onset of the 1982/83 ENSO event. Subsequently, anomalous convection ( $OLR' < 0$ ) in the western and central Pacific migrates slowly eastward, and gradually intensifies and expands. It is quite different from the normal situation of the 30-60 day oscillation approaching the western Pacific (e.g., Figs. 5.5a, 5.5b, and 5.5c). In general, low-frequency convection after passing through the maritime continent emanates from the equatorial region into the Inter-Tropical Convergence Zone (ITCZ) and the South Pacific Convergence Zone (SPCZ) and then dies out, whereas the equatorial central-eastern Pacific is still a cold water region and prevents deep convection. However, the occurrence of convection over the western Pacific in

association with the strongest 30-60 day oscillation marks the beginning of eastward shift of the warm pool (1982/83 ENSO onset). Consequently, a replacement of fair skies over the central and eastern Pacific by the deep convection and heavy rainfall takes place, indicating the transition from non-ENSO steady state to the 1982/83 ENSO state (Figs. 5.5g-5.5t) with an enhancement of the reverse Walker circulation (anomaly) and N-S vertical overturning. From the above observational evidence, it is possible to conclude that the 30-60 day oscillation is in rapport with the ENSO onset and can be a trigger of ENSO. These results essentially support the hypothesis proposed by Lau (1986). Interestingly, similar observational evidence during the recent 1986/87 ENSO episode has been presented by Nitta and Motoki (1987).

#### 5.3.2. The 2-15 Day Disturbance

Figure 5.6 depicts the time series of short-period  $OLR_S''$  activity along the equator from  $60^\circ E$  to  $60^\circ W$ . Prior to the 1982/83 ENSO,  $OLR_S''$  disturbance activity is below normal over the eastern Pacific between  $150^\circ W$  and  $90^\circ W$ . This is contrasted with a sharp increase in  $OLR_S''$  during the onset phase. At  $150^\circ W$ ,  $OLR_S''$  reaches a peak in December, 1982; while at  $90^\circ W$ ,  $OLR_S''$  becomes maximum in April, 1983. This is indicative of the eastward propagation of  $OLR_S''$  activity with nearly the same phase speed as that of

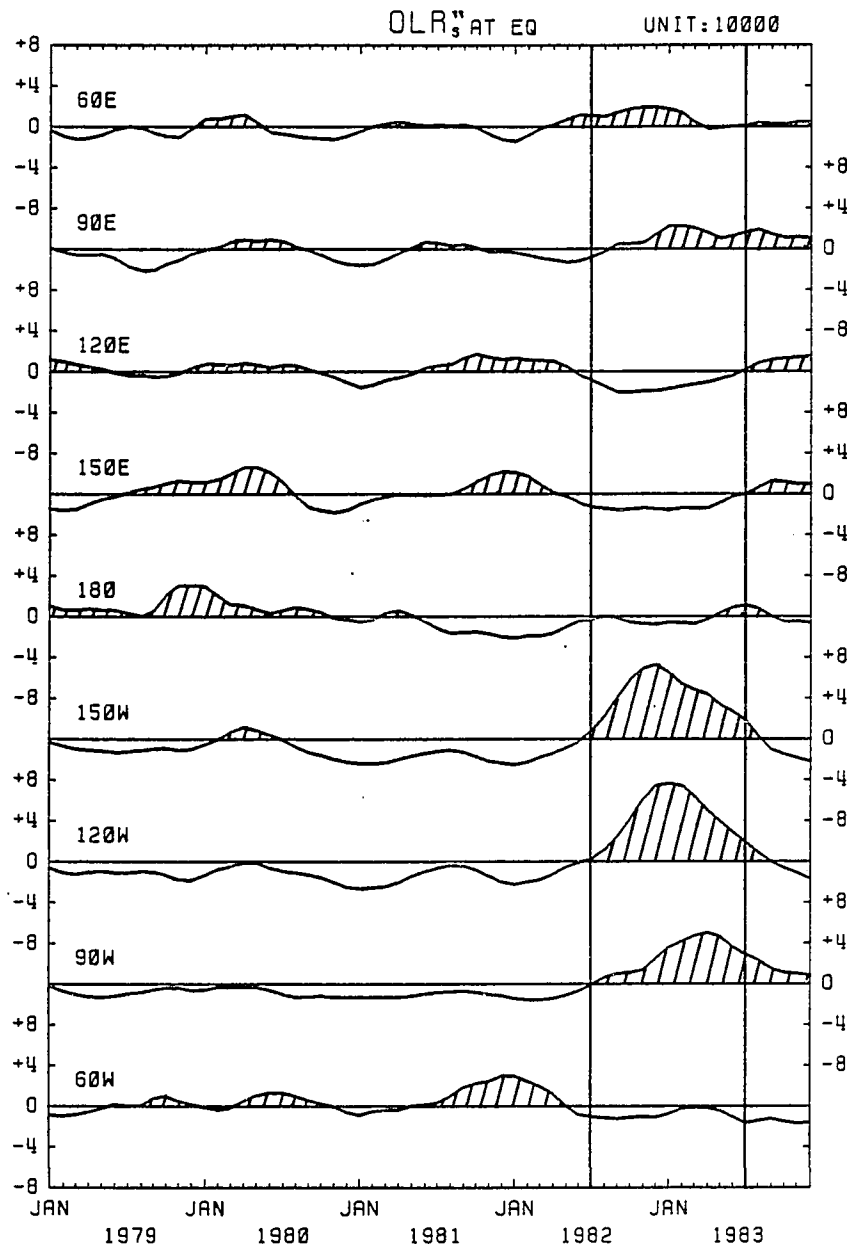


Fig. 5.6 As in Fig. 5.2, except for 2-15 day convective activity OLR<sub>2-15</sub>.

interannual modes (refer to Figs. 4.4 and 4.7). In fact, above normal  $OLR_g''$  activity is always encountered in regions of eastward propagating  $OLR'' < 0$ , 200 mb  $u'' < 0$ , and 850 mb  $u'' > 0$ . Such structural features of the interannual modes would provide a favorable environment for the enhancement of short-period disturbance activity. The activation of  $OLR_g''$ , in turn, favors the intensification of interannual modes. Here, the speculation is that these mutual interaction processes are responsible, at least partially, for the development of the interannual ENSO modes over the eastern Pacific.

In Fig. 5.6, one also notes that over the western Pacific ( $120^\circ\text{E}-180^\circ$ ), short-period  $OLR_g''$  is depressed below normal during the ENSO. This is coincident with  $OLR'' > 0$  (below normal convection), 200 mb  $u'' > 0$  (anomalous westerlies), and 850 mb  $u'' < 0$  (anomalous easterlies). Further upstream over the Indian Ocean ( $60^\circ-90^\circ\text{E}$ ),  $OLR_g'' > 0$  is correlated with  $OLR'' < 0$ , 200 mb  $u'' < 0$ , and 850 mb  $u'' > 0$  during the ENSO. Recall that these conditions resemble the ENSO features over the equatorial eastern Pacific, implying an approximate in phase relationship between the interannual variations over the Indian Ocean and the eastern Pacific.

Since the strongest peak of  $OLR_g''$  activity occurs at  $150^\circ\text{W}$ , the daily time series of  $OLR'$ ,  $\bar{OLR}$ , and  $OLR^*$  at this location are presented in Fig. 5.7 from the first of May 1982 to the end of June 1983.  $OLR'$  is generally negative

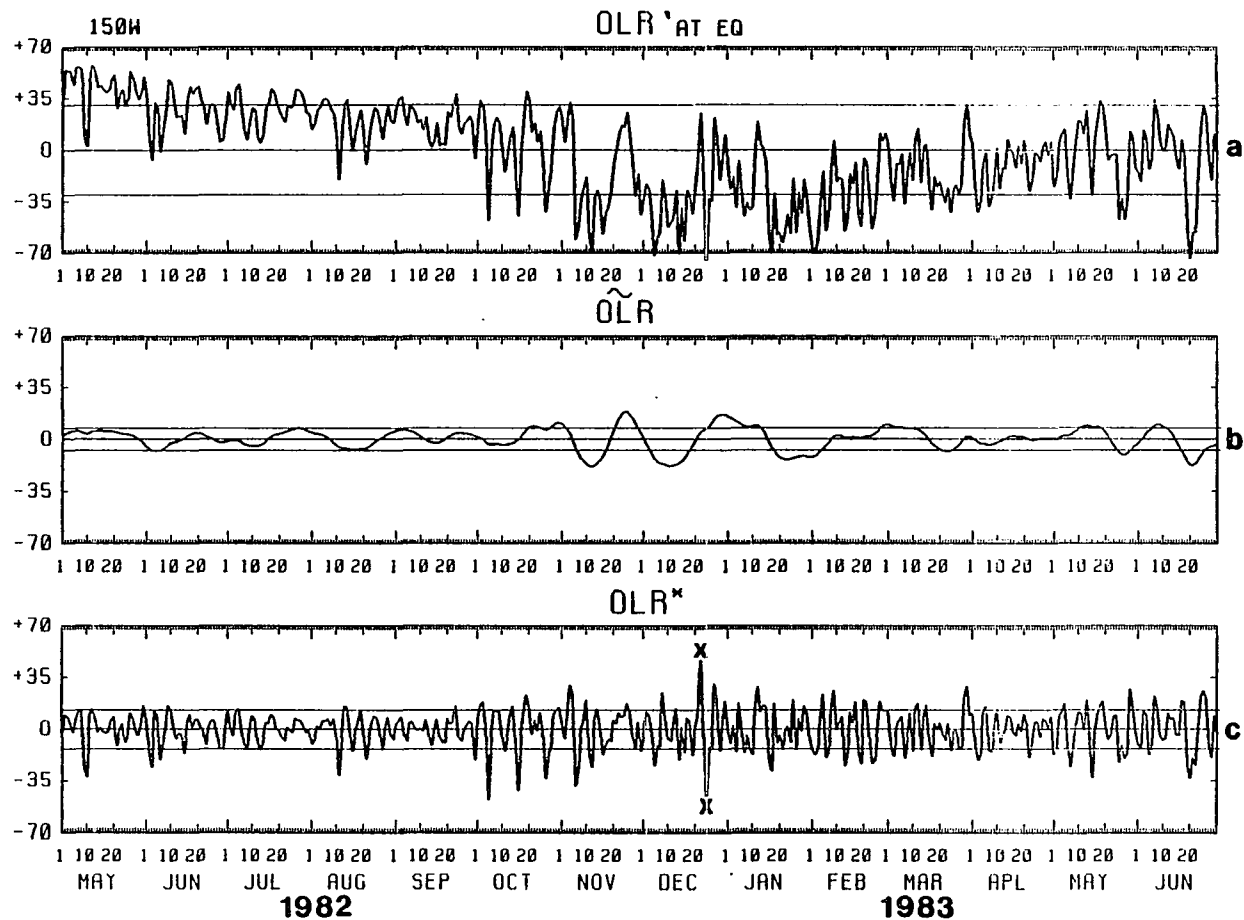


Fig. 5.7 As in Fig. 5.3, except for at (EQ., 150°W) from May 1st, 1982 to June 30th, 1983. The largest amplitude of OLR\* in (c) is marked by a letter x.

(below normal) over an extended period from about November 1982 to around April 1983. This results in a negative OLR<sup>''</sup> (above normal convection) during this particular ENSO period. Associated with this is the amplitude modulation of both 30-60 day OLR oscillation (Fig. 5.7b) and 2-15 day OLR\* disturbances (Fig. 5.7c), reflecting OLR<sub>L</sub><sup>''</sup>>0 (refer to Fig. 5.2) and OLR<sub>S</sub><sup>''</sup>>0 (refer to Fig. 5.6). Once again, the above results indicate the importance of intraseasonal disturbances (including 30-60 day oscillation and 2-15 day perturbations) upon interannual variations in terms of a modulation process.

The spatial structure and time evolution of short-time disturbances are exemplified in Fig. 5.8 with daily OLR\* maps for the period of Dec. 22-27 1982, which is one of the strongest amplitude episodes in Fig. 5.7c (denoted by the letter x). The negative OLR\* anomaly over 150°W, 30°S at Dec. 22 drastically intensifies on Dec. 23 with an equatorward movement. After reaching the equator on Dec. 24, it then propagates northeastward with areal expansion (Figs. 4.9d and 5.8e), followed by a decrease in intensity and a southward migration. An inspection of satellite cloud pictures (figures are not shown) during the same period reveals a good association between the negative OLR\* region and the individual cloud mass.

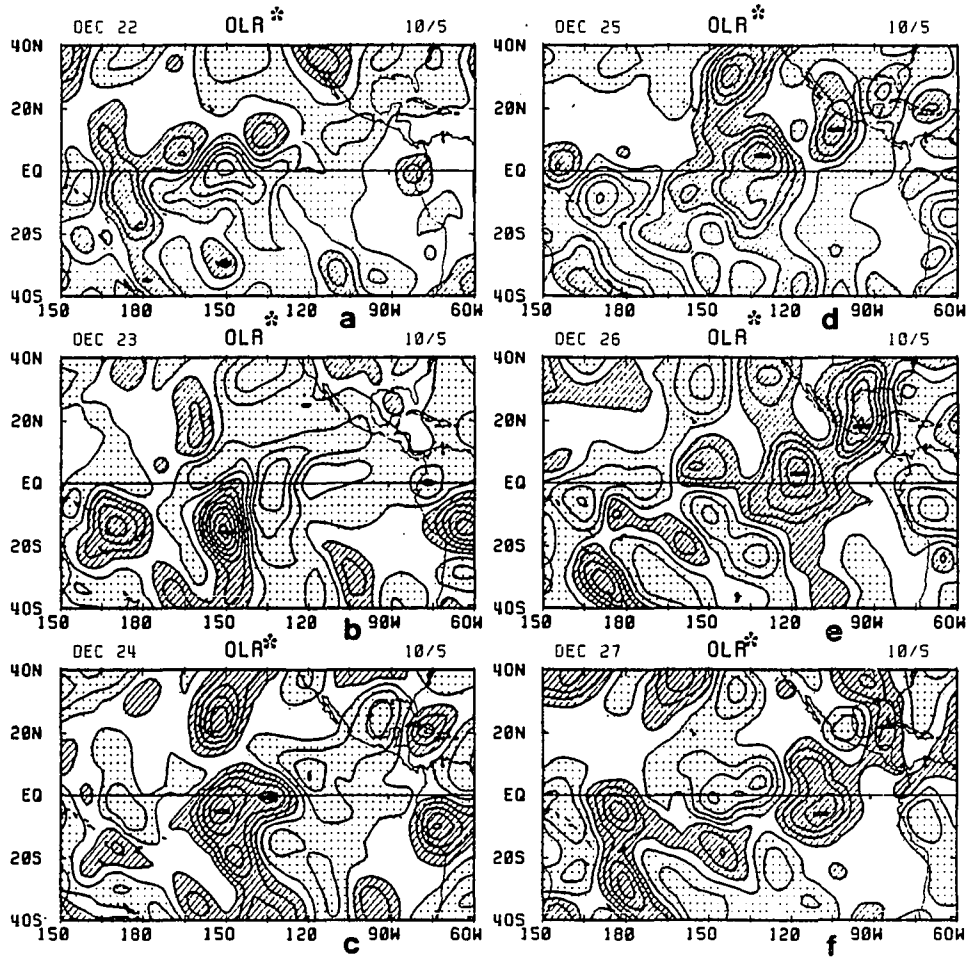


Fig. 5.8 As in Fig. 5.5, except for daily map of OLR\* over the eastern Pacific from Dec. 22 to Dec. 27 1982.

#### 5.4. Global-Scale Synoptics of Interannual Modes

This section investigates the difference in the planetary aspects of interannual modes between the two contrasting phases of the 1982/83 ENSO cycle, namely, the pre-ENSO [JAN(-1)] or post-ENSO [DEC(0)] phase and mid-ENSO [JAN(0)] phase. Separate synoptic maps of atmospheric parameters for JAN(0), JAN(-1), and DEC(0) exhibit many well defined features characteristic of these two contrasting climatic phases.

##### 5.4.1. JAN(0) Circulation Patterns

JAN(0) corresponds to time of the peak 1982/83 ENSO. The OLR" field for JAN(0), as shown in Fig. 5.9a, resembles the E<sub>1</sub> pattern presented in Fig. 4.4a. The Indian Ocean and the central Pacific are two of the most convectively active (OLR"<0) equatorial regions during the mid-ENSO state. These convectively active, updraft centers are indicated by a symbol "U" in Fig. 5.9a. Conversely, two of the anomalously dry (OLR">0), downdraft equatorial regions (denoted as "D") are located near the maritime continent and Brazil, respectively. As confirmed by Ardanuy and Krishnamurti (1987), negative (positive) interannual OLR" anomalies generally coincide with regions of upper tropospheric divergence (convergence) overlying low-level convergence (divergence). Thus, two cells of E-W oriented equatorial overturning are implied with updraft U branches

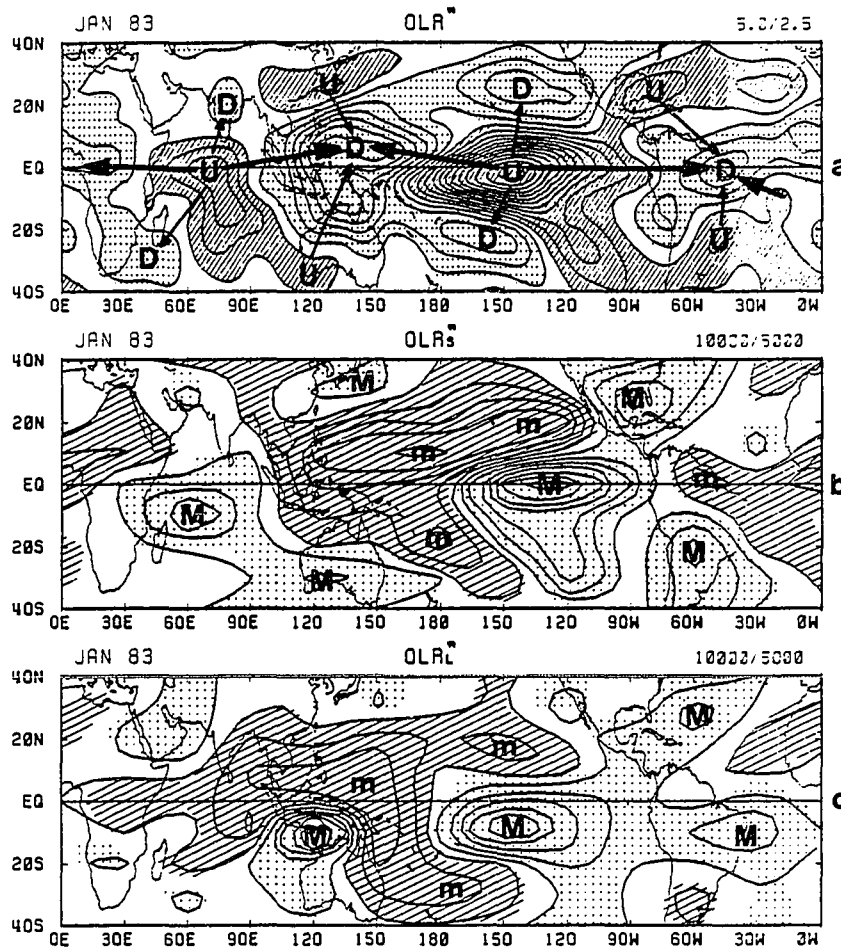


Fig. 5.9 Mid-ENSO (January 1983) patterns for  $OLR''$  (a;  $5 \text{ Wm}^{-2}$  unit),  $OLR_S''$  (b;  $10^4 \text{ W}^2\text{m}^{-4}\text{day}$  unit), and  $OLR_L''$  (c;  $10^4 \text{ W}^2\text{m}^{-4}\text{day}$  unit). Interval is 1 unit. Light mesh (hatching) indicates regions of greater (less) than +0.5 (-0.5) unit; no zero lines. The letter U (D) in (a) denotes updraft or convection (down-draft or non-convection) region, and M (m) in (b) and (c) indicates maximum (minimum) convective activity. The heavy (light) arrows in (a) indicates anomalous Walker (local Hadley) circulation.

over the Indian Ocean and the central Pacific, and downdraft D branches over the maritime continent and Brazil. Upper-level divergent outflows from U centers are directed to the west (east) as easterlies (westerlies), as indicated by the heavy arrows in Fig. 5.9a. Here, the salient feature is the extremely strong divergent easterlies blowing between dipole OLR<sup>"</sup> axes over the maritime continent-central Pacific region. Upper-level divergent outflows from equatorial U centers are also directed poleward and converge into extratropical downdraft D centers of the two hemispheres, implying the development of anomalous direct N-S vertical circulation, as represented by thin arrows in Fig. 5.9a. Conversely, reverse N-S overturnings connect the equatorial D centers with extratropical U centers. The direct N-S overturning is strongest along about 150°W with an ascending portion (U) over the equatorial Pacific and descending portions (D) over the extratropical North and South Pacific. This is contrasted with a prominent reverse N-S cell between about 120°E and 150°E with downdrafts (D) near the maritime continent and updraft (U) near Southern Japan and Australia.

The N-S, as well as E-W, vertical circulations mentioned above appear to exert some measure of control upon the intraseasonal convective activity of OLR<sub>S</sub><sup>"</sup> (Fig. 5.9b) and OLR<sub>L</sub><sup>"</sup> (Fig. 5.9c). In these figures, the symbol "M" denotes regions of maximum (above normal) intraseasonal

convective activity, while "m" represents minimum (below normal) activity. A glance at Figs. 5.9a and 5.9b reveals a good correspondence between U centers for  $OLR''$  and M centers for  $OLR_S''$ . Namely, the space scale of  $OLR_S''$  is comparable to that of interannual  $OLR''$  modes. This, in turn, indicates the importance of assembling a climatology of short-period (2-15 day) convective activity. It is also necessary to monitor 30-60 day convective activity ( $OLR_L''$ ) as an important index for climatic variations. In Figs. 5.9a and 5.9c, one notes a fairly good agreement between U centers for  $OLR''$  and M centers for  $OLR_L''$ , especially over the Pacific region where ENSO signals are strongest. The main discrepancies between Figs. 5.9a and 5.9c are over the Indian Ocean where 30-60 day convective activity is generally above normal during non-ENSO periods, and below normal in ENSO episode. Thus,  $OLR_L''$  mode and  $OLR_S''$  mode have different natures in relation to interannual  $OLR''$  variations as mentioned in section 3.3.3.

Figure 5.10a depicts the latitude-time section of the zonally averaged correlation between  $OLR''$  and  $OLR_S''$  computed at every 10 degrees of latitude from  $40^{\circ}N$  to  $40^{\circ}S$  for each month during the five years of 1979-83. Shading indicates regions of correlation of less than -0.3. Also shown is the latitudinal dependency of averaged correlation for the entire five years. The five-year mean correlation amounts to less than -0.4 at the equator. This is due to the

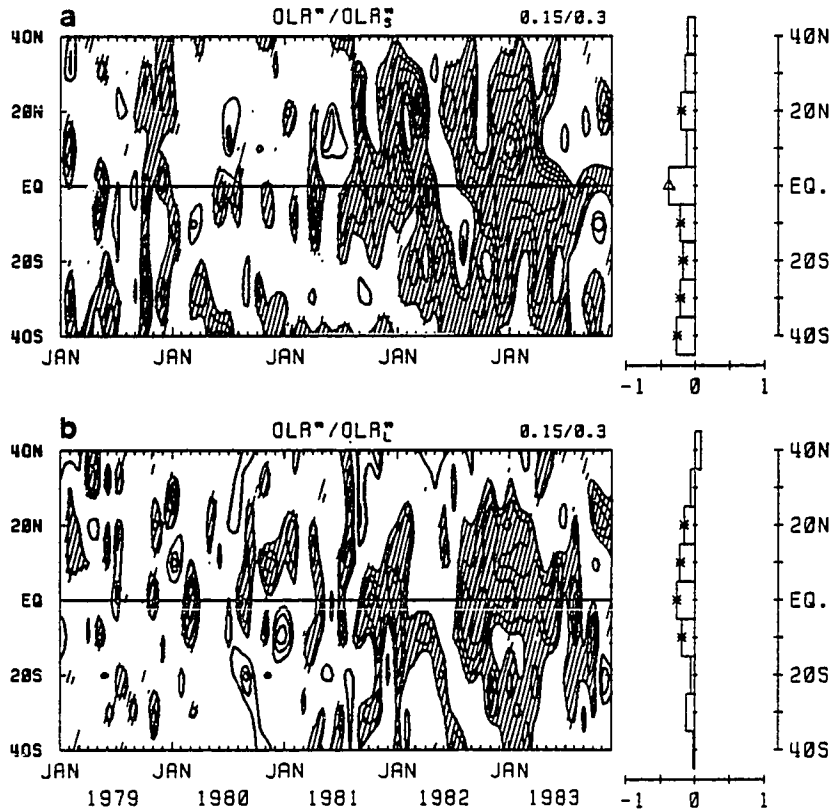


Fig. 5.10 Time-latitude section of zonally averaged correlation between  $OLR''$  and  $OLR_g''$  (a), and between  $OLR''$  and  $OLR_L''$  (b). Intervals are 0.15. Shading indicates negative correlation less than -0.3. The 5-year mean correlations are also shown at the right end of the diagram, triangle (asterisk) denotes mean correlation exceeding 0.5 (0.3).

contribution of large negative correlation after about August, 1981. More specifically, negative correlation of less than  $-0.5$  at the equator occurs during the pre to onset period of December, 1981 to April, 1982; as well as in the mature to late ENSO phase from October, 1982 to June, 1983. Curiously, the correlation approaches zero, or even becomes slightly positive during the onset phase of the 1982 summer. Similarly, the correlation between  $OLR''$  and  $OLR_L''$  (Fig. 5.10b) also reduces to near zero prior to and during the onset phase. A sketchy examination of monthly  $OLR''$ ,  $OLR_L''$ , and  $OLR_S''$  maps indicates that zonal phase differences between  $OLR_L''$  or  $OLR_S''$  patterns and  $OLR''$  distributions exist prior to and during the onset phase of the 1982/83 ENSO. This probably results in the poor correlation during this period. Interestingly in Fig. 5.10a, the correlation pattern after October, 1981 has a clear northwest-southeast tilt. Here, the indication is  $OLR_S''$  activity which originates in the Northern Hemisphere midlatitudes affects the Southern Hemisphere, suggesting the importance of the Northern Hemisphere upon development of interannual modes. The above results are in agreement with those discussed in Fig. 4.10a for the phase differences between  $OLR_S''$  and  $OLR''$ .

Global-scale interannual  $OLR''$  convection (Fig. 5.9a) certainly affects tropospheric flow patterns. This is demonstrated in Fig. 5.11a, showing  $(u'', v'')$  wind vectors

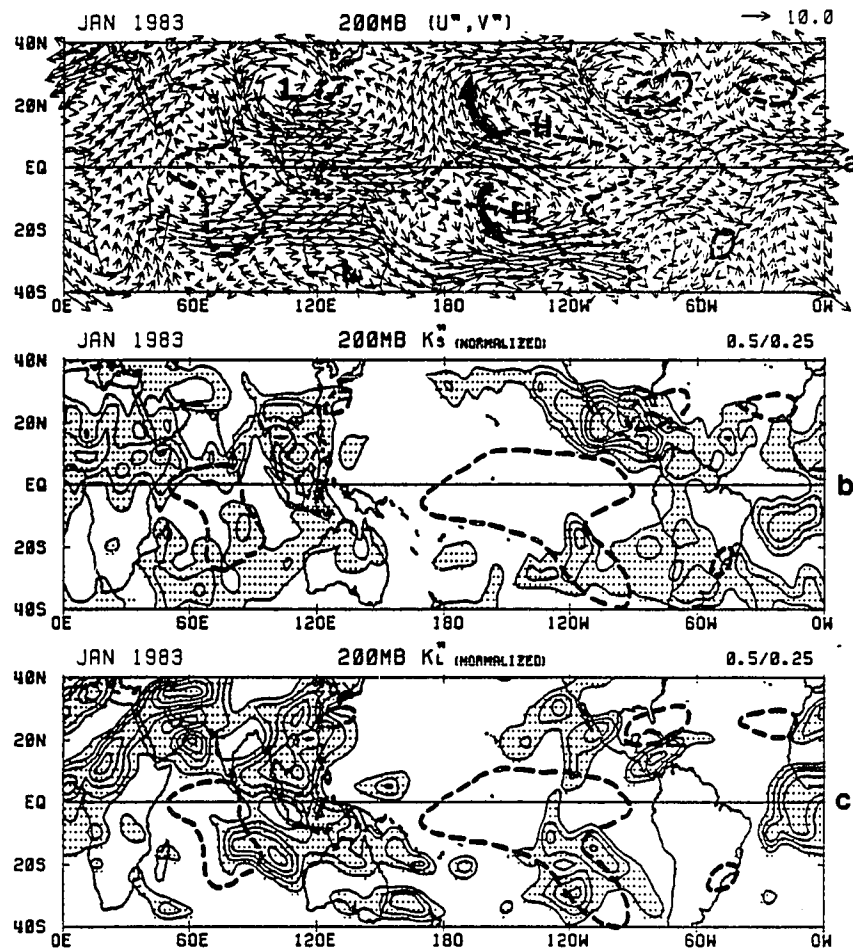


Fig. 5.11 Mid-ENSO (January 1983) patterns for  $(u'', v'')$  vectors (a),  $K_S''$  (b), and  $K_L''$  (c) at 200 mb. Unit vector is  $10 \text{ ms}^{-1}$  and major distributions are indicated by H and L. Heavy dashed lines denotes regions of  $OLR''$  less than  $-7.5 \text{ Wm}^{-2}$ . Intervals for normalized  $K_S''$  and  $K_L''$  are 0.5; light mesh indicates regions greater than 0.25 (no zero and negative contours).

at 200 mb in JAN(0). Of interest is a near symmetric configuration of ( $u''$ ,  $v''$ ) vectors with respect to the equator. To the north and south of the most intense convective cell situated over the equatorial eastern Pacific are well organized upper-level anticyclones with equatorial easterlies between them. Poleward of these twin anticyclonic cells, anomalous westerlies dominate the extratropical North and South Pacific where downdrafts ( $OLR'' > 0$ ) are predominant (Fig. 5.9a). One also should not overlook the presence of strong poleward meridional ( $v''$ ) flows prevailing to the west of the twin anticyclones in Fig. 5.11a. These poleward flows, which represent upper-level branches of the anomalous direct N-S cell mentioned earlier, presumably contribute to the acceleration of mid-latitude westerlies over the North and South Pacific. With reference to a relatively weak convection region over the Indian Ocean, there exist less distinct equatorial easterlies with ill-organized twin anticyclones and mid-latitude westerlies to the north and south.

As for the anomalously dry ( $OLR'' > 0$ ) regions of the maritime continent and equatorial Brazil (Fig. 5.9a), one at once notes the existence of equatorial westerlies sandwiched between twin cyclonic cells in the extratropics of both hemispheres (Fig. 5.11a). For example, a pair of well-defined cyclonic cells over Southern China and Southern Australia are separated by exceptionally strong

equatorial westerlies in excess of  $10 \text{ ms}^{-1}$  (anomaly) over the maritime continent.

Figures 5.11b and 5.11c present the horizontal distribution of  $K_S''$  and  $K_L''$  (Eqs. 5 and 6) at 200 mb in JAN(0). These values are normalized by the local standard deviations of  $K_S''$  and  $K_L''$ , respectively. Shading indicates regions of above normal  $K_S''$  and  $K_L''$  activity exceeding more than 25 percent of the local standard deviations. Here, note that contours of negative (below normal)  $K_S''$  and  $K_L''$  are not shown in Figs. 5.11b and 5.11c.

Recall that over the eastern Pacific between about the date line and  $120^\circ\text{W}$  a marked direct N-S vertical overturning (anomaly) is dominant (Fig. 5.11a). For brevity, this region of direct N-S circulation is designated as the DNS zone. The date line acts as a separator with equatorial easterlies (westerlies) to the east (west). The most important feature detected in the DNS zone is that the eddy kinetic energy for a 2-15 day period range ( $K_S''$ ) at 200 mb is depressed well below normal in and around equatorial convection ( $\text{OLR}'' < 0$ ). Perhaps, upper-level equatorial easterlies inhibit the development of short-period transient disturbances. Further poleward of the equator are regions of substantially large  $K_S''$ , which are embedded within the extratropical  $u''$  westerlies over the North and South Pacific. This suggests a possible interaction between tropical convection ( $\text{OLR}'' < 0$ ) and midlatitude

circulation across the deep equatorial easterly flow ( $u'' < 0$ ) over the DNS zone. Most theoretical studies of tropical-extratropical interaction focus on the effect of Rossby-wave propagation into and out of the tropics through upper-level westerlies (e.g., Hoskins and Karoly, 1981; Lau and Lim, 1984). Recently, Sardeshmukh and Hoskins (1987) emphasized the importance of the advection of vorticity due to the divergent component of the winds when a direct N-S overturning intensifies. This advective effect which occurs in response to equatorial forcing or heating ( $OLR'' < 0$ ), then leads to strong Rossby-wave activity in the extratropical westerlies. The intensification of mid-latitude westerlies favors the development of short period baroclinic unstable waves.

Transient eddy kinetic energy for a 30-60 day period range, i.e.,  $K_L''$ , is also prominent in the extratropical westerlies of the DNS zone (Fig. 5.11c). Similar to the  $K_S''$  mode,  $K_L''$  is generally small in regions of equatorial easterlies.

As mentioned earlier, the Japan-maritime continent-Australia region between about  $100^\circ$  and  $160^\circ$ E is characterized by a reverse N-S vertical overturning, and thus, will be denoted hereafter as the RNS zone. Some of the characteristic features of this RNS zone can be summarized as follows: (1) Depressed convection ( $OLR'' > 0$ ) near the equator as contrasted with substantial convection ( $OLR'' < 0$ )

over southern Japan and southern Australia (Fig. 5.9a), (2) deep upper-tropospheric westerlies covering Indochina, Sumatra, Borneo, and northern Australia (Fig. 5.11a), (3) a distinct bridge of large  $K_S''$  across the upper-level  $u''$  westerly flows (Fig. 5.11b), and (4) a close association of large  $K_L''$  with strong  $u''$  westerlies (Fig. 5.11c). There are some theoretical explanations for the above observational results. Based on a barotropic model, Webster and Holton (1982) have shown that equatorial regions of anomalously large eddy kinetic energy are a result of the propagation of extratropical synoptic and low-frequency waves through the upper tropospheric westerly duct. Their theoretical study was essentially motivated by the observational evidence (Murakami and Uuninayar, 1977) in which a large eddy kinetic energy bridge connecting the two hemispheres over the eastern Pacific had been found during January and February 1971, an pre-ENSO phase with respect to the 1972/73 ENSO. Webster, Chang, and Min (1987) have recently expanded on this perspective by pointing out that energy can also be conveyed longitudinally along the equator from the convection source region to the vicinity of the equatorial westerlies where an accumulation of transient energy due to longitudinal trapping occurs. Perhaps this new theory, together with the previous one, can account for the large longitudinal difference in  $K_S''$  and  $K_L''$  along the equator between the DNS and RNS zones.

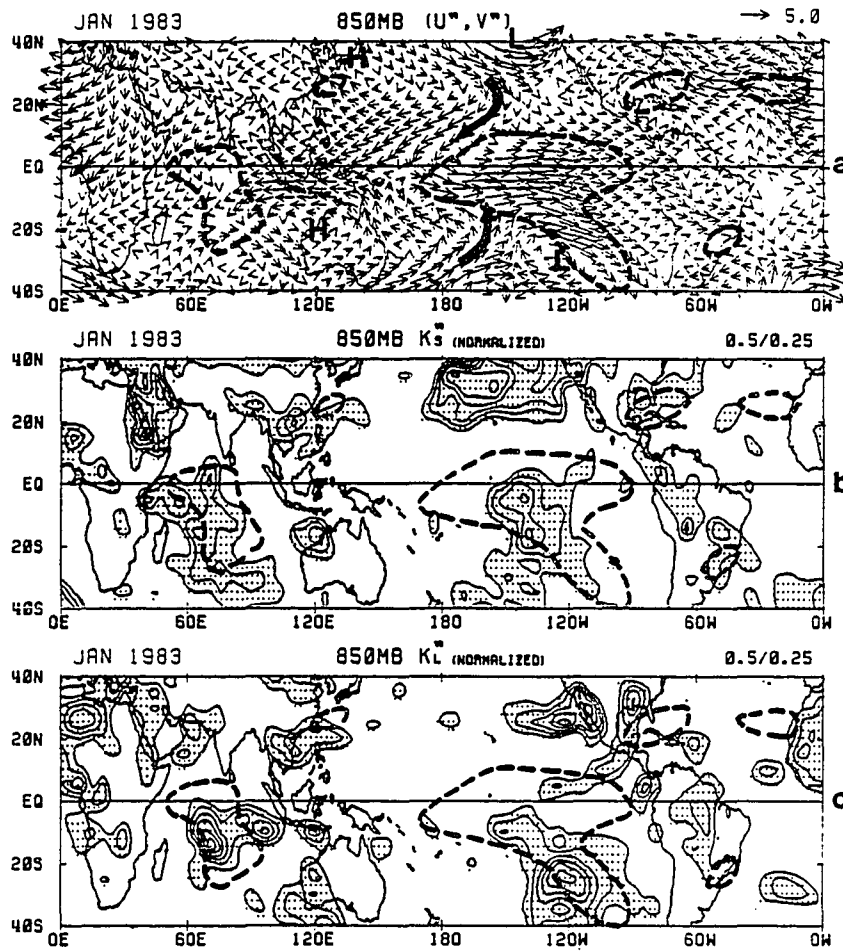


Fig. 5.12 As in Fig. 5.11, except for the 850 mb level.

Figure 5.12a depicts the 850 mb ( $u''$ ,  $v''$ ) wind fields and provides important information pertaining to the tropical-extratropical interaction on the interannual time scale. Over the equatorial eastern (western) Pacific, 850 mb westerlies (easterlies) are capped by the easterlies (westerlies) at 200 mb. This equatorial baroclinic wind system represents an anomalous Walker circulation during the mid-ENSO state. Over the majority of the extratropics poleward of about  $30^\circ$ , 850 mb ( $u''$ ,  $v''$ ) winds are in phase with 200 mb ( $u''$ ,  $v''$ ) winds; namely, they are barotropic in the vertical.

Pointed out earlier, the western end of the Indian Ocean is the possible breeding place of low-level equatorial  $u''$  westerlies. They then propagate eastward, eventually reaching the eastern Pacific by JAN(0) as evident in Fig. 5.12a. At this time, regions of equatorial westerlies ( $u'' > 0$ ) over the eastern Pacific are coincident with anomalous equatorial convection ( $OLR'' < 0$ ; Fig. 5.9a), large  $OLR_S''$  (Fig. 5.9b), large 850 mb  $K_S''$  (Fig. 5.12b), and small 200 mb  $K_S''$  (Fig. 5.11b). Thus, short-period (2-15 day) convective activity ( $OLR_S''$ ) is primarily controlled by low-level transient eddies, i.e., 850 mb  $K_S''$ , while, 200 mb  $K_S''$  contributes little to  $OLR_S''$  activity. On the other hand, the 30-60 day  $K_L''$  modes over the equatorial eastern Pacific, are equally important at both 850 mb (Fig. 5.12c) and 200 mb (Fig. 5.11c) levels, indicating that the vertical extent

of 30-60 day transients is presumably deeper than the 2-15 day counterparts, i.e., the barotropic nature.

The most important indication in Fig. 5.12a is that the equatorial meridional  $v''$  flows which prevail to the west of the twin cyclones over the extratropical North and South Pacific, appear to make some contribution to equatorial  $u''$  westerlies and associated convection ( $OLR'' < 0$ ). In Fig. 5.12a heavy arrows indicate equatorward meridional flows along about the date line, these equatorward flows represent low-level branches of an anomalous Hadley-type circulation over the DNS zone. These  $v''$  flows of Northern Hemisphere (NH) and Southern Hemisphere (SH) extratropical origin turn eastward as the equator is approached and converge into the equatorial convective region. Equatorward  $v''$  flows are particularly strong to the west of the anomalous South Pacific cyclonic system centered at  $35^{\circ}\text{S}$  and  $120^{\circ}\text{W}$ . Namely, in JAN(0) the SPCZ becomes abnormally strong and dominates the South Pacific with significant  $u''$  westerlies extending as far east as South America.

Over the RNS zone ( $100^{\circ}$ - $160^{\circ}\text{E}$ ), the 850 mb ( $u''$ ,  $v''$ ) fields are largely regulated by twin anticyclones centered over Japan and western Australia, respectively. Equatorward of these twin anticyclones are anomalous easterlies covering an extensive latitude band from about  $30^{\circ}\text{N}$  to  $20^{\circ}\text{S}$ . Lau and Lim (1984) have shown that their numerically simulated zonal wind perturbations are symmetric with

respect to the equator and are confined within a narrow equatorial belt between about  $10^{\circ}\text{N}$  and  $10^{\circ}\text{S}$ . Namely, the latitudinal extent of the simulated equatorial modes are approximately determined by the equatorial radius of deformation, which is the characteristic scale of equatorial dynamics. Hence, the observed interannual  $u''$  westerlies and easterlies in Fig. 5.12a cannot be regarded as pure equatorial modes. They are regulated not only by equatorial convective heating which can be viewed as an oceanic influence, but also by some means of extratropical circulation forcing, as evident by the strong equatorward meridional flows in Fig. 5.12a.

Within the RNS zone, 850 mb  $K_S''$  and  $K_L''$  activity (Figs. 5.12b and 5.12c) are pronounced over the NH and SH subtropics including Indochina, the Philippines, and west Australia, while they are depressed over the Indonesian Seas in JAN(0). This is consistent with persistent dry weather ( $\text{OLR}'' > 0$ ) over the SH summer monsoon region during the mature ENSO stage (Fig. 5.9a). In other words, JAN(0) corresponds to the peak break monsoon with much less pronounced low-level disturbance activity than normal. This stands in sharp contrast with above normal  $K_S''$  and  $K_L''$  at 850 mb over the eastern equatorial Pacific.

Together, figs. 5.9, 5.10, and 5.11 reveal that interannual motion fields ( $u''$ ,  $v''$ ), as well as anomalous convection fields  $\text{OLR}''$ , appear to exert some measure of control

upon the interannual variability of intraseasonal disturbance activity as defined by  $OLR_S''$ ,  $K_S''$ ,  $OLR_L''$ , and  $K_L''$ . Combining the information obtained so far, a schematic model is proposed which establishes the relationship between  $OLR''$ ,  $(u'', v'')$ ,  $OLR_S''$ , and  $K_S''$  over the DNS zone ( $180^\circ-120^\circ W$ ) during the mid-ENSO of JAN(0) as shown in Fig. 5.13. The relationship between  $OLR''$ ,  $(u'', v'')$ ,  $OLR_L''$ , and  $K_L''$ , is identical to Fig. 5.13, except for some discrepancies between  $K_S''$  and  $K_L''$  discussed in the text, and thus, it is not reproduced here.

The characteristic features noted in Fig. 5.13 for the DNS zone are summarized as follows:

- A. An equatorial updraft region of  $OLR'' < 0$ 
  - A.1. 850 mb  $u''$  westerlies accompanied by strong low-level eddy kinetic energy  $K_S''$  and pronounced short-period (2-15 day) convective activity  $OLR_S''$ ; here, there is a need for a moist multi-level model to simulate these convective low-level disturbances.
  - A.2. Asymmetric low-level  $u''$  westerlies with respect to the equator with their latitudinal extension requiring an improved tropical-extratropical interaction dynamics.
  - A.3. 200 mb  $u''$  easterlies probably inhibit short period disturbance activity.
- B. Midlatitude downdraft regions of  $OLR'' > 0$

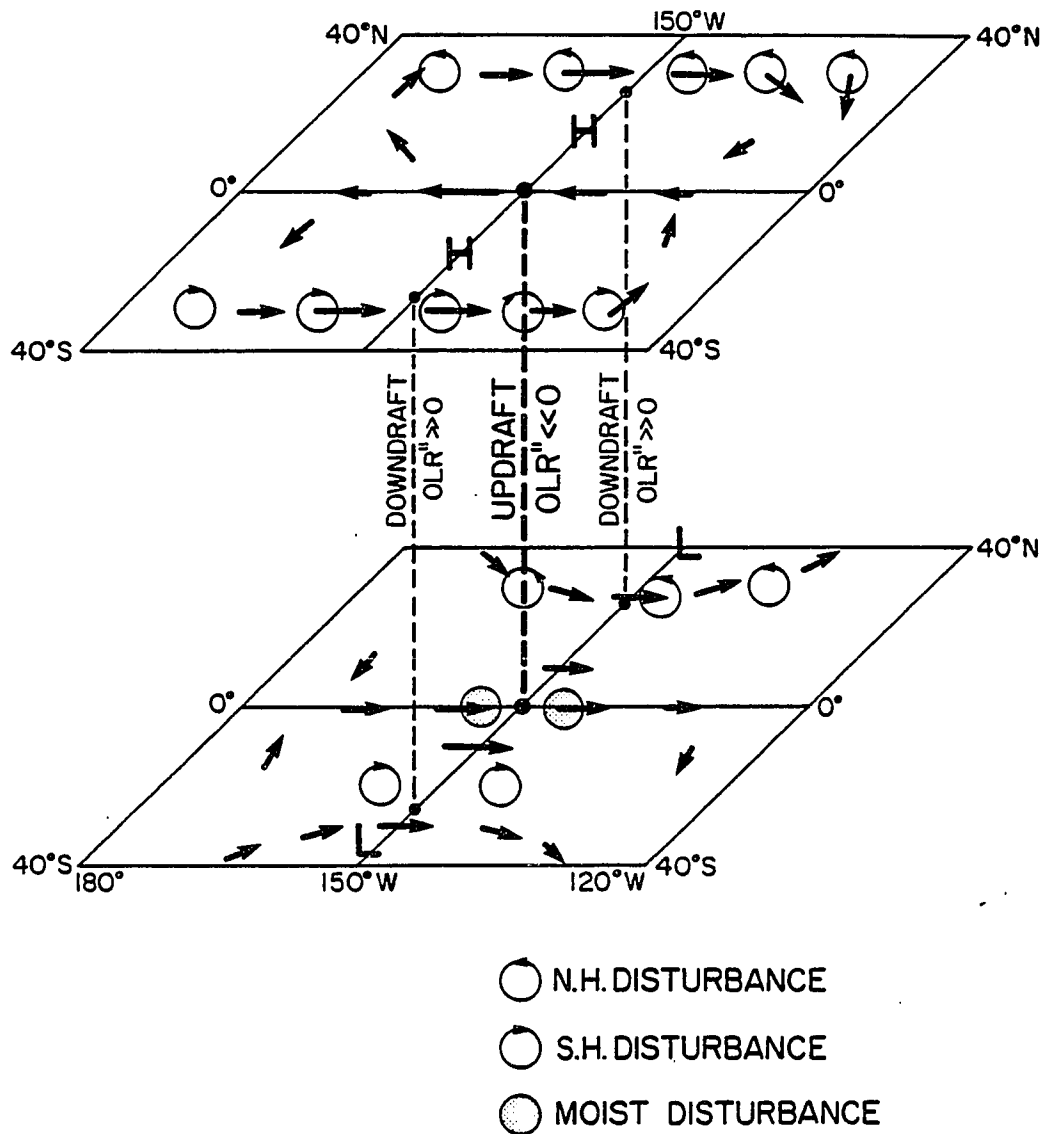


Fig. 5.13 Schematic diagram for a direct N-S vertical overturning (anomaly) occurring over the eastern North and South Pacific ( $180^{\circ}$ - $120^{\circ}$ W) during the mid-ENSO phase of January 1983.

- B.1. Westerly  $u''$  flows at both 850 and 200 mb, suggesting the barotropic nature of mid-latitude interannual modes.
- B.2. Significant  $K_S''$  activity at both 850 and 200 mb, reflecting the development of baroclinic unstable waves in the anomalous  $u''$  westerlies.
- B.3. Quite small  $OLR_S''$ , indicating weak short-period rainfall variations.

The schematic diagram for the RNS zone ( $100^{\circ}$ - $160^{\circ}$ E) shown in Fig. 5.14, is likewise proposed from the discussion of the observational evidence. Here, the following noteworthy aspects are depicted:

- A. Equatorial downdraft region of  $OLR'' > 0$ .
  - A.1. 850 mb  $u''$  easterlies, depressed short-period convective activity  $OLR_S''$ , and small transient eddy kinetic energy  $K_S''$ .
  - A.2. Strong 200 mb  $u''$  westerlies enhancing upper-level transient disturbance activity, i.e., large  $K_S''$ .
- B. Subtropical updraft regions of  $OLR'' > 0$ .
  - B.1. Pronounced 200 mb  $u''$  westerlies and associated short-period wave activity  $K_S''$ .
  - B.2. Significant 850 mb  $K_S''$  activity and substantial short-period rainfall variation, namely, very large  $OLR_S''$ .

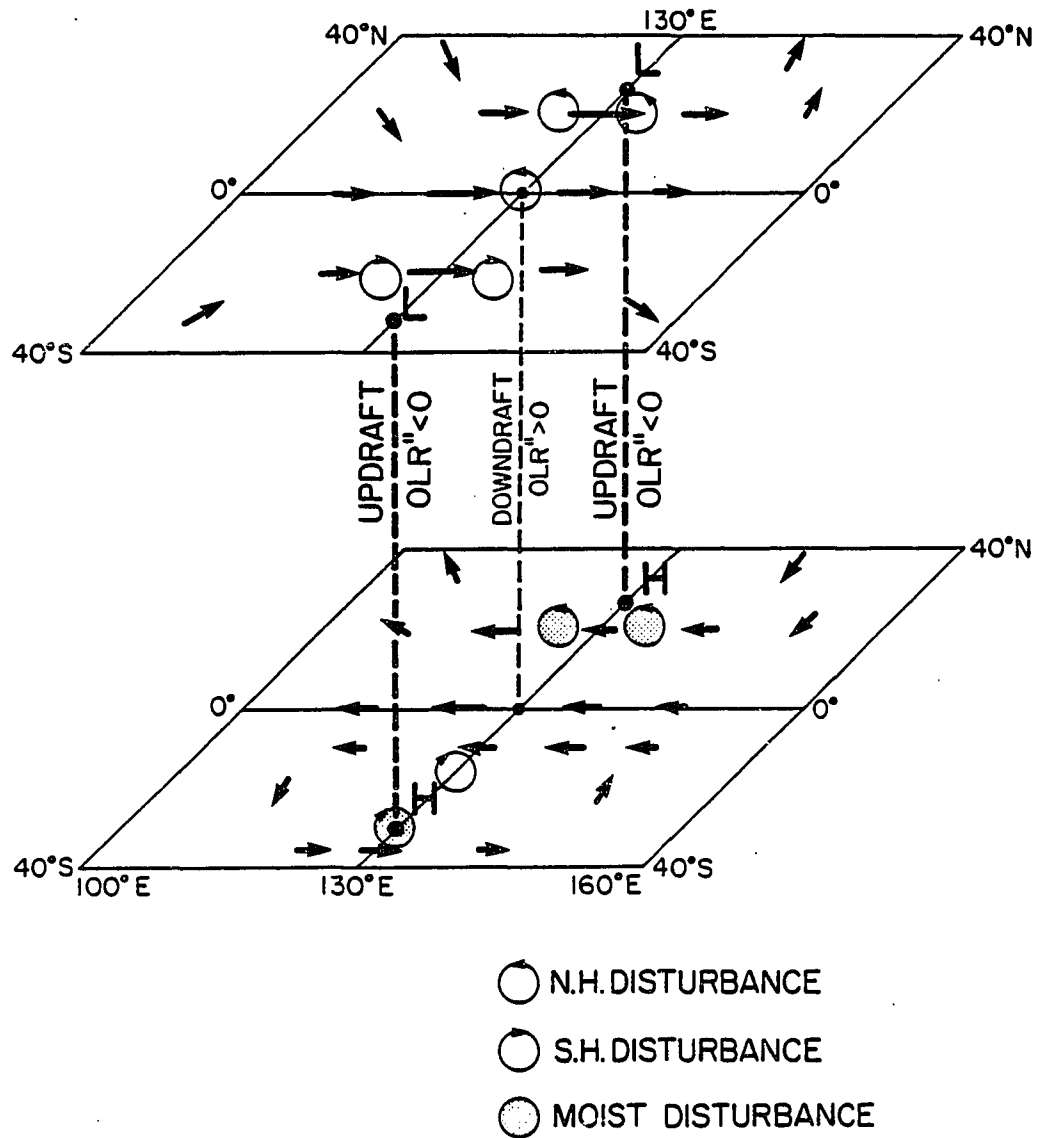


Fig. 5.14 As in Fig. 5.13, except for an indirect N-S vertical overturning (anomaly) over the Japan-maritime continent-Australia region ( $100^{\circ}$ - $160^{\circ}$ E).

#### 5.4.2. JAN(-1) Circulation Patterns

As shown in Fig. 4.4c,  $SOI''$  reaches a maximum (positive) around January 1982. Thus, the pre-ENSO phase of JAN(-1) most probably represents an extreme of non-ENSO steady state. There exists an approximate inverse relationship between the  $OLR''$  patterns in Fig. 5.15a for JAN(-1) and those in Fig. 5.9a for JAN(0). Similarly, the 200 mb ( $u''$ ,  $v''$ ) wind fields in Fig. 5.16a for JAN(-1) are essentially identical, without regard to the signs, to those in Fig. 5.11a for JAN(0). The inverse relationship between the 850 mb ( $u''$ ,  $v''$ ) winds in Fig. 5.17a for JAN(-1) and those in Fig. 5.12a for JAN(0) generally hold, especially over the DNS zone. The same check that was earlier applied to  $OLR''(I)$ , as discussed in the Section 4.2.3., was used here for both the OLR and wind data. The results are that the large-scale features presented in Figs. 5.9a, 5.11a, and 5.12a for JAN(0) and in Figs. 5.15a, 5.16a, and 5.17a for JAN(-1) are essentially independent to their normal mean fields. Thus, January 1982 (January 1983) is most probably indicative of an extreme of the non-ENSO (ENSO) steady state, namely, anti-ENSO (mid-ENSO) phase. Since the 5-year data set used in this study is too short to precisely estimate the normal annual cycle, and to reliably define the anti-ENSO phase, further investigation using a data set with longer time period is necessary.

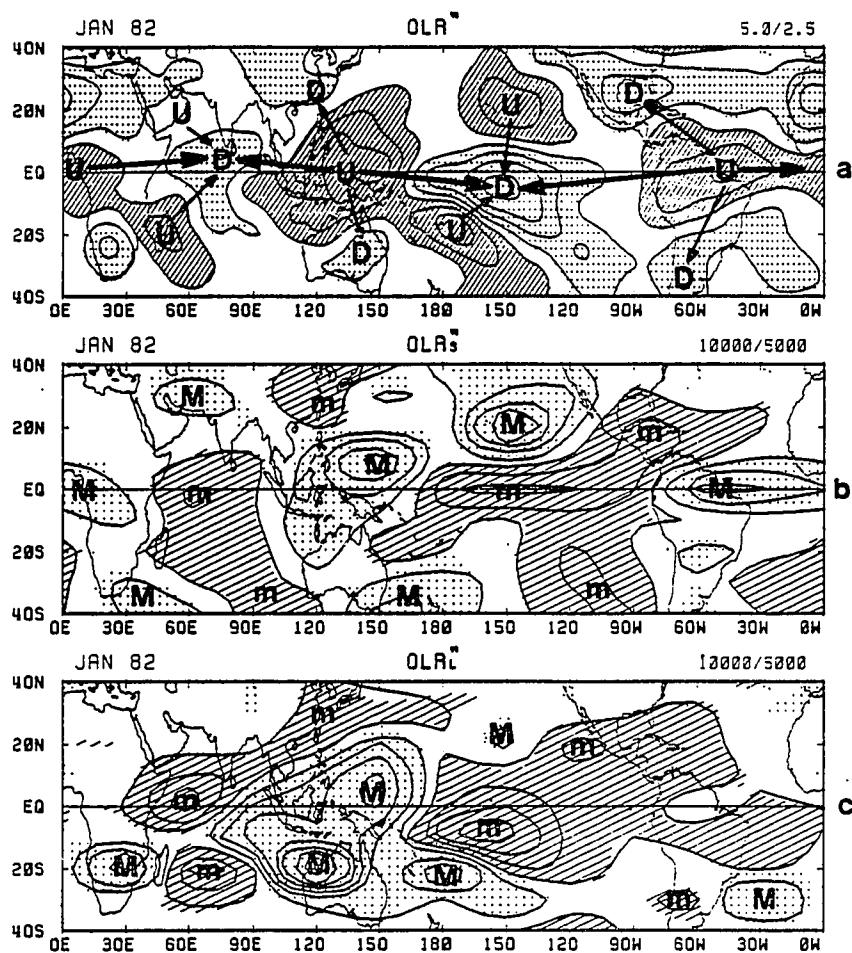


Fig. 5.15 As in Fig. 5.9, except for the pre-ENSO phase of January 1982.

The OLR" pattern in JAN(-1) is nearly symmetrical with respect to the equator. Three regions of anomalous convection ( $OLR'' < 0$ ) are encountered over the maritime continent, Brazil, and Africa, respectively (Fig. 5.15a). These are also three of the most convectively active regions during a normal winter. The 200 mb ( $u''$ ,  $v''$ ) pattern in JAN(-1) likewise exhibits an almost symmetric character with pairs of NH and SH cyclones straddling the equator over the central North and South Pacific (Fig. 5.16a). This is the manifestation of an anomalous intensification of upper oceanic troughs in the pre-ENSO JAN(-1), a likely representative of anti-ENSO phase, as compared to a normal winter. The equatorial westerlies between these twin cyclones are overlying the 850 mb easterlies (Fig. 5.17a), indicating the baroclinic nature of tropical wind fields. However, the barotropic nature of the midlatitude ( $u''$ ,  $v''$ ) winds is much better defined in the NH than in the SH over the Pacific.

Another interesting feature in Fig. 5.16a is the existence of anomalous anticyclonic cells over southern China and southern Australia, respectively. These anticyclones (anomaly) are a result of a phase locking with the annual cycle of the upper tropospheric circulations; namely, the anomalous intensification of monsoonal anticyclones at 200 mb in JAN(-1). The 850 mb ( $u''$ ,  $v''$ ) winds are much weak over the eastern Asia-maritime continent-Australia region,

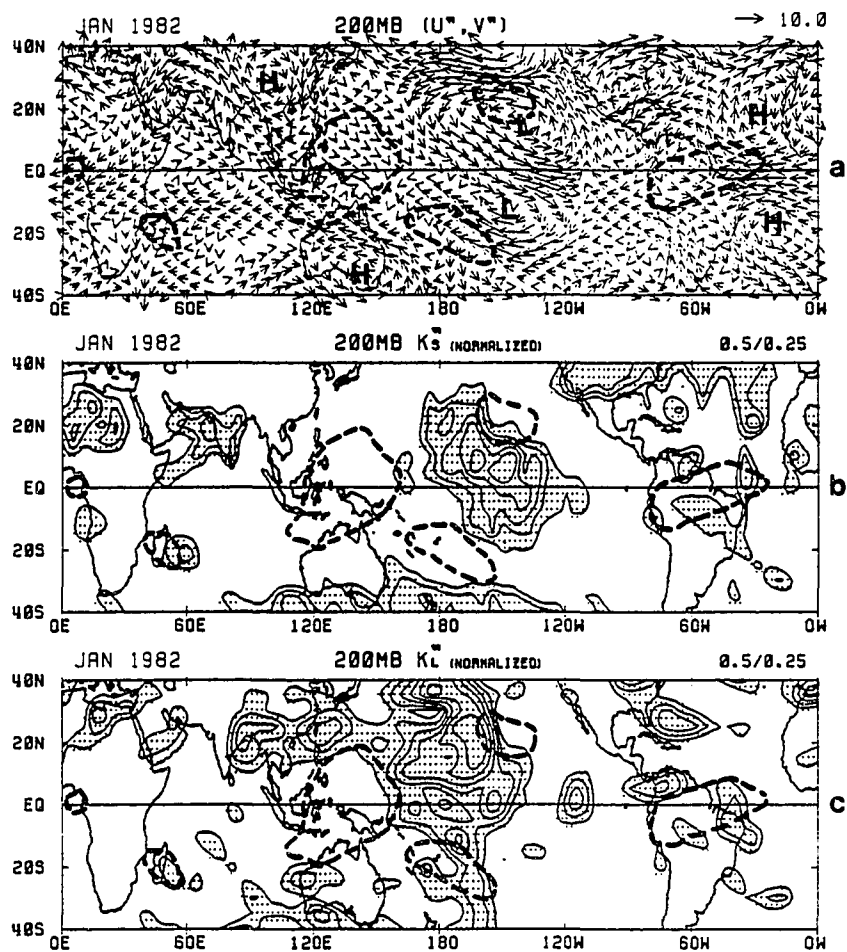


Fig. 5.16 As in Fig. 5.11, except for the pre-ENSO phase of January 1982.

reflecting the much shorter time scale of prevailing wind variations over monsoonal areas.

A nearly complete reversal also occurs in local N-S vertical overturning. Between about  $100^{\circ}$  and  $160^{\circ}$ E in JAN(-1) is a direct N-S vertical circulation (anomaly) with an updraft portion (U;  $OLR'' < 0$ ) over the maritime continent and downdraft portions (D;  $OLR'' > 0$ ) over southern China and southern Australia (Figs. 5.15a and 5.16a). All diagrams for intraseasonal disturbance activity as shown in Figs. 5.15b-c, 5.16b-c, and 5.17b-c exhibit distinct features similar to those shown schematically in Fig. 5.13 for the DNS zone. The near equatorial updraft U zone is associated with large  $OLR_S''$ , 850 mb  $K_S''$ ,  $OLR_L''$ , and 850 mb  $K_L''$  in contrast with very small  $K_S''$  and  $K_L''$  at 200 mb. Conversely, subtropical downdraft D branches are characterized by small  $OLR_S''$  and  $OLR_L''$ , considerably small 850 mb  $K_S''$  and  $K_L''$ , and relatively large 200 mb  $K_S''$  and  $K_L''$ .

In JAN(-1), an anomalous indirect N-S overturning dominates the eastern Pacific ( $40^{\circ}$ N- $40^{\circ}$ S,  $180^{\circ}$ - $120^{\circ}$ W), where is the important area for ENSO. An inspection of Figs. 5.15, 5.16, and 5.17 indicates a close association of equatorial downdraft (D) with low-level easterlies and upper-level westerlies. As expected, these features are nearly identical to those shown in Fig. 5.14 for the RNS zone in JAN(0). The most interesting feature in Fig. 5.16b is the distinct northwest-southeast oriented zone of large

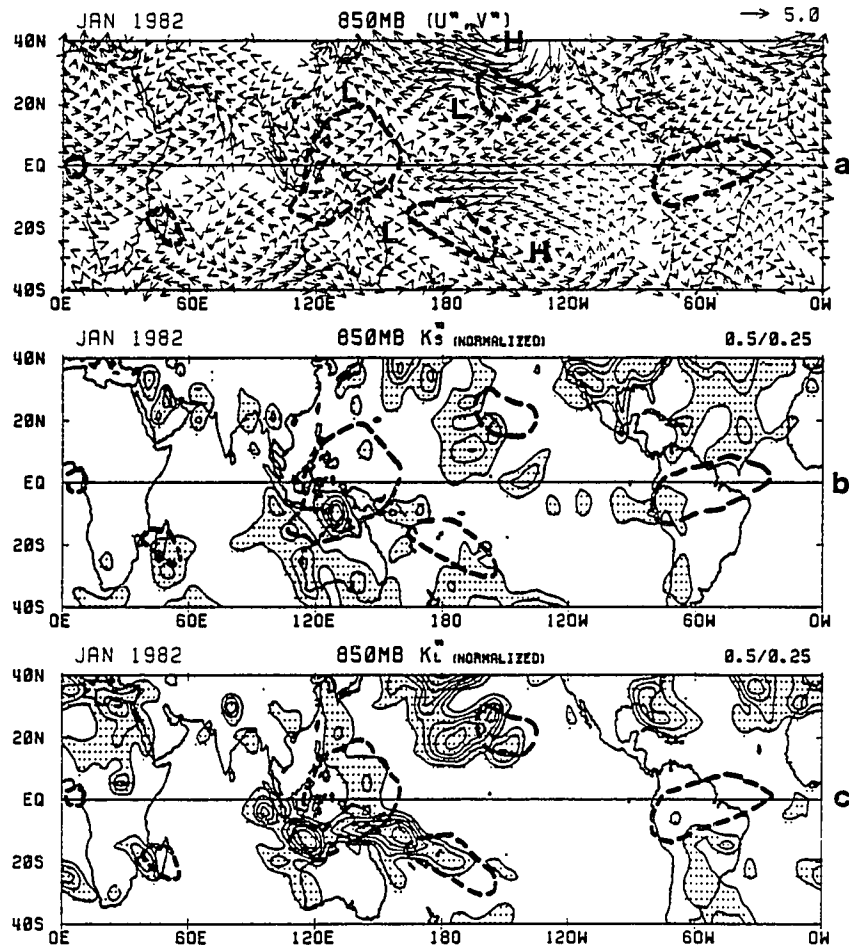


Fig. 5.17 As in Fig. 5.12, except for the pre-ENSO phase of January 1982.

$K_S''$  which approximately follows the 200 mb northwesterly flows over the equatorial eastern Pacific. This region of large  $K_S''$  is a direct consequence of anomalous transient eddy activity in and around the anomalously intensified upper-tropospheric oceanic troughs in JAN(-1). Thus, the equatorial eastern Pacific can be identified as a duct for wave energy fluxes between the two hemispheres during the normal winter. Refer also to Murakami and Unninayer (1977) for the presence of large transient eddy kinetic energy at 200 mb over the eastern North and South Pacific in the winter of 1970/71, a pre-ENSO phase with respect to the 1972/73 ENSO event.

Likewise, the striking feature in Fig. 5.16c is the very large 30-60 day transient energy  $K_L''$  over the central Pacific connecting the two hemispheres with the maximum center to northwest of the 2-15 day counterpart  $K_S''$ . However, the large  $K_L''$  region stretches upstream through the northwestern Pacific and southeastern Asia to the Tibetan Plateau. This is consistent with a series of the 30-60 day eastward propagating anticyclones (cyclones) found in this area by Murakami (1987) using a composite technique. Therefore, the central Pacific is fundamentally important for the hemispheric connection of 30-60 day activity  $K_L''$ , and for the interaction between  $K_L''$  and interannual modes.

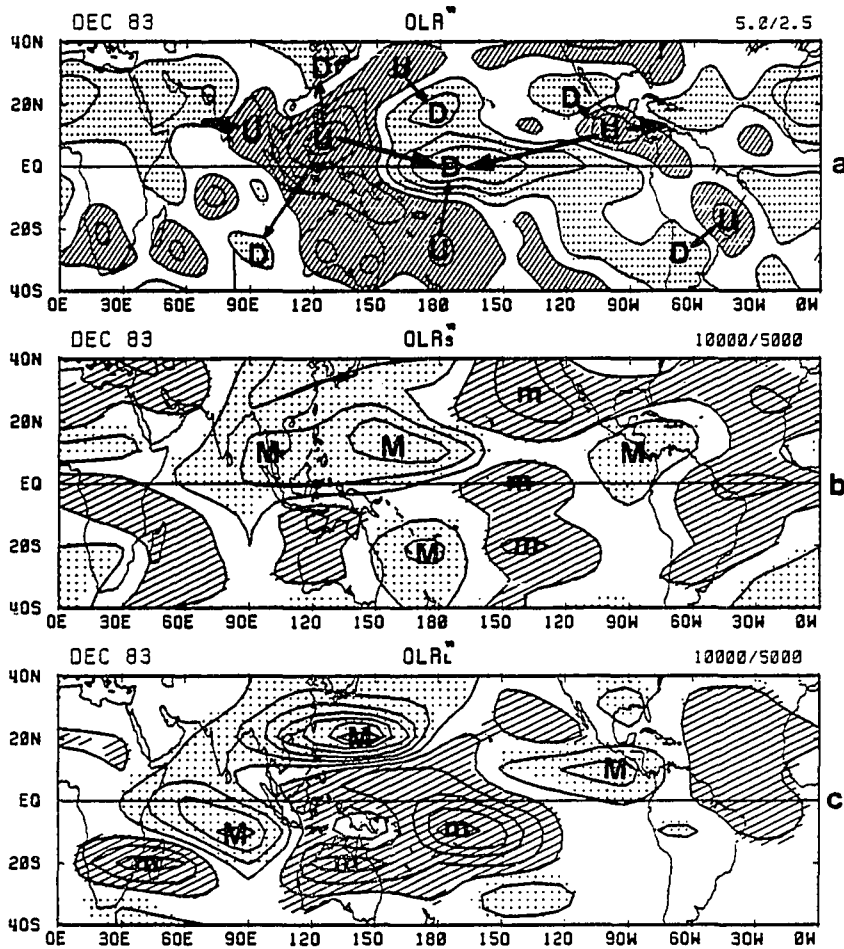


Fig. 5.18 As in Fig. 5.9, except for the post-ENSO phase of December 1983.

#### 5.4.3. DEC(0) Circulation Patterns

Judging from the time-longitude sections along the equator for  $OLR''$  (Fig. 4.7c) and 850 mb  $u''$  (Fig. 5.1d), January 1984 would probably be most representative of the post-ENSO phase, which would be another extreme of non-ENSO steady state, or anti-ENSO phase. However, due to the unavailability of the January 1984 data in the present study, The December 1983 was selected as the approximate post-ENSO phase. The DEC(0) patterns for all variables are shown in Figs. 5.18, 5.19, and 5.20. These patterns exhibit essentially the same characteristic features as in Figs. 5.15, 5.16, and 5.17, respectively for JAN(-1). The major discrepancies between DEC(0) patterns and JAN(-1) patterns occur in the  $OLR_L''$ , 850 mb  $K_L''$ , and 200  $K_L''$  fields (Figs. 5.15c and 5.18c, 5.16c and 5.19c, 5.17c and 5.20c), indicating that the 30-60 day activity has more degrees of freedom to affect on or interact with interannual modes.

Similar to the JAN(-1) phase, the upper oceanic troughs appear to be more pronounced than normal over the eastern North and South Pacific as shown in Fig. 5.19a. The equatorial  $u''$  easterlies between these twin cyclones are overlying the 850 mb  $u''$  westerlies (Fig. 5.20a). Associated with this is an equatorial downdraft ( $OLR'' > 0$ ; Fig. 5.18a). In conjunction, a marked zone of large  $K_S''$  at 200 mb (Fig. 5.19b) stretches all the way from  $40^\circ N$  to  $40^\circ S$  along about  $180^\circ$ - $140^\circ W$ . This reconfirms the occurrence of

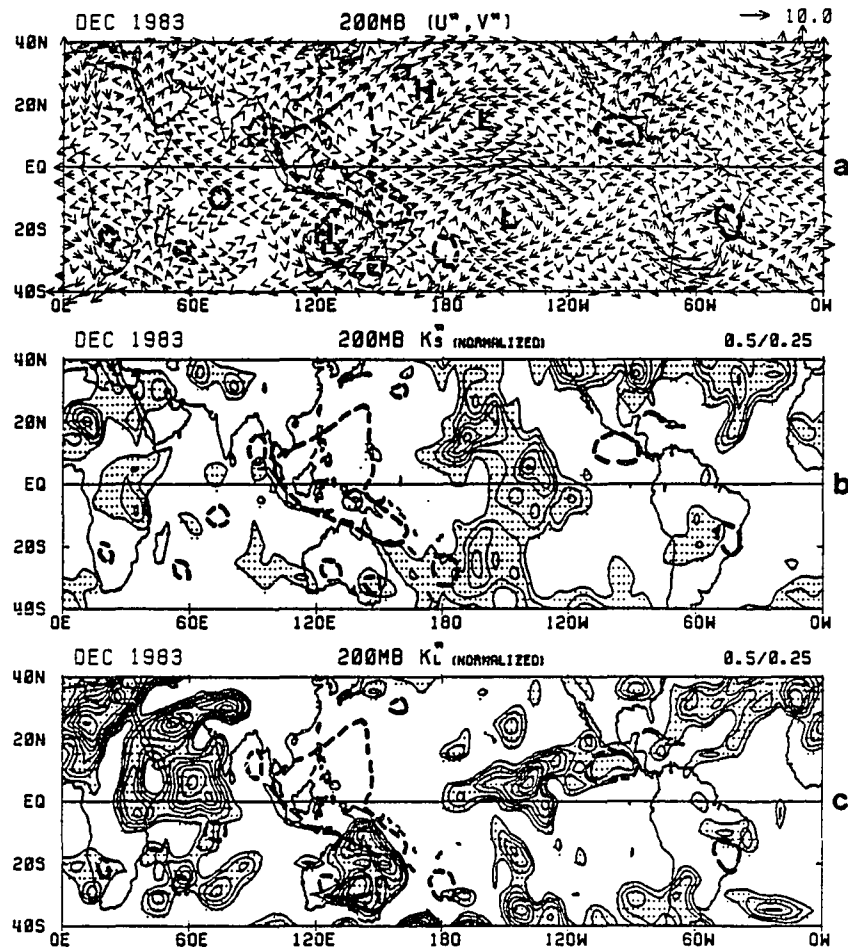


Fig. 5.19 As in Fig. 5.11, except for the post-ENSO phase of December 1983.

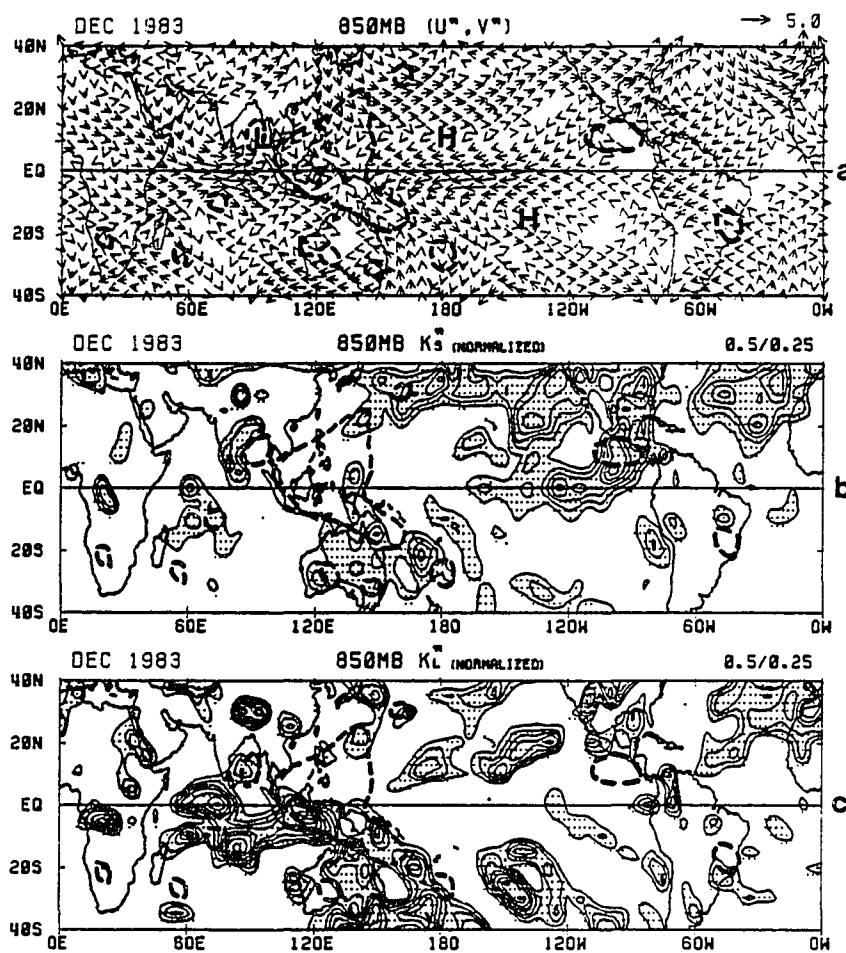


Fig. 5.20 As in Fig. 5.12, except for the post-ENSO phase of December 1983.

well above normal transient disturbance activity at 200 mb in and around the anomalous upper oceanic troughs over the eastern Pacific, where the dry weather ( $OLR'' > 0$ ) persists throughout the post-ENSO phase of DEC(0).

### 5.5. Momentum Budget for Low-Level $u''$ Westerlies

As mentioned in Section 5.2., the origin of low-level equatorial  $u''$  westerlies is a question of fundamental importance. With this in mind, an attempt is made to measure momentum transports due to intraseasonal disturbances and to identify their role in the initiation and/or maintenance of  $u''$  westerlies. Daily momentum transports due to short-period disturbances can be expressed as the products  $u_s u_s$  and  $u_s v_s$ , where the suffix  $s$  refers to the 2-15 day filtered wind data. The three-month running mean anomalies, i.e.,  $(u_s u_s)''$  and  $(u_s v_s)''$ , are then computed in the same manner as shown in the eq. 3. In Fig. 5.21, arrows indicate the line integrated values for  $(u_s u_s)''$  along the east and west boundaries and for  $(u_s v_s)''$  cross the north and south boundaries, whereas the number at the center of each box represents the net balance of momentum fluxes. Here, a positive (negative) balance indicates gain (loss) of westerly  $u''$  momentum due to short-period (2-15 day) perturbations. Also shown in Fig. 5.21 is an area averaged value for  $u''$  (signified as  $\bar{u}''$ ). The  $180^\circ$  longitudes x  $20^\circ$  latitudes. boxes were selected to follow the

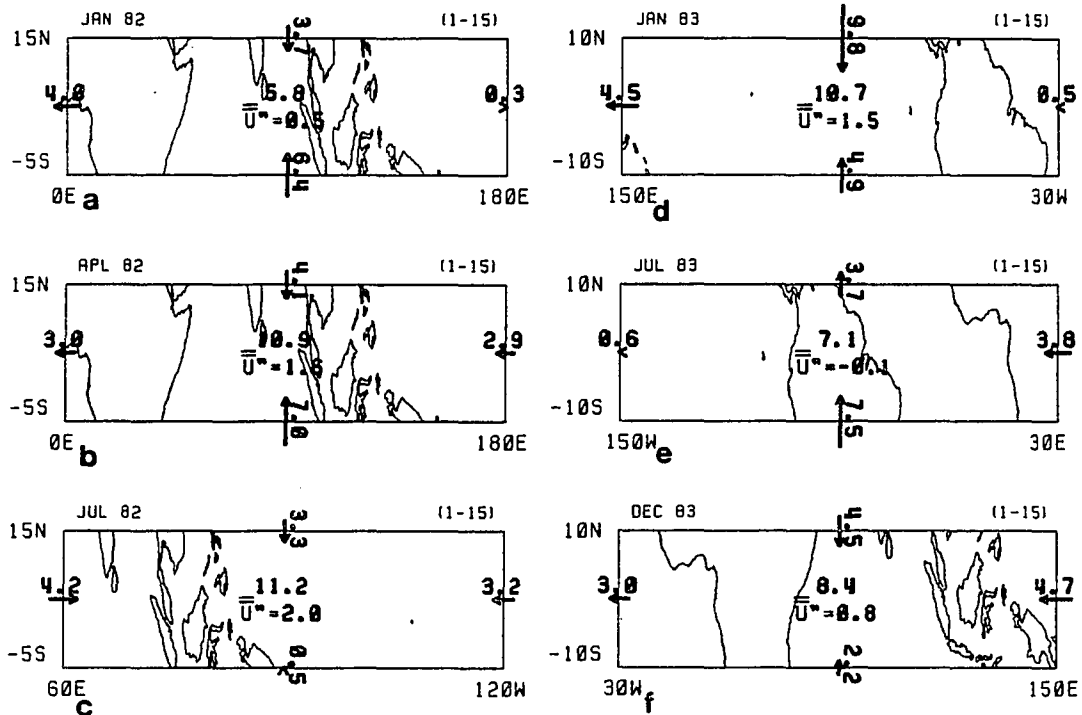


Fig. 5.21 Westerly momentum budget due to short-period (2-15 day) disturbances at 850 mb. Arrows are proportional to the direction and magnitude of the momentum fluxes integrated along the boundaries (unit:  $10^6 \text{ m}^3 \text{ s}^{-2}$ ), while the number at the center of the represents the net westerly momentum balance. The areal averaged zonal wind  $\bar{u}$  is also shown at the center of diagram.

trajectory of the eastward propagating 850 mb  $u''$  westerlies during one cycle of the 1982/83 ENSO.

Except for July 1983,  $\bar{u}''$  is positive (westerly), reaching a maximum of  $2.0 \text{ ms}^{-1}$  during the onset phase of July 1982. The net momentum balance becomes substantially large (+10.9 units) in April 1982 (Fig. 5.21b), a pre-onset phase. This value corresponds to an approximate westerly acceleration of  $1 \text{ ms}^{-1}$  per month. Considering the large space and time scale, this value reflects a significant contribution of short-period (2-15 day) perturbations toward the westerly acceleration of  $\bar{u}''$  over the Africa-Indian Ocean-western Pacific region. The net westerly momentum gain also has the maximum of 11.2 units in the onset phase of January 1982 (Fig. 5.21c), during which the zonal convergence of westerly momentum is significant. During the mid-ENSO of January 1983 (Fig. 5.21d), momentum influxes across the northern ( $10^{\circ}\text{N}$ ) boundary appear to be the major contributor to the net momentum balance for  $\bar{u}''$  over the Pacific-South America region. This is coincident with the results in Fig. 5.19a, that is, short-period (2-15 day) activity over the North Pacific exerts some influence on interannual modes in the equatorial central-eastern Pacific. Here, it is worth looking again at Fig. 5.12a to note the large longitudinal as well as latitudinal extent of low-level westerly  $u''$  perturbations in JAN(0).

In Fig. 5.21, the most important indication is that the net momentum balance is positive (gain) throughout one cycle of ENSO from January 1982 to December 1983. The short-period (2-15 day) transient eddies constantly furnish westerly momentum to interannual  $u''$  perturbations. Thus, the importance of barotropic nonlinear interactions between these two components is established. Interestingly, the net momentum gain as well as the areal averaged  $\bar{u}''$  both have a maximum in the onset phase of July 1982 instead of the mature phase of Jan. 1983. The established  $u''$  westerlies would then contribute to an fully ocean-atmosphere coupling on interannual time scale.

Likewise, shown in Fig. 5.22 are the westerly momentum budget due to the 30-60 day filtered 850 mb wind perturbations. Prior to the ENSO onset, low-frequency (30-60 day) oscillations appear to be equally important for the momentum balance of low-level  $u''$  westerlies, as compared with the 2-15 day counterpart. This can be confirmed in Fig. 5.22b for April 1982 which presents the net momentum flux convergence (gain) due to  $(u_L u_L)''$  and  $(u_L v_L)''$ , i.e., zonal and meridional momentum transports by low-frequency oscillations. At this time, a large influx (11.6 units) across the southern boundary is nearly compensated for by a large export (12.8 units) at the northern boundary. This is probably due to the planetary-scale of 30-60 day oscillation and relatively short distance in meridional

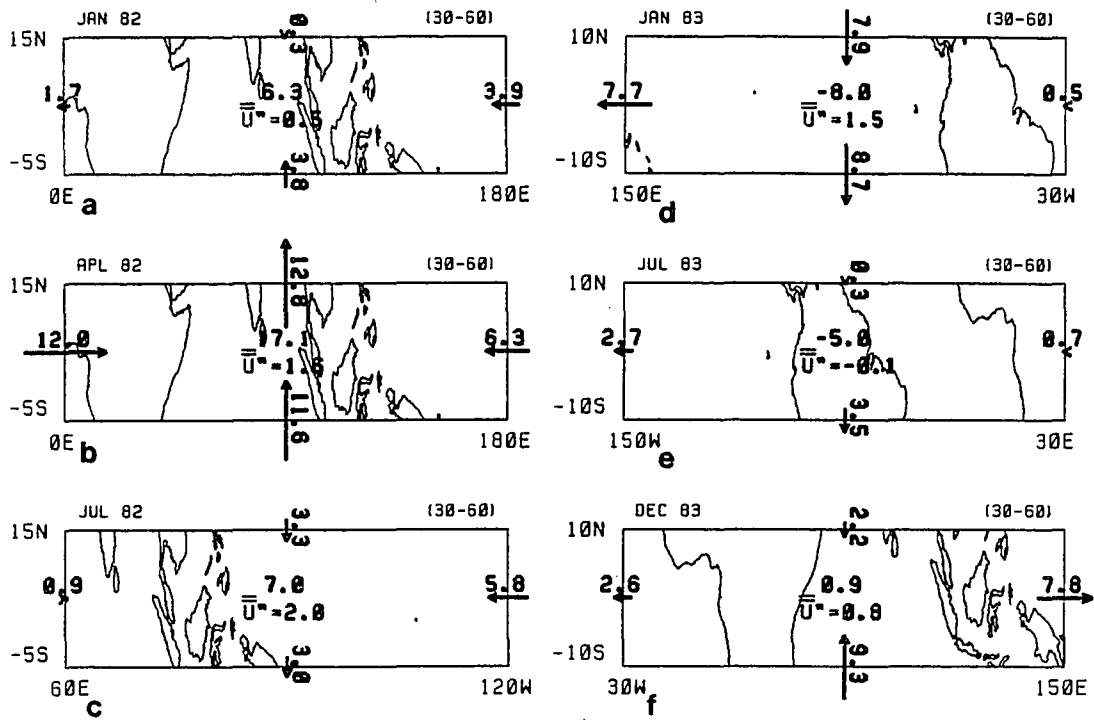


Fig. 5.22 As in Fig. 5.21, except for low-frequency (30-60 day) perturbations.

direction for the selected reference box. However, there exists substantial zonal flux convergence across the eastern and western boundaries at this pre-onset stage. The net balance amounts to as much as 17.1 units in April 1982. This is consistent with the previous observation in Figs. 5.2, 5.3b, and 5.5 that the activity of 30-60 day oscillations becomes exceptionally strong over the Indian Ocean, in terms of an amplitude modulation process affecting the western Pacific, prior to the ENSO onset. Therefore, low-frequency (30-60 day) oscillations are vital for the enhancement of interannual zonal wind perturbations prior to and at the ENSO onset. The contribution due to low-frequency disturbances appears to become less important after the mid-ENSO phase of January 1983.

## 6. Discussion and Conclusion

### 6.1 Discussion

Based on OLR and wind data over the global tropics, the relationship between intraseasonal disturbance activity and interannual variation has been studied. The intraseasonal activity represented by spectra amplitude shows evidence of frequency modulation in different time scales. Especially, the 30-60 day oscillation exhibits considerable interannual frequency modulation with a period of 2-5 years over the equatorial Indian Ocean-maritime continent-western Pacific during the non-ENSO period, indicating an enhanced nonlinear energy exchange between intraseasonal disturbances and interannual modes. This phenomenon is not important over the central-eastern Pacific during the 1982/83 ENSO episode (Figs. 3.2 and 3.3). Further investigation on this aspect with more refined approach<sup>7</sup> is certainly necessary for a full understanding of the ENSO phenomenon.

The two constructed components of intraseasonal activity, i.e., 2-15 day and 30-60 day, show very different natures in conjunction with seasonality and interannual

---

<sup>7</sup>Diagnostic results from frequency domain may be biased due to high nonlinearity in data set. Thus, the conclusion from spectral analysis should be considered as preliminary until tested by different approaches.

modes. Namely, the seasonal and interannual amplitude modulation of 30-60 day oscillation is mainly confined to the Eastern Hemisphere tropics, and that of 2-15 day perturbations accompanies the major signal of short-term climate variations, e.g., ENSO events. The variability of both components exhibits evidence that the ENSO signal over the central-eastern Pacific is traceable to the Indian Ocean and western Pacific, where the 30-60 day oscillation undergoes large amplification. Thus it is reasonable to infer that this is a region for potential interaction between intraseasonal and interannual time scales, which correspond to a relatively low value for the climate signal-to-noise ratio, to occur. The recent studies (e.g., Graham and Barnett, 1987) have shown that over broad regions of the Indian Ocean and western Pacific SST in excess of  $27.5^{\circ}\text{C}$  is required for large-scale deep convection to occur. However, SST above that temperature is not a sufficient condition for convection, and further increases in SST appear to have little effect on the intensity of convection. Therefore, the intensive intraseasonal convective activity, particularly for 2-15 day OLRs<sup>''</sup>, over the Indian Ocean-western Pacific warm pool region is unlikely to couple with the ocean. In other words, this convection between intraseasonal disturbance assembly and interannual variation can only be associated with the atmospheric intrinsic vacillation, for example, westerly

bursts. This is consistent with the GCM experimental results that the 30-60 day mode is fundamentally an atmospheric phenomenon whose origin does not require a fully coupled ocean-atmosphere system (Hayashi and Sumi, 1986; Lau and Lau, 1986).

Synthesizing the above information, a possible dynamical link between intraseasonal activity and ENSO can be proposed as follows: The family of atmospheric waves associated with enhanced interannual variation can have a slow dynamic time scale much closer to that of the tropical ocean, which is about  $2 \text{ ms}^{-1}$  for equatorial oceanic Kelvin wave phase speed. When this occurs, a linear coupling between the ocean and atmosphere can become more effective, and unstable coupled linear modes may result (Lau, 1981; Philander *et al.*, 1984; Yamagata, 1985; Hirst, 1986; and Zebiak and Cane, 1987). However, the enhancement of the atmospheric interannual mode results from a series of energy support by intraseasonal activity cascading from high frequency to low frequency through a nonlinear interaction process. This certainly emphasizes the importance of transient disturbances to the ENSO phenomenon. It appears that an understanding of the dynamics of such an effect may shed new light on the mechanism of the onset and evolution of ENSO.

The results of the EOF analyses also support the above argument. The ENSO in interannual OLR variations can be

regarded as an intrinsic mode of a bimodal climate system in the tropical region, since the 1982/83 ENSO pattern is also obtained from the data excluding the ENSO period. On the other hand, the 30-60 day mode is spatially similar to the ENSO mode (Lau and Chan, 1987). Thus, the amplification of this intrinsic climate mode (ENSO), which is present in the tropical atmosphere all the time, can be triggered and/or terminated by the 30-60 day oscillation through seasonality. Namely, the 30-60 day mode is one of catalytic agents for ENSO onset (probable withdraw) which is likely phase locked with the annual cycle. This can be clearly seen in Fig. 5.5 for the 1982/83 ENSO. A similar phenomenon is also apparent in the most recent 1986/87 ENSO event (Nitta and Motoki, 1987).

Also presented (Figs. 3.4, 5.21, and 5.22) are some evidence of that 30-60 day mode as an ENSO trigger plays different role over the Indian Ocean and western Pacific. When the slow eastward propagating interannual modes (Fig. 5.1) are over the Indian Ocean before ENSO onset, 30-60 day oscillation is the dominant factor for its maintenance and enhancement or even generation. When interannual modes reach the western Pacific after crossing the Indian Ocean, all type of intraseasonal disturbances are responsible for its rapid intensification. This corresponds to the ENSO onset period when 30-60 day oscillation not only itself enhances interannual mode but also plays a role of bridge

between transient disturbances (period < 30 days) and interannual variation. A detailed analysis of Murakami and Sumathipala (1988) supports above suggestion.

## 6.2 Conclusion

The present study have shown the existence of frequency and amplitude modulation phenomena in the atmosphere. However during the course of the 1982/83 ENSO, all intraseasonal components of atmospheric convective activity are significantly intensified over the central-eastern Pacific ocean, reflecting the depressed frequency modulation and enhanced amplitude modulation.

The EOF results have illustrated the existence of bimodal steady states on the time scale of the recurrence of ENSO, i.e., non-ENSO and ENSO. ENSO onset corresponds to transition from non-ENSO to ENSO, and ENSO withdraw corresponds to transition from ENSO to non-ENSO (Fig. 4.7). These transitions are phase locked with seasonality, and are likely actuated by 30-60 day oscillation (Fig. 5.5).

Within the data period of this study, the highlight is the 1982/83 ENSO with its peak phase (mid-ENSO) in January 1983; and with the pre-ENSO phase of January 1982 and the post-ENSO of December 1983. Thus, one cycle of the 1982/83 ENSO covers a two-year period from January 1982 to December 1983. The phase changes during one cycle, i.e., transition from non-ENSO to (mid-) ENSO or vice versa, occur in

association with the slow eastward propagation of inter-annual time-scale perturbations. The above statements are confirmed in the time-longitude sections of the three-month running mean anomalies, such as,  $OLR''$  in Fig. 4.7 and  $u''$  in Fig. 5.1.

The synoptic features characteristic of the mid-ENSO (mature ENSO) at any location are a complete reversal to those of pre-ENSO (or post-ENSO) which is an extreme of non-ENSO state, i.e., anti-ENSO. The pre-ENSO (or post-ENSO) synoptics are a manifestation of an anomalous enhancement of the characteristic features of the normal winter circulation, i.e., a steady state on the seasonal time scale which is superimposed on the non-ENSO state. For example, over the eastern North and South Pacific between about the date line and  $120^{\circ}W$ , the main characteristic of the pre-ENSO (or post-ENSO) and mid-ENSO phases are summarized as follows:

(a.) Pre-ENSO (or post-ENSO) exhibits an unusual intensification of upper oceanic troughs over the extra-tropical North and South Pacific with exceptionally intense equatorial westerlies ( $u'' > 0$ ). Substantial intraseasonal disturbance activity ( $K_S'' > 0$ ,  $K_L'' > 0$ ) at 200 mb, indicates a strong hemispheric interaction of the intraseasonal time scale. These features are a result of an anomalously intensified indirect N-S vertical overturning with below

normal equatorial convective activity ( $OLR'' < 0$ ) in contrast to above normal rainfall ( $OLR'' > 0$ ) over the extratropics.

(b.) Mid-ENSO experiences the development of a direct N-S vertical overturning (anomaly) with equatorial convection ( $OLR'' < 0$ ) and extratropical dry weather ( $OLR'' > 0$ ). An unusual weakening of upper oceanic troughs or anticyclones takes place in conjunction with substantial equatorial upper easterlies (anomaly). Thus, the intraseasonal  $K_S''$  and  $K_L''$  disturbance activity is inhibited. Poleward of the twin anomalous anticyclones are stronger than usual midlatitude westerlies and associated above normal baroclinic disturbance activity ( $K_S'' > 0$ ,  $K_L'' > 0$ ) at 200 mb.

In short, the eastern North and South Pacific bear a complete reversal of circulation features from those depicted in Fig. 5.14 for a RNS zone during the pre-ENSO (a possible anti-ENSO) phase to those exhibited in Fig. 5.13 for the DNS zone during the mid-ENSO phase. In other words, the circulation features over this area change from the RNS-type (pre-ENSO), via DNS-type (mid-ENSO), and back to RNS-type (post-ENSO) during a complete 1982/83 ENSO cycle.

The Japan-maritime continent-Australia region between about  $100^\circ$  and  $160^\circ$ E is another key area. Here, a well-defined reversal of circulation characteristics also occurs with DNS-type circulation during the pre-ENSO (post-ENSO) phase and RNS-type during the mid-ENSO phase. Thus,

circulation changes over this key area are out of phase with those over the eastern North and South Pacific region.

In addition, less organized circulation reversals also take place over the following two regions: (1) Afghanistan-Indian Ocean region between  $40^{\circ}$  and  $80^{\circ}$ E where anomalous circulation features are approximately in phase (out of phase) with the eastern North and South Pacific (Japan-maritime continent-Australia) region. Hence, one notes a RNS-type circulation in pre-ENSO (or post-ENSO), and DNS-type in mid-ENSO. (2) Central America-South American region between about  $80^{\circ}$ W and  $40^{\circ}$ W has an approximately out of phase (in phase) relationship with the eastern Pacific (Japan-maritime continent-Australia) region. A DNS-type circulation appears in pre-ENSO (or post-ENSO) and a RNS-type in mid-ENSO.

Combining all circulation characteristics along the equator which have been described so far, the phase shift of the Walker circulation is clearly defined during the ENSO episode (Wyrtki, 1980). However, this zonal-type planetary circulation changes its phase not only along the equator, but also over the midlatitudes.

In conclusion, interannual modes are planetary in scope, and exhibit coherent features over the tropics and extratropics. They encircle the globe from Africa and the Indian Ocean in the west to the eastern Pacific and North and South America in the east, and extend from the Northern

Hemisphere extratropics ( $40^{\circ}\text{N}$ ) to the Southern Hemisphere extratropics ( $40^{\circ}\text{S}$ ). These interannual modes undergo a long life cycle, through which short period (2-15 day) as well as low-frequency (30-60 day) perturbations furnish energy to interannual modes, such as, 850 mb  $u''$ . This phenomenon necessitates the monitoring of intraseasonal disturbance activity as an important parameter for describing the climate regime.

This study presented a single ENSO event, i.e., the 1982/83 ENSO, and thus, the conclusion should be regarded as preliminary until further tested with many other ENSO events including the recent 1986/87 event.

On the whole this study has raised many more questions than it has answered. Hopefully many of these will be resolved with more studies. Knowledge of nonlinear interaction between interannual variation and intraseasonal disturbance are necessary for complete understanding of ENSO, and to climate forecasting. The results presented here may help to direct future work on these important problems.

## Appendix

### A. Significance Test for EOF Eigenmodes

A Monte Carlo simulation is a more accurate approach for selecting eigenvalues in an EOF analysis for which the meteorological signal is above the level of noise (Preisendorfer and Barnett, 1977; Overland and Preisendorfer, 1982). The method is outlined as following. Let  $e_m$ ,  $m=1, \dots, M$ , be the eigenvalues of the spatial correlation matrix  $R(x, x')$  computed from  $N$  observations, such that  $e_1 > e_2 \dots > e_M$ .  $M$  is total number of grid points, and  $N$  is total number of days or months for the data set used. The normalized eigenvalue statistic can be formed as:

$$X_m = e_m \left( \sum_{m=1}^M e_m \right)^{-1}, \quad m=1, \dots, M. \quad (A1)$$

In order to determine the significance of each eigenvalue, the null hypothesis is that the meteorological data is randomly drawn from a population of uncorrelated gaussian variables. Use a random number generator to generate  $N$ -length gaussian time series of zero mean and unit variance at each grid point, and compute the correlation matrix. Compute the eigenvalues of the correlation matrix and repeat this experiment  $I$  ( $I$  should be larger than 100 in general) times. If  $d_m^i$ ,  $m=1, \dots, M$ , is the set of eigen-

values produced by the  $i$ -th Monte Carlo simulation, the statistic analogous to (A1) is

$$Y_m^i = d_m^i \left( \sum_{m=1}^M d_m^i \right)^{-1}, \quad m=1, \dots, M, \text{ and } i=1, \dots, I. \quad (\text{A2})$$

For fixed  $m$ , order the  $Y_m^i$  so that

$$Y_m^1 \leq Y_m^2 \leq \dots \leq Y_m^I. \quad (\text{A3})$$

Let  $s$  is a significance level, for example  $s=95\%$ . For each experimental EOF modes  $m=1, \dots, M$ , select  $X_m^C = Y_m^{i_C}$  where  $i_C = s R$  as a criterion at confidence level  $s$ . Compare  $X_m$  with  $X_m^C$ . If  $X_m$  is larger than  $X_m^C$ , the  $m$ -th eigenmode is significant at level  $s$ , otherwise, the eigenmode is in noise level.

#### B. Measurement of Climate Predictability

The basic assumption of this method is that meteorological data can be treated as stationary stochastic variable. Following Chu and Katz (1987), only a particular class of stationary models known as autoregressive-moving average process (ARMA) is considered. An ARMA( $p, q$ ) process  $X_t$  with mean zero and variance  $\sigma^2$  can be expressed as

$$X_t = \sum_{i=1}^p \phi_i X_{t-i} + a_t - \sum_{j=1}^q \theta_j a_{t-j} \quad (\text{B1})$$

Here the  $\phi$  and  $\theta$  are called autoregressive (AR) and moving average (MA) parameters, respectively. In (B1), it is assumed that the  $a_t$  are uncorrelated random variables with mean zero and variance  $\sigma_a^2$  from a Gaussian distribution.

If the model (B1) best fits meteorological data, a forecast from time origin  $t$  to  $m$  time steps ahead can be written as

$$\hat{X}_t(m) = \sum_{i=1}^p \phi_i X_{t+m-i} + a_{t+m} - \sum_{j=1}^q \theta_j a_{t+m-j} \quad (\text{B2})$$

In (B2), forecasted values (zeroes) are substituted for  $X$ 's ( $a$ 's) that have not yet been observed.

Assume that the parameters of the ARMA process ( $\phi$ ,  $\theta$ ,  $\sigma^2$ , and  $\sigma_a^2$ ) are known. This means that the present and past error terms ( $a_t$ ,  $a_{t-1}$ ,  $a_{t-2}$ , ...) are known. Let

$$e_t(m) = X_{t+m} - \hat{X}_t(m) \quad (\text{B3})$$

be the  $m$ -step ahead forecast error and  $V(m) = \text{var}[e_t(m)]$  be its variance.

According to Box and Jenkins (1976, p.47), an ARMA( $p, q$ ) process in (B1) is equivalent to an infinite order MA process as follows

$$X_t = \sum_{j=0}^{\infty} \psi_j a_{t-j} \quad (\text{B4})$$

with  $\psi_0 \equiv 1$ . Now by using (B4), the forecast error variance  $V(m)$  can be expressed as

$$\begin{aligned} V(1) &= \sigma_a^2, \\ V(m) &= (1 + \sum_{j=1}^{m-1} \psi_j^2) \sigma_a^2, \quad m=2,3,\dots \end{aligned} \quad (\text{B5})$$

By comparing the variance of the  $m$ -step ahead forecast errors to the variance of the  $X_t$ -process (  $^2$  ), the fractional variance "explained" by the  $m$ -step ahead forecast can be defined as

$$\begin{aligned} \lambda_0 &\equiv 1, \\ \lambda_m &= 1 - \frac{V(m)}{\sigma^2}, \quad m=1,2,\dots \end{aligned} \quad (\text{B6})$$

in other words, the  $m$ -step ahead predictability for any ARMA process can be expressed as solely a function of the  $\psi$ -weights defined by

$$\Lambda(m) = \sum_{j=1}^{\infty} \psi_j^2, \quad m=0,1,2,\dots \quad (\text{B7})$$

Now, (B6) becomes

$$\lambda_m = \Lambda(m)/\Lambda(0) \quad (\text{B8})$$

The stationarity constraint on the ARMA parameters requires

(B7) being a finite sum. It is clear that  $0 \leq \lambda_m \leq 1$ , with  $\lambda_m = 0$  for the case of no predictability and  $\lambda_m = 1$  for the case of perfect predictability  $m$ -steps ahead. Moreover,  $\lambda_m$  necessarily tends to zero as  $m$  tends to infinity.

## Reference

- Ardanny, P.E., and T.N. Krishnamurti, 1987: Divergent circulation inferred from Nimbus-7 ERB: Application to the 1982-83 ENSO event. J. Meteor. Soc. Japan, 65, 353-370.
- Arkin, P.A., J.D. Kopman, and R.W. Reynolds, 1983: 1982-83 El Nino/Southern Oscillation Event Quick Look Atlas. Climate Analysis Center, NOAA/NMC, Washington.
- Barnett, T.P., 1983: Interaction of the monsoon and the Pacific trade wind system in interannual time scale. Part I: The equatorial zone. Mon. Wea. Rev., 111, 756-773.
- Bjerknes, J., 1966: A possible response of the atmospheric Hadley circulation to equatorial anomalies of ocean temperature. Tellus, 18, 820-829.
- \_\_\_\_\_, 1969: Atmospheric teleconnections from the equatorial Pacific. Mon. Wea. Rev., 97, 163-172.
- \_\_\_\_\_, 1972: Large-scale atmospheric response to the 1964-65 Pacific equatorial warming. J. Phys. Oceanogr., 2, 212-217.
- Chu, P.-S., and R.W. Katz, 1987: Measures of predictability with applications to the Southern Oscillation. Mon. Wea. Rev., 115, 1542-1549.
- Gill, A.E., and E.M. Rasmusson, 1983: The 1982-83 climate anomaly in the equatorial Pacific. Nature, 306, 229-234.

- Graham, N.E., and T.P. Barnett, 1987: Sea surface temperature, surface wind divergence, and convection over tropical oceans. Science, 238, 657-659.
- Grimmer, M., 1963: The space-filtering of monthly surface temperature anomaly data in terms of pattern, using empirical orthogonal functions. Quart. J. Roy. Soc., 89, 395-408.
- Gruber, A., and J.S. Winston, 1978: Earth-atmosphere radiative heating based on NOAA scanning radiometer measurements. Bull. Amer. Meteor. Soc., 59, 1570-1573.
- Harrison, D.E., and P.S. Schopf, 1984: Kelvin wave-induced anomalous advection and the onset of surface warming in El Nino events. Mon. Wea. Rev., 112, 923-933.
- Hirst, A.C., 1986: Unstable and damped equatorial modes in simple coupled ocean-atmosphere models. J. Atmos. Sci., 43, 606-630.
- Hoskins, N.J., and D.J. Karoly, 1981: The steady linear response of a spherical atmosphere in thermal and orographic forcing. J. Atmos. Sci., 38, 1174-1196.
- Keen, R., 1987: Equatorial westerlies and the Southern Oscillation. Mon. Wea. Rev., in press.
- Kutzbach, J.E., 1967: Empirical eigenvectors of sea-level pressure, surface temperature and precipitation complexes over North America. J. Appl. Meteor., 6, 791-802.

- Lau, K.M., 1981: Oscillation in a single equatorial climate system. J. Atmos. Sci., 38, 248-261.
- Lau, K.M., 1985a: Bimodal climate state, subseasonal scale oscillation and the El Nino/Southern Oscillation. Coupled Ocean-Atmosphere Models, J. Nihoul, Ed., Elsevier, Amsterdam, 766pp.
- \_\_\_\_\_, 1985b: Elements of a stochastic dynamical theory of the long-term variability of the El Nino/Southern Oscillation. J. Atmos. Sci., 112, 1552-1558.
- \_\_\_\_\_, and H. Lim, 1984: On the dynamics of equatorial forcing of climate teleconnections. J. Atmos. Sci., 41, 167-171.
- \_\_\_\_\_, and P.H. Chan, 1985: Aspects of the 40-50 day oscillation during the northern winter as inferred from outgoing longwave radiation. Mon. Wea. Rev., 114, 1354-1367.
- \_\_\_\_\_, 1986: The 40-50 day oscillation and El Nino/Southern Oscillation: A new perspective. Bull. Amer. Meteor. Soc., 67, 533-534.
- \_\_\_\_\_, 1987: Interannual and intra-seasonal variations of tropical convection: A possible link between the 40-50 day oscillation and ENSO. J. Atmos. Sci., 44, in press.
- \_\_\_\_\_, and S. Shen, 1987: On the dynamics of intra-seasonal oscillation and ENSO. J. Atmos. Sci., in press.

- Lukas, R., S.P. Hayes, and K. Wyrтки, 1984: Equatorial sea level response during the 1982-83 El Niño. J. Geophys. Res., 89, 10425-10430.
- \_\_\_\_\_, 1987: On the role of western Pacific air-sea interaction in the El Niño/Southern Oscillation phenomenon. In Proceedings of the U.S. TOGA western Pacific air-sea interaction workshop, Honolulu, 16-18 Sep. 1987, R. Lukas and P. Webster, eds., 1988, p1-27.
- Luther, P.S., D.E. Harrison, and R.A. Knox, 1983: Zonal winds in the central equatorial Pacific and El Niño. Science, 222, 327-330.
- McCreary, J.P., 1976: Eastern tropical ocean response to changing wind systems: With application to El Niño. J. Phys. Oceanogr., 6, 29-35.
- Meehl, G.A., 1987: The annual cycle and interannual variability in the tropical Pacific and Indian Ocean regions. Mon. Wea. Rev., 115, 27-50.
- Madden, R.A., and D.J. Shea, 1972: Estimates of the natural variability of time-averaged temperature over the United States. Mon. Wea. Rev., 106, 942-952.
- Murakami, M., 1979: Large-scale aspects of deep convective activity over the GATE area. Mon. Wea. Rev., 107, 994-1013.
- Murakami, T., 1987: Intraseasonal atmospheric teleconnection patterns during the Northern Hemisphere summer. Mon. Wea. Rev., 115, 2133-2154.

- \_\_\_\_\_, 1988: Intraseasonal atmospheric teleconnection patterns during the Northern Hemisphere winter. J. of Climate, 1, No. 2, 117-131.
- \_\_\_\_\_, and M.S. Unninayar, 1977: Atmospheric circulation during December 1970 through February 1971. Mon. Wea. Rev., 105, 1024-1035.
- \_\_\_\_\_, T. Nakazawa, and J. He, 1984: On the 40-50 day oscillations during the 1979 Northern Hemisphere summer. Part I: Phase propagation. J. Meteor. Soc. Japan, 62, 440-468.
- \_\_\_\_\_, L.-X. Chan, and A. Xie, 1986a: Relationship among seasonal cycles, low-frequency oscillations, and transient disturbances as revealed from outgoing longwave radiation data. Mon. Wea. Rev., 114, 1456-1465.
- \_\_\_\_\_, L.X. Chan, A. Xie, and M.L. Shrestha, 1986b: Eastward propagation of 30-60 day perturbations as revealed from outgoing longwave radiation data. J. Atmos. Sci., 43, 961-971.
- \_\_\_\_\_, and W.L. Sumathipala, 1988: Relationship between outgoing longwave radiation and sea surface temperature on interannual time scale. To be submitted to J. of Climate.
- Nakazawa, T., 1986: Intraseasonal variations of OLR in the tropics during the FGGE year. J. Meteor. Soc. Japan, 64, 17-34.

- Nitta, T., and T. Motoki, 1987: Abrupt enhancement of convective activity and low-level westerly burst during the onset phase of the 1986-87 El Niño. J. Meteor. Soc. Japan, 65, 497-506.
- North, G.R., T.C. Bell, R.F. Cahalan, and F.J. Moeng, 1982: Sampling errors in the estimation of empirical orthogonal functions. Mon. Wea. Rev., 110, 699-706.
- Overland, J.E., and R.W. Preisendorfer, 1982: A significance test for principal components applied to a cyclone climatology. Mon. Wea. Rev., 110, 1-4.
- Philander, S.G.H., 1983: El Niño Southern Oscillation phenomena. Nature, 302, 295-301.
- \_\_\_\_\_, T. Yamagata, and R.C. Pacanowski, 1984: Unstable air-sea interactions in the tropics. J. Atmos. Sci., 41, 604-613.
- Preisendorfer, R.W., and T.P. Barnett, 1977: Significance test for empirical orthogonal functions. Reprints Fifth Conf. Probability and Statistic in Atmospheric Sciences, Las Vegas, Amer. Meteor. Soc., 169-172.
- Rasmusson, E.M., and T.H. Carpenter, 1982: Variations in tropical sea surface temperature and surface wind fields associated with the Southern Oscillation/El Niño. Mon. Wea. Rev., 110, 354-384.
- \_\_\_\_\_, and J.M. Wallace, 1983: Meteorological aspects of the El Niño/Southern Oscillation. Science, 222, 1195-2222.

- Sardeshmukh, P.D., and B.J. Hoskins, 1987: On the generation of global rotational flow by steady idealized tropical divergence. J. Atmos. Sci., in press.
- Shrestha, M.L., 1986: Interannual variation of 30-60 day oscillations and their structure during summer and winter. Ph.D. dissertation, University of Hawaii, Dept. of Meteorology, 198pp.
- Shukla, J., and D. Gutzler, 1983: Interannual variability and predictability of 500 mb geopotential heights over the Northern Hemisphere. Mon. Wea. Rev., 111, 1273-1279.
- Trenberth, K.E., 1985: Potential predictability of geopotential heights over the Southern Hemisphere. Mon. Wea. Rev., 113, 54-64.
- Walker, G.T., 1923: Correlation in seasonal variations of weather, VIII: A preliminary study of world weather. Memoirs of the India Meteorological Department, 24, Part 4, Calcutta, 75-131
- \_\_\_\_\_, 1924: Correlation in seasonal variations of weather, IX: A further study of world weather. Memoirs of the India Meteorological Department, 24, Part 9, Calcutta, 275-332.
- Wang, X.-L., 1986: Relationship between intraseasonal low-level meridional winds and monsoonal convection during the southern hemisphere summer. M.S. Thesis, Dept. of Meteorology, University of Hawaii, pp135.

- Webster, P.J., and J.R. Holton, 1982: Cross-equatorial response to middle-latitude forcing in a zonally varying basic state. J. Atmos. Sci., 39, 722-733.
- \_\_\_\_\_, H.R. Chang, and D. Min, 1987: Equatorial wave energy accumulation and emanation zones: Implications for climate regime transient. Presented at the IUGG XIX General Assembly. Vancouver, Canada, August 9-22, 1987.
- Weickmann, K.M., G.R. Lussky, and J.E. Kutzbach, 1985: Intraseasonal (30-60 day) fluctuations of outgoing longwave radiation and 250 mb streamfunction during Northern summer. Mon. Wea. Rev., 113, 941-961.
- Wyrtki, K., 1975: El Nino-the dynamic response of the equatorial Pacific Ocean to atmosphere forcing. J. Phys. Oceanogr., 5, 572-584.
- Yamagata, T., 1985: Stability of a simple air-sea coupled model in the tropics. Coupled Ocean-Atmosphere Models, J. Nihoul, Ed., Elsevier, Amsterdam, 766pp.
- Yamazaki, N., and M. Murakami, 1987: An intraseasonal amplitude modulation of the short-term tropical disturbances over the western Pacific. J. Meteor. Soc. Japan, in press.
- Zebiak, S.E., and M. Cane, 1987: A model ENSO. J. Atmos. Sci., 44, 2334-2356.